CHALMERS
UNIVERSITY OF TECHNOLOGY

System Modelling and State Estimation of Cell Core Temperature

Master's thesis in Systems, Control and Mechatronics

Mir Arash Keshavarz Kelachayeh
Yuhui Bi

DEPARTMENT OF ELECTRICAL ENGINEERING

CHALMERS UNIVERSITY OF TECHNOLOGY
Gothenburg, Sweden 2023
www.chalmers.se

Master's thesis in Systems, control and mechatronics
2023

System Modelling and State Estimation of Cell Core Temperature

Mir Arash Keshavarz Kelachayeh
Yuhui Bi

CHALMERS
UNIVERSITY OF TECHNOLOGY

Department of Electrical Engineering
Division of Systems, Control and Mechatronics
CHALMERS UNIVERSITY OF TECHNOLOGY
Gothenburg, Sweden 2023

System Modelling and State Estimation of Cell Core Temperature
MIR ARASH KESHAVARZ KELACHAYEH
YUHUI BI

Supervisor: Ashkan Pirooz, Volvo Group
Examiner: Torsten Wik, Professor, Electrical Engineering, Chalmers University

Master's Thesis 2023
Department of Electrical Engineering
Division of Systems, Control and Mechatronics (MPSYS)
Chalmers University of Technology
SE-412 96 Gothenburg
Telephone + 46 (0)31-772 1000

Typeset in Microsoft Word
Printed by Chalmers Reproservice
Gothenburg, Sweden 2023

System Modelling and State Estimation of Cell Core Temperature
MIR ARASH KESHAVARZ KELACHAYEH
YUHUI BI
Department of Electrical Engineering
Chalmers University of Technology

Abstract

Li-ion battery cells, as the main energy source component of Electric Vehicles (EV), demonstrate complex electrical, chemical, thermal, and mechanical behaviour. Additionally, they sum up in large quantities to form the overall Energy Storage System (ESS) of targeted applications. Hence, real-time management, monitoring, and control of cells is necessary to ensure safe and efficient operation, which is handled by Battery Management Systems (BMS). Due to strong dependency of batteries to temperature, one of the key tasks of a BMS is thermal management. This masters project aimed at developing a BMS function for battery cells' core temperature estimation to provide more detailed thermal information alongside battery cells' geometry. Two model-based estimation approaches have been implemented using Kalman filtering and sliding-mode observation. Both approaches have been implemented upon electro-thermal cell model derived by second order RC equivalent circuits where the coupled thermal side of the model are either 1D lumped mass, or 2D finite difference types having heat transferred by conduction and convection. While all suggested solutions are shown to be executable in real-time, a detailed comparison for accuracy evaluation is performed. The reference for verification has been Computational Fluid Dynamics (CFD) 3D simulations performed under validated and known thermal parameters for a specific candidate battery cell. The proposed modelling approaches and estimation methods are evaluated in terms of estimation accuracy, performance, and parameter uncertainty. The results showed that the estimation using FDM thermal modelling together with Kalman filter estimation has better correlation with CFD results compared to the lumped thermal modelling using either Kalman filter or sliding mode observer. On the other hand, the lumped thermal model is easy to implement in real-time applications due to having just two state variables, but the FDM thermal modelling has large number of state variables.

Keywords: battery management system (BMS), battery modelling, equivalent electrical model (EEM), equivalent thermal model (ETM), finite difference method (FDM), Kalman filter (KF), li-ion battery (LIB), lumped model (LM), sliding mode observer (SMO), temperature estimation

Acknowledgements

We would like to express our sincere gratitude to all those who have supported and contributed to the completion of this master thesis. First and foremost, we are deeply grateful to our supervisor, Ashkan Pirooz, for his invaluable guidance, unwavering support, and expertise throughout this research journey. His insightful feedback, constructive criticism, and constant encouragement have played a pivotal role in shaping the direction and quality of the thesis.

We would like to acknowledge the assistance provided by our manager and colleagues of BMS team at Volvo. Their assistance with technical support has been instrumental in the successful completion of this research work.

Finally, we would like to express our deep gratitude to our families for their support and encouragement throughout all our studies.

Arash and Yuhui, Gothenburg, June 2023

List of Acronyms

BMS	Battery Management System
CFD	Computation Fluid Dynamics
CKF	Cubature Kalman Filter
EC	European Commission
ECM	Equivalent Circuit Model
EEM	Equivalent Electrical Model
EKF	Extended Kalman Filter
ETM	Equivalent Thermal Model
EV	Electric Vehicles
EU	European Union
FD	Finite Difference
FDM	Finite Difference Method
FEM	Finite Element Method
FFLS	Forgetting Factor Least Square
FUDS	Federal Urban Driving Schedule
FVM	Finite Volume Method
HEV	Hybrid Electric Vehicles
JKF	Joint Kalman Filter
Li	Lithium
LIB	Lithium-Ion Battery
Ni-Cd	Nickel-Cadmium
Ni-MH	Nickel-Metal Hydride
OCV	Open Circuit Voltage
PDE	Partial Differential Equations
RC	Resistor-Capacitor
SMO	Sliding Mode Observer
SOC	State-Of-Charge
UKF	Unscented Kalman Filter
UAC	Urban Assault Cycle

Contents

Chapter 1: Introduction

1.1 Background

Nowadays, climatic change, driven by human activities (especially greenhouse gas emissions), has significant direct negative effects on the environment and contribute to over 160,000 deaths per year from side effects associated with climate change [1]. In addition, the European Commission (EC) records show that the past five years were the hottest years registered, with an increase of 1.1℃ of global average temperature above preindustrial levels by 2019. Therefore, EC applied an emission reduction target of greenhouse gas by 2030 (taking 1990 as a reference) at least 55% [2]. So far, the world relies heavily on fossil fuels, such as oil, natural gas, and coal, which provide almost 80 percent of the global energy demands, to meet its energy requirements. In fact, energy and environmental issues have been challenging for the world's automotive industry for a long time. The energy transition implies replacing fossil fuels by alternative renewable energy sources such as solar, wind, ocean, biomass, etc. Consequently, one of the main challenges of the modern society is the so-called energy transition for reducing the global warming due to the huge amount of exhausted carbon dioxide that will devastate our planet [3].

These causes and consequences have motivated researchers, scientists, and engineers to look for more efficient, cheaper, and environmental-friendly alternatives for energy sources. Since the vehicles emission is one the main cause of the sustainability challenges, several alternatives, such as Electric Vehicles (EV) and Hybrid Electric Vehicles (HEV), are proposed, which are attractive for sustainability aspects. However, the hybrid vehicles were not economical until the late 1990s due to the cost and limited battery performance, numerous hybrid vehicles came to market after 2000, for example, Ford Escape Hybrid. In fact, EVs and HEVs have improved significantly, due to recent battery technology which is reflected in Figure 1.1 showing almost an exponential increase of EV registrations in the European Union (EU) [4].

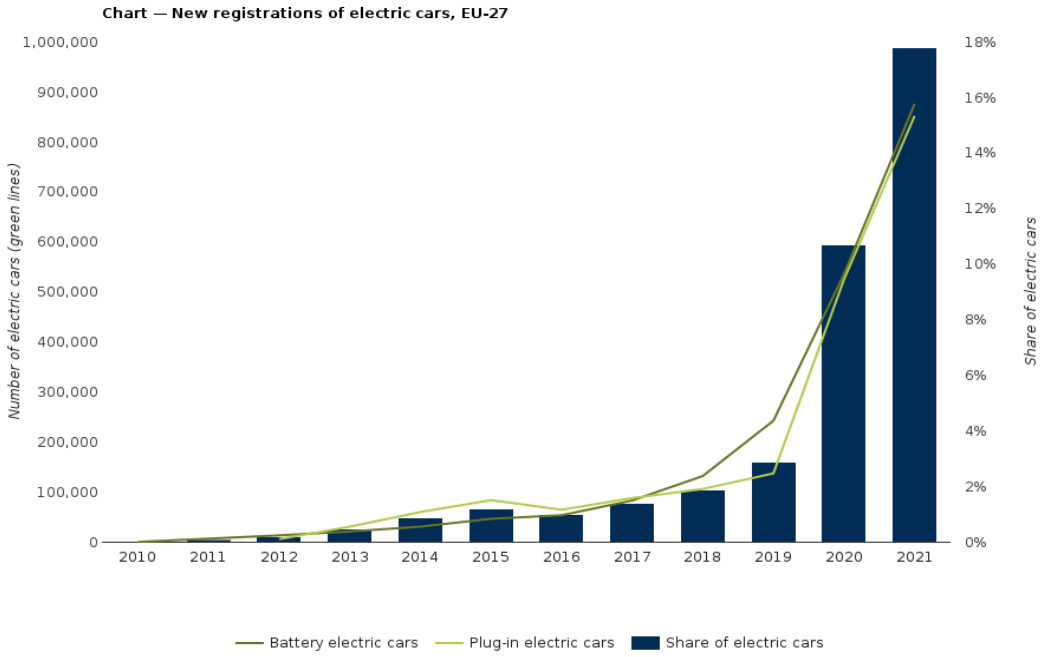

Figure 1.1: Total registration of EVs in 27 countries in EU [4]

Although many battery technologies are currently being analyzed for EVs and HEVs, the focus has been mainly on lead-acid, Nickel-Cadmium (Ni-Cd), Nickel-Metal Hydride (Ni-MH) and Li-ion battery technologies. Today, most EVs are powered by Lithium-Ion Batteries (LIBs). Ni-MH batteries are widely used in HEVs owing to their high charge-and-discharge rate, cycle life and environmentally friendly features. However, the application of Ni-MH batteries in EVs is limited because they have low voltage and are unsuitable for parallel connection [5]. During the last 15 years, LIBs have dominated the advanced energy sources by powering modern portable electronics and replaced many other commercial battery systems in the market [6]. LIB has been applied everywhere, from cellphone to power station, from vehicles to aircrafts. The main reasons of the vast utility of LIB are its superiority over other battery systems, namely, high voltage, high-energy density, longer lifetime, rechargeable and low self-discharge. Although, EVs and HEVs can compete with conventional vehicles in terms of performance and cost with much less environmental issues, their efficiency depends mainly on proper battery management. Hence, EVs use a Battery Management System (BMS) to control and manage the battery systems in a safe and efficient way.
One of the key functions of BMS is thermal management, and consequently, high temperature is one of the crucial parameters that should be monitored to ensure battery safety. Moreover, the battery temperature during the processes of charging and discharging directly affects the operation performance of EVs, such as life cycle, efficiency, reliability, and safety. In addition, under some operating conditions, the maximum temperature difference between the battery surface and its core can be 10 °C or more [7]. Hence, the core temperature may reach a thermal critical point earlier than the surface temperature. Thus, the temperature inside the battery cell (core temperature) is one of the important battery variables that should be monitored during operation to avoid safety issues and have a more precise estimation of other battery states. Furthermore, embedding a sensor inside a battery cell appears not to be economical in vehicle mass production. However, Computational Fluid Dynamics (CFD) can also be used to calculate the temperature distribution, though this method is not suitable for on-board application. The purpose of this thesis is to design an observer, such a Kalman filter, to estimate the temperature inside the cell based on a simplified battery electro-thermal model. Furthermore, other types of observers, such as Sliding Mode Observer (SMO), is also implemented. In addition, the cell thermal modeling is done in two different ways, i.e. a lumped model and by finite differences. Based on problem complexity, computational time and other factors, the efficiency and performance of the Kalman filters and the sliding mode observers together with the mentioned thermal models are investigated.

1.2 Aim of the thesis

The aim of this project has been to build an observer to estimate the cell core temperature by using an electro-thermal model of battery. The electrical part of the model is a second-order RC (Resistor-Capacitor) model. To estimate the core temperature, the observer is designed based on cell thermal modelling in which the cell heat transfer is modelled by either a lumped model or a finite difference model. The overall procedure includes one-dimensional and two-dimensional heat transfer modelling and simulation, and observer design.

1.3 Thesis outline

Chapter 2 includes a brief introduction to battery basics, LIBs and BMS. The key battery parameters, such as C-rate, capacity, State-Of-Charge (SOC), Open Circuit Voltage (OCV) and terminal voltage, are briefly described in this chapter.
In Chapter 3, the theory of convection and conduction heat transfer modelling, including lumped mass model, finite difference modelling, the methods for electro-thermal modelling of battery as well as estimation methods, such as the Kalman filter and the sliding mode observer, are described.
In Chapter 4, thermal modelling such as lumped mass model, finite difference model of cell as well as estimation methods (Kalman filter and sliding mode observer) in MATLAB and Simulink are presented.
Chapter 5 represents the comparison and validation of estimation results with CFD simulations. Finally, Chapter 6 covers conclusion and some proposals for future works.

1.4 Method

In this thesis, the cell is represented by an electro-thermal model in which the electrical model is coupled with a thermal model to provide the necessary data such as heat generation. The electro-thermal parameters, such as SOC, open circuit voltage, heat capacity, conduction, and convection resistance, etc., will be provided through experiments or found from literature.

At first, the thermal part of the electro-thermal model is done using two different modelling approaches which are the lumped model and finite difference model. The electrical model is a second-order RC model. After building the thermal model and connecting it with the electrical model, a robust and suitable estimator, such as a Kalman filter or other types of observers can be designed based on complexity of problem, efficiency and required accuracy to estimate the cell core temperature. Furthermore, the estimation results are compared with finite difference, finite element solutions at 1C and 2C rates. At the end, the results are validated by CFD simulations at 1C charge rate.

Chapter 2: Introduction to battery system

2.1 Lithium-Ion Battery (LIB)

The lithium-ion battery was first proposed by M.S. Whittingham at Exxon in 1970s where he discovered the concept of intercalation electrodes using titanium sulfide as the cathode and lithium metal as the anode [6]. Goodenough was the first to patent $LiCoO_2$ as a lithium intercalation cathode material in 1980 and H. Ikeda of Sanyo was the first to patent an intercalation material in an organic solvent such as graphite in 1981. I. Kuribayashi and A. Yoshino developed a new cell design using an intercalation carbon anode and a $LiCoO_2$ cathode and filed patents worldwide. In 1991, Sony Energy Inc. began to produce commercial lithium-ion cells under the leadership of Yoshio Nishi [6]. Soon after commercialization, the LIBs began to appear as a popular choice in electric devices due to their high specific energy, long life and so on. However, LIBs have been primarily used for portable electronics, such as mobile and notebook computers as shown in Figure 2.1. Quite recently, its utility has been extended to electric drive vehicle.

Figure 2. 1: LIB of smartphone

Figure 2.2 illustrates LIB packs on a typical Volvo BEV truck. Each battery pack consists of hundreds of lithium-ion cells linked together. On the right side, there are five battery packs of LIB.

Figure 2.2: LIB packs on a typical Volvo BEV truck [8],[9] ©Volvo Group

As shown in Figure 2.3, the higher volumetric and gravimetric energy storage capability are main features of the LIB systems compared to the conventional sealed Nickel-Cadmium (Ni-

Cd), Nickel-Metal Hydride (Ni-MH) batteries. Therefore, LIB is the most common choice for vehicle battery packs today.

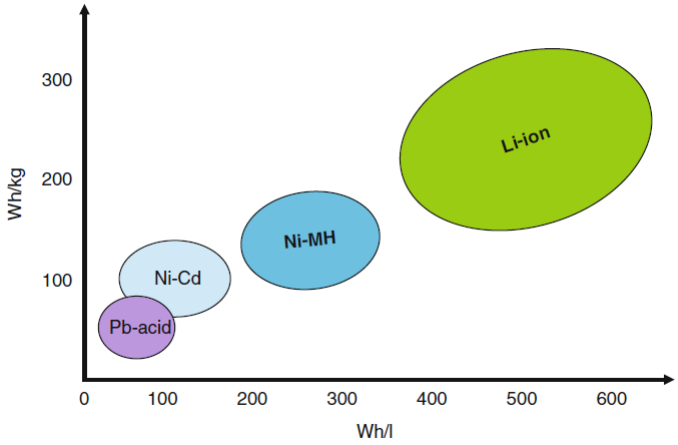

Figure 2.3: Volumetric energy density (Wh/L) and gravimetric energy density (Wh/kg) for major rechargeable battery systems [6]

The main components of a typical LIB cell are negative electrode (or anode), positive electrode (or cathode), and electrolyte. The cell shape design of LIB cells can be cylindrical, prismatic, and pouch.

In a typical LIB, the cathode is composed of a thin layer of powdered metal oxide (e.g., $LiCoO_2$) coated on aluminum foil and the anode can be a thin layer of powdered graphite mounted on a copper foil. The two electrodes are separated by a separator soaked in an electrolyte made of $LiPF_6$ salt dissolved in a mixture of organic solvents such as ethylene carbonate, ethyl methyl carbonate, or diethyl carbonate.

During discharge, the lithium ions are removed from the negative electrode moved through the electrolyte and intercalated into the positive electrode. The opposite happens during charging in which lithium ions deintercalated from the positive electrode and gets intercalated into the negative electrode. Figure 2.4 shows the schematic representation of the operation of a lithium-ion cell during the discharge process.

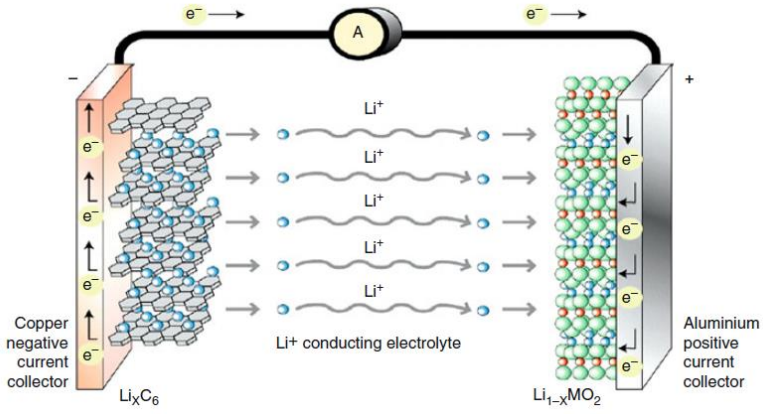

Figure 2.4: Schematic representation of Li-ion cell operating mechanism during discharge [6]

The positive electrode half-cell reaction (with charging being forward) can be given as follows:

$$LiCoO_2 \leftrightarrow Li_{1-x}CoO_2 + xLi^+ + xe^-$$

where the forward reaction corresponds to charging and the reverse reaction occurs during discharge. The negative electrode half-reaction (with charging being forward) is

$$xLi^+ + xe^- + 6C \leftrightarrow Li_xC_6$$

where x refers to moles of lithium. Therefore, the overall cell reaction can be written as

$$LiCoO_2 + 6C \leftrightarrow Li_{1-x}CoO_2 + Li_xC_6$$

2.2 Battery Management System (BMS)

Generally, the specification of two cells can be slightly different even if they are produced in identical conditions with advanced quality check. When the battery pack is new, the cell differences may not be important but in the long term, the charge and discharge cycles make them more important. In addition, in case of having tens or hundreds of series-connected cells, the defected cell can be easily disguised. Therefore, it is essential to monitor the batteries individually and detect a defected cell as soon as possible. In order to ensure the safe operation of a battery system to supply energy to an electric vehicle, a BMS is needed to control and manage the battery system in a safe and efficient way.

The basic functions of a BMS include battery data acquisition, modelling and state estimations, charge and discharge control, fault diagnosis and alarm, thermal management, balance control, and communication. The functional structure diagram of an advanced BMS is shown in Figure 2.5. Therefore, developing advanced and intelligent BMS for the lithium-ion battery systems to control the mentioned functions of BMS is essential for industrialization and marketization of electric vehicles. The main technical difficulties restricting the development of battery management technology can be concluded in the following three aspects: (1) The lithium battery system is highly nonlinear (2) The internal states of the battery such as temperature inside the cell, cannot be obtained by direct measurement (3) The inconsistent performance of a cell directly influences the efficiency of the entire battery system. Therefore, advanced BMSs needs accurate modeling and state estimation to ensure reliable and safe performance of battery system.

BMS key features can be seen in Figure 2.6, and one of the key parts of BMS is thermal management, where high temperature is one of the crucial parameters that should be monitored to ensure battery safety. Hence, monitoring and regulating the cell temperature within optimal operating range prolongs battery life.

In addition, under some operation conditions, the maximum temperature difference between the battery surface and core can be 10 °C or more [7]. Hence, the core temperature may reach a thermal critical point earlier than the surface temperature. Thus, the temperature inside the battery cell (core temperature) is one of the important battery parameters that should be monitored during operating conditions to avoid security issues and proving a more precise estimation of other battery states. Despite the fact that embedding a sensor inside a battery cell is under research and development, it still needs time and investment to reach mass production of such idea.

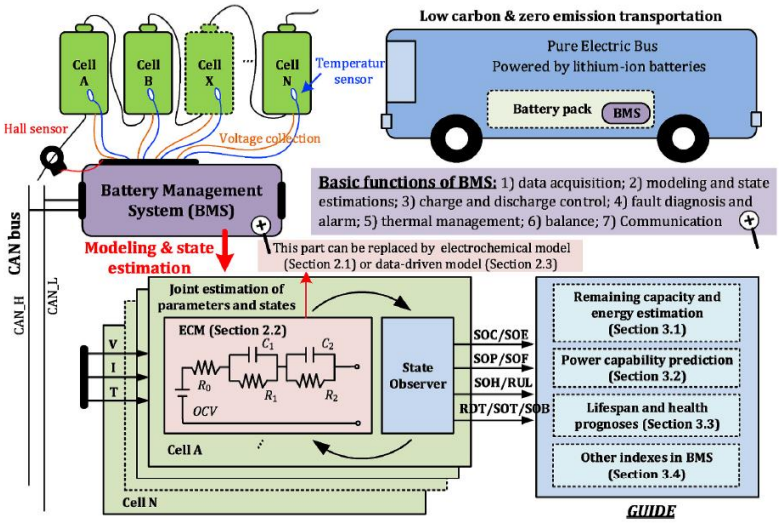

Figure 2.5: An advanced BMS's functional structure diagram [11]

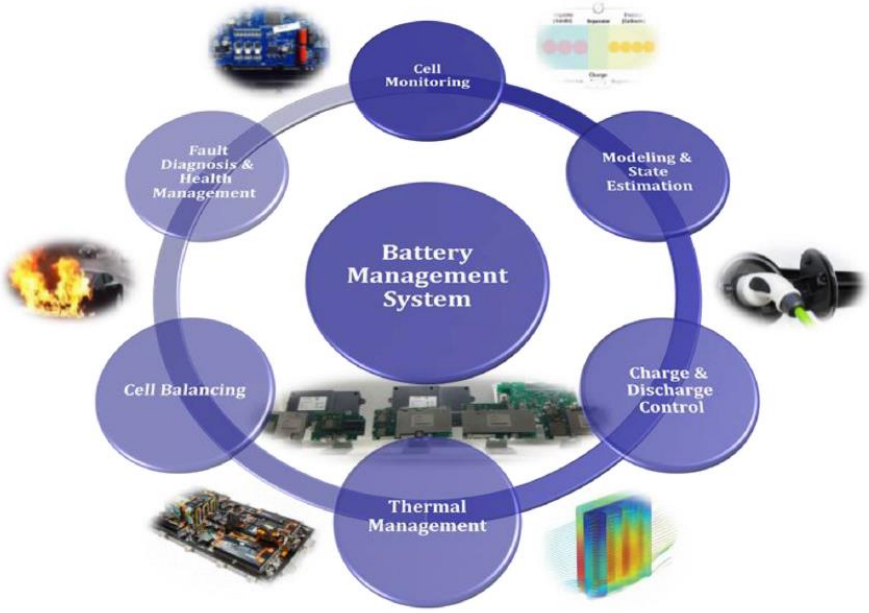

Figure 2.6: BMS's key features [11]

2.3 Battery cell characteristics

There are several key parameters that describe the specification and performance of batteries. In this section, some of these parameters that will be used in the following chapters of this thesis are described.

- Terminal Voltage and Open-Circuit Voltage

The battery voltage can refer to two kinds of voltage which are terminal voltage (V_T) and open-circuit voltage (V_{OCV}). The terminal voltage is the voltage that can be measured at the cell's terminals at any time. In contrast, open circuit voltage is the internal voltage of the cell generated by the electrochemistry, it can be measured only when the battery is at rest.
As shown in Figure 2.7, due to cell impedances and resistances, the terminal voltage is different from V_{OCV}.

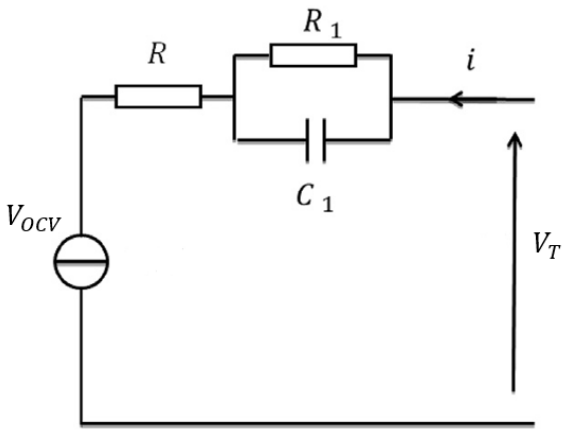

Figure 2.7: First order equivalent circuit model of a battery cell [12]

Figure 2.8 shows that the terminal voltage is equal to open circuit voltage, when the cell has been resting for some time at zero current. In addition, open circuit voltage and terminal voltage are affected by several factors, such as its State-Of-Charge (SOC) and temperature.

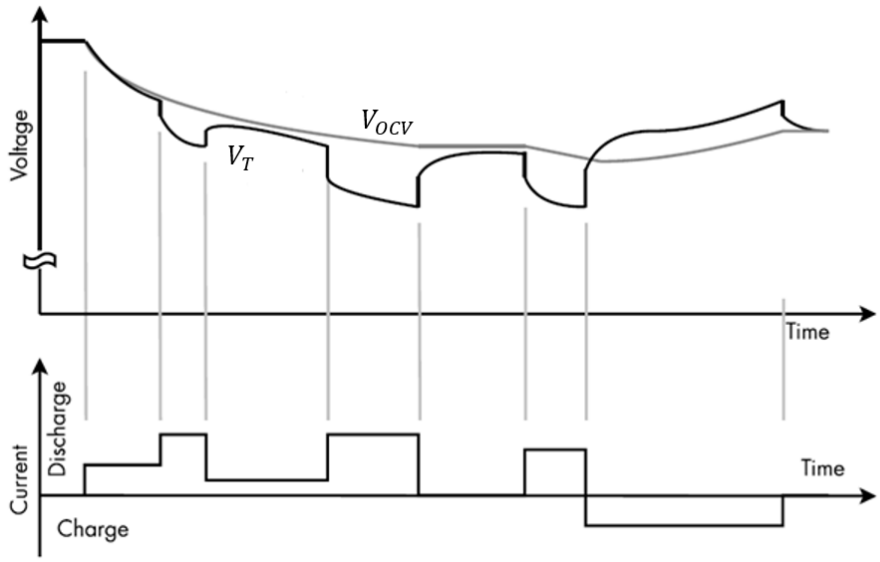

Figure 2.8: Terminal voltage and V_{OCV} in various charge-discharge conditions [13]

It can be seen in Figure 2.8 that in steady-state discharge current, the terminal voltage is below V_{OCV}. On the other hand, with a steady-state charge current, the terminal voltage is above the V_{OCV}. In no current condition, the terminal voltage slowly approaches V_{OCV}, but never quite reaches it due to hysteresis. The hysteresis phenomena can be defined as the terminal voltage never reaching V_{OCV}, even after a long relaxation time at zero current.

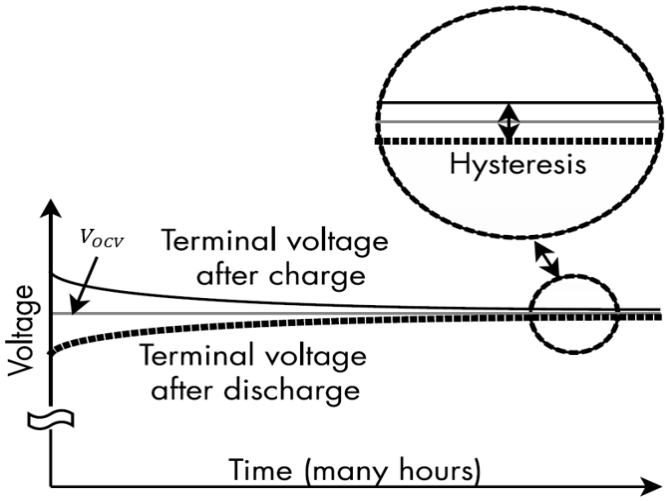

Figure 2. 9: The hysteresis in charge and discharge mode [13]

It can be seen in Figure 2.9 that the terminal voltage is slightly less than V_{OCV} in discharge mode after many hours. On the contrary, the terminal voltage is a little greater than V_{OCV} in charge mode. The hysteresis caused by the inability of ions to diffuse evenly in the cell terminal such that the lithium ions bunch up near an electrode when being added to that electrode or become sparse near an electrode when being taken from that electrode [13].

- State Of Charge (SOC)

The SOC shows the battery remaining capacity (Q_{rem}) as a percentage of the maximum available capacity. SOC formulation can be given as shown in Eq. 2.1.

$$SOC = \frac{Q_{rem}}{Q_{max}} \times 100 \qquad (2.1)$$

Q_{rem} : The capacity of the battery as it discharges from the present state to the fully discharged state.
Q_{max}: The capacity of the battery at full charge state

The SOC can vary in the range [0-100] % in which the full discharge SOC=0 and full charge state SOC=100 %. From chemical point of view, SOC represents the concentration of lithium ions in the negative electrode. Figure 2.10 shows the variation of V_{OCV} versus SOC in which it can be seen that different organizations have different definition for SOC range.

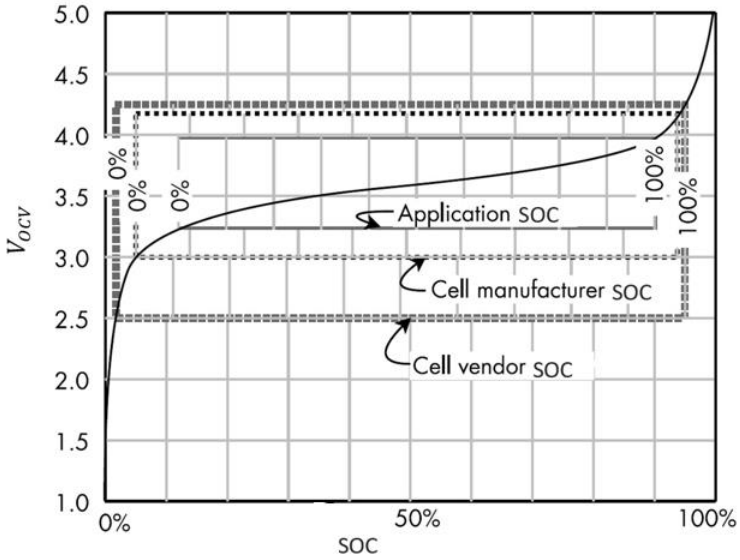

Figure 2.10: Open circuit voltage versus SOC for a specific cell [13]

- Capacity

Capacity, measured in Ah, is the total charge that a cell or battery can store. It is usually measured in Ah. It can be defined as

$$Q = \int_{SOC=0}^{SOC=1} i(t)dt \qquad (2.2)$$

- C-Rate

C-rate can be defined as the rate at which a battery is charged or discharged relative to its capacity. It can be explained in this way, 1C means the battery can be fully charged (in a specified current) in one hour. C-rate higher than 1C correspond to fast charge. For example, 2 C means twice faster, which gives full charge in half an hour. In a similar way, 0.5 C means a slow charge condition, that gives a full charge in two hours.

2.4 Modelling and estimation

Since one of the key parameters of a cell is its core temperature, this parameter should preferably be controlled and monitored in an intelligent battery management systems. During charging/discharging and operating condition, the heat generated by chemical reactions inside the cell causes the temperature to rise. Hence, a cognitive thermal management system is required to monitor the battery temperature regularly. As mentioned earlier, the installation of a sensor inside the cell is expensive and it also brings some side effects for example sensor isolation which leads to discovering an alternative way to measure the temperature. Consequently, using observers can be a suitable alternative to calculate the temperature rise inside the cell. In order to design an observer, it is essential to model the heat transfer inside the cell in such a way that it represents the temperature gradient from surface to the internal parts of cell. There are several methods for modelling the heat transfer, for example, lumped model and finite difference model which will be discussed in the next chapters.

2.5 Literature review

Nowadays several methods for estimating the cell core temperature have been developed, including numerical methods and the simplified lumped thermal models. While numerical techniques, such as finite element method and Finite Volume Method (FVM), can predict the detailed temperature distribution, these kinds of methods are not suitable for online vehicle applications due to their computational demand. One of the most popular and efficient battery models that are suitable for onboard applications, is Equivalent Circuit Models (ECM). These kinds of models can be implemented in cell thermal modelling as well as electrical modelling in which a series of equivalent Resistor-Capacitors (RC) are connected to represent the cell behaviour in real condition.
Many works have been focused on temperature estimation using Kalman filter or other types of observers, such as Luenberger observer using lumped thermal models in which conduction and convection heat transfer are modelled with equivalent thermal resistances. For example, Lin et al. [14] modelled heat transfer in a cylindrical cell by a two-state lumped thermal model in which conduction and convection was represented by equivalent electrical resistance, and designed an observer to estimate the core temperature. They derived model parameters such as cell electrical resistance, convection and conduction resistances using a least square identification method using UAC (Urban Assault Cycle) test data. In addition, they simulated internal heat generation as current squared times the identified cell internal resistance. At the end, they designed an observer to estimate the cell's core temperature and validated the results with measurements. As an improvement in thermal modelling, Sun [15] et al. designed a Kalman filter for a two-state lumped thermal model of a prismatic cell to estimate the internal temperature considering a heat source generated by entropy variation and overpotential of the cell. The model parameters, conduction and convection resistances and capacitance, are identified through a current pulse test. The investigation of heat generation originating from overpotential as well as entropy variation at 2C, 1.5C and 1C charge and discharge shows that the overpotential contribution is dominant in the heat generation. The comparison of estimation results with measurement (by insertion of thermocouple inside the battery) as well as surface temperature demonstrated that the surface temperature cannot reflect the inside temperature and internal temperature rises with increasing C-rate.

Some researchers such as Dai et al. [16] and Chen et al. [17], proposed a JKF-based (Joint Kalman Filter) in which the convection resistance is treated as a time varying variable. To do

so, Dai et al [16] modelled the battery heat transfer by a two-state lumped model and designed a Kalman filter in two cases, the first one (KF-based), for only estimation of cell temperature, and the second one (JKF) for estimation of time-dependent convection heat transfer coefficient as well as core temperature. They modelled internal heat by including ohmic losses as well as the entropic heat (reversible heat). By conducting 2C discharge/charge test, they showed that the entropic heat contribution is only a small portion of the heat generation and hence it is reasonable to consider ohmic loss as main source of heat generation. The lumped model parameters are identified by a least squares method based on experimental data. They carried out estimation in 0.5C, 2C and FUDS (Federal Urban Driving Schedule) case studies. They show that, due to the inaccurate convection resistance, there exists an obvious difference between the core temperature and measured temperature obtained by the KF-based estimator. The comparison of joint estimator with measurements indicated that the JKF has better performance to track the temperature due to estimation of convection heat transfer coefficient so that the error of KF- and JKF-based estimator is less than 1.8 ℃ and 1 ℃ respectively. In addition, Chen et al [17] proposed a JKF to estimate the core temperature and convection resistance using an electro-thermal model in which the second order electrical RC model was coupled to the two-state lumped thermal model. They identified the electrical RC parameters as functions of SOC and temperature in both charge and discharge conditions. In addition, they included the contribution of reversible and irreversible heat generation. They showed that the estimated core temperature has better correlation with measurements at various charge and discharge rates at different ambient temperatures.

In order to obtain a comprehensive description of cell behavior for real-time applications, some researchers estimated SOC and cell Ohmic resistance in addition to internal temperature. For example, Zhang [18] et al., developed an online Kalman filter estimator for internal temperature, SOC and Ohmic resistance based on a simplified electro-thermal model in which the electrical part was a first-order RC model, and the thermal model was also an equivalent two-state lumped model in which the cell heat transfer was modelled by an equivalent RC model. In addition, they considered the cell Ohmic resistance as temperature dependent. They showed that in low-current self-heating tests (e.g., less than 1 C), the battery internal temperature will not differ much from the surface temperature. However, in high current tests, the temperature difference was around 11 °C. They also found that there was a bias between the estimated and measured temperature due to the inaccuracy of the thermal model, which originates from time-varying behavior of the convection heat transfer resistance. Some researchers proposed an enhanced temperature estimation approach. For example, Pang H. et al. [19] proposed a novel estimation procedure for the internal and surface temperatures of a cylindrical cell using an Extended Kalman Filter (EKF) based on an electro-thermal model in which the electrical RC model was of second order. In fact, the novelty of their approach can be described in this way that, instead of using measured surface temperature, the measured terminal voltage of the cell was used as measured data for EKF estimation. Moreover, they used “Forgetting Factor Least Square (FFLS)” method to identify temperature dependant RC parameters and open circuit voltage. Finally, they verified the accuracy of their proposed method at different ambient temperatures by reduction in estimation error compared to measurements.
In addition to lumped thermal model, S. Sattarzadeh et al. [20] used a different approach for thermal modelling and estimation for a pouch cell where they used a two-dimensional finite difference method to model the heat transfer in the cell with non-uniform heat distribution and a sliding mode observer for estimation. They examined the performance of observations in two case studies, in the first one, multiple temperature sensors were used and in the second one, there was only one temperature sensor.

Regarding the mentioned research, it can be concluded that a two-state lumped thermal model together with an equivalent electrical circuit model has been widely used to estimate the cell temperature. Although the numerical methods are heavy in terms of computational time, the lumped models are simple and easy to implement without sacrificing accuracy, thus being suitable for onboard applications. Furthermore, it can also be seen that various identification methods, such as least squares can be implemented to derive the lumped model parameters. The accuracy of the lumped model, as well as the estimations depend on the accuracy of the lumped model parameters. Moreover, it can be inferred that Kalman filter is one of the most common estimation methods for temperature estimation and cell parameters, such as SOC, internal cell resistances and so on. Therefore, it was decided to use a lumped model and finite differences for the thermal modelling, and at the next step, Kalman filter and sliding mode observer were implemented for temperature estimation. The details of this procedure will be described further in the following chapters.

Chapter 3: Theory of cell modelling, heat transfer and estimation

3.1 Battery modelling methods

There are multiple battery model types because of various behaviors, such as chemical, electrical, thermal, and mechanical models. For BMS applications, the most common method is electro-thermal model using equivalent circuit modeling.
Here, starting from the classical electro-thermal model, several modelling methods are reviewed.

3.1.1 Equivalent Circuit Models (ECM)

The ECMs are composed of resistances and capacitances in different configurations. In fact, they are the most popular methods in real time applications due to simple structure and ease of parameter identification. In literature, ECMs can be divided into two groups: the integer-order models and fractional-order models.
Different models have different precision depending on the number and configuration of the resistances and capacitances in the circuit. A brief introduction of ECMs will be presented in the following.

- Integer-order models

The simplest battery model is shown in Figure 3.1, and is an internal resistance battery model (Rint), implemented by ADVISOR in 1994 [21] . It consists of a voltage source (V_{OCV}) and a resistor (R_0). These parameters vary with SOC and temperature. Although this model is simple and is easy to implement, it cannot describe dynamic polarization phenomena within a battery. Therefore, it is not suitable for electric vehicles, or any other application, that needs high accuracy.

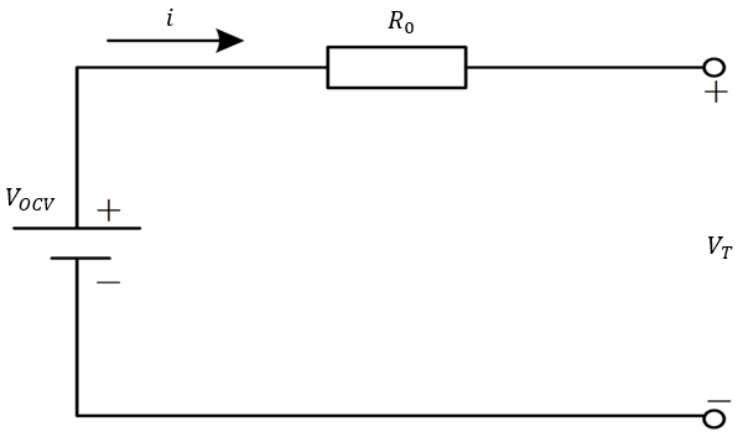

Figure 3.1: Rint model

A modified form of the Rint model is the so-called Thevenin equivalent circuit or first-order RC-model [21]. As shown in Figure 3.2, this model is composed of a voltage source represented by V_{OCV}, an Ohmic resistance R_0 that models the internal resistance and one R_1C_1 pair that describes the polarization phenomena. In principle, C_1 represents the polarization of the metallic electrodes and R_1 refers to the resistance in contact area of the electrodes with the electrolyte. This model can simulate battery behaviors with quite high fidelity, as validated by experimental results [22].

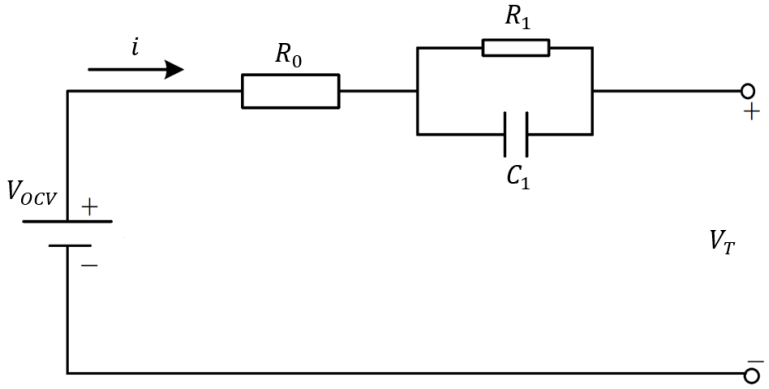

Figure 3.2: Thevenin model, or first-order RC model [21]

However, because the first-order *RC* model considers polarization in only one *RC* pair, it is not accurate at the end of charge and discharge. A second-order *RC* equivalent circuit model has therefore been proposed to approximate the battery dynamic performance and a voltage error less than 40 mV has been achieved [22]. The second order model simulates the polarization by two different *RC* pairs that are connected in series, as shown in Figure 3.3. It is generally agreed that the first and second *RC* pairs model the concentration polarization and electrochemical polarization, respectively.

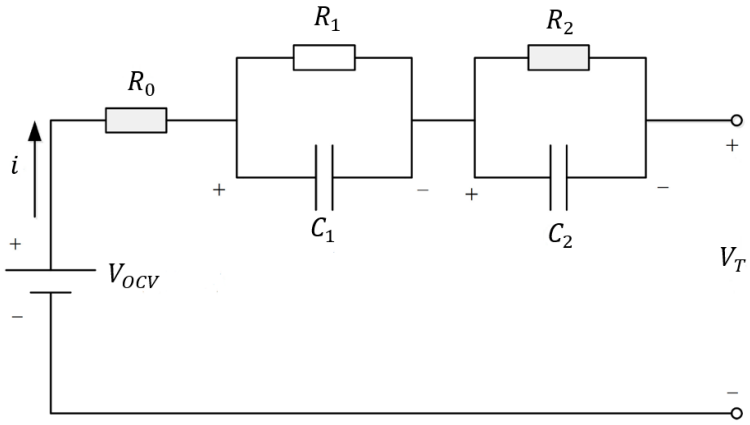

Figure 3.3: Second order RC model [23]

In this work the second order model is used to simulate the electrical part of model. There are, however, other ECMs such as, hybrid model, PNGV model, advanced Rint-Rp, which are all described in [24].

3.1.2 Other battery models

- Electrochemical models

The electrochemical models are based on first principal modelling and usually rely on simultaneously solving a large number of Partial Differential Equations (PDEs). Due to their complexity, they have tremendous requirements of memory and computational power to solve for the unknown variables. In addition, the electrochemical models do not give reliable results

without having accurate model parameters. To achieve this online is still an unsolved problem. Since the parameters change with age, they are not ready to be applied in real-time applications. This method is therefore out of the scope of this thesis.

- Data-driven models

This method implements machine learning methods using training data to model the battery system. The data-driven approaches have good performance in many nonlinear problems, through their accuracy depends highly on the training datasets and training methods such that the performance of this method may change from one battery to another. However, these models are simple and easy to implement, but they may have 5-20% inaccuracy due to the non-linear behavior of a battery under a dynamic load profile [25]. This method is also out of the scope of this thesis.

3.2 Heat transfer mechanisms

Heat transfer is thermal energy in transit due to a spatial temperature difference [26]. The energy flow (heat flux) is driven by the temperature difference. Indeed, heat transfer studies the rate of energy transfer in transient condition between materials at different temperatures. On the other hand, thermodynamics deals with the energy required to change a system from one equilibrium (no transient condition) state to another equilibrium. The heat transfer can occur according to three different modes, i.e., conduction, convection, and radiation. An example with boiling water is illustrated in Figure 3.4.

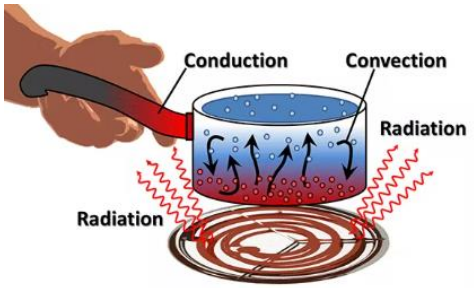

Figure 3.4: Example of heat transfer mechanisms when boiling water [27]

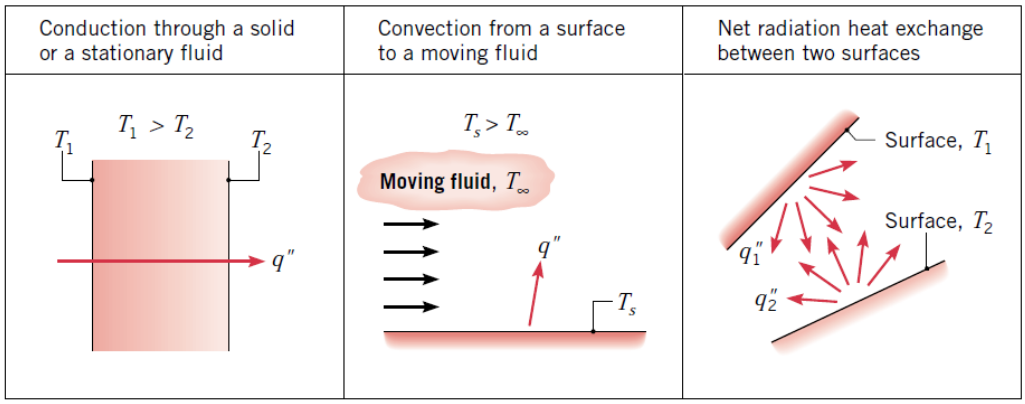

Figure 3.5: Conduction, convection, and radiation heat transfer modes [26]

The mentioned types of heat transfer modes can also be seen in Figure 3.5. The conductive heat transfer is caused by a temperature gradient within a media. Convection refers to heat transfer that will occur between a surface and a moving fluid when they have different

temperatures. Radiation is energy exchange between two materials by electromagnetic waves, and will not be considered in this thesis.

3.2.1 Conduction

When there is a temperature gradient in a body, there is an energy transfer from the high-temperature region to the low-temperature region as shown in Figure 3.6.

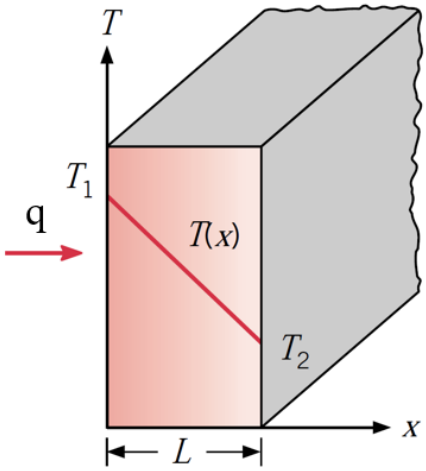

Figure 3.6: One-dimensional heat transfer by conduction [26]

The heat transfer flow can be described by Fourier's law

$$q = -kA\frac{dT}{dx} \tag{3.1}$$

where T is temperature in K or $°C$. q is the heat transfer rate in J/s or W, A is the cross-section area in m^2, and k is thermal conductivity in $W/m°C$. The negative sign with $\frac{dT}{dx}$ on the right-hand side implies that the heat flows along a negative temperature gradient, in other words, the heat flows from high temperature to low temperature area. For the example in Figure 3.6, Eq. 3.1 can be rewritten as

$$q = \frac{-\Delta T}{\frac{\Delta x}{kA}} = \frac{T_1 - T_2}{\frac{L}{kA}} \tag{3.2}$$

By considering $\frac{L}{kA} = R$ and using Ohm's law analogy, the heat transfer can be interpreted as an electrical circuit in which q (heat transfer rate) refers to current, ΔT (temperature gradient) represents the voltage and $\frac{L}{kA}$ represent the thermal resistance. The unit for thermal resistance is $°C/W$. So, heat transfer can be modelled as

$$\text{heat flow} = \frac{\text{thermal potental difference}}{\text{thermal resistance}} \tag{3.3}$$

By applying the Ohm's law analogy to a wall with different material, as shown in Figure 3.7, Fourier's law can be rewritten as

$$q = \frac{\Delta T_{overall}}{\sum R_{th}} = \frac{T_1 - T_4}{\frac{\Delta x_A}{k_A A} + \frac{\Delta x_B}{k_B A} + \frac{\Delta x_C}{k_C A}} \tag{3.4}$$

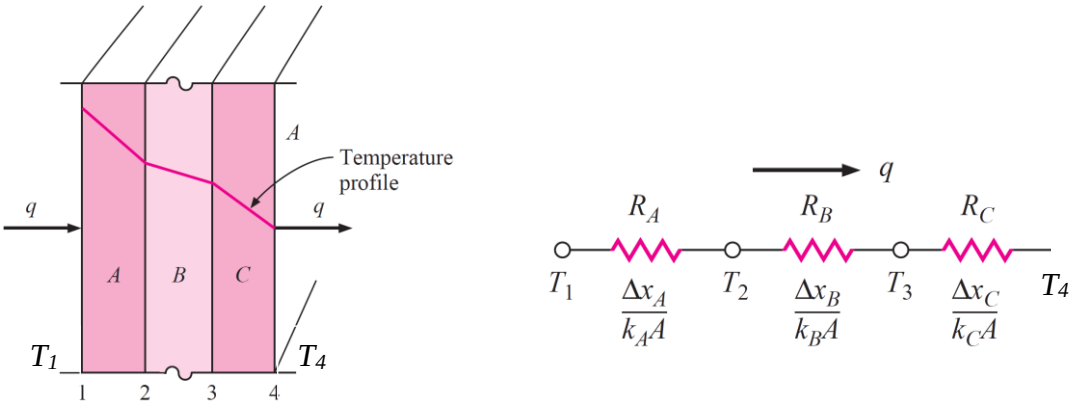

Figure 3.7: One-dimensional heat transfer through a composite wall and the electrical analogy [28]

In a lumped model, the battery is considered as being a combination of the material inside the battery (e. g. anode, cathode, electrode) and the housing (or shell) around the battery. Thus, heat transfer model inside the cell can be derived by using this methodology, which will be discussed further in the next chapter.

Now, generalizing to three space dimensions an energy (heat) balance for the case of constant thermal conductivity and homogenous internal heat source gives

$$\frac{\partial^2 T}{\partial x^2} + \frac{\partial^2 T}{\partial y^2} + \frac{\partial^2 T}{\partial z^2} + \frac{\dot{g}}{k} = \frac{1}{\alpha}\frac{\partial T}{\partial \tau} \tag{3.5}$$

where $\dot{g}$ is the internal heat source per volume (w/m^3) and $\alpha = \frac{k}{\rho c}$ is thermal diffusivity of the material. It represents the heat diffusion inside the material such that the larger α is, the faster heat will distribute through the material.

3.2.2 Convection

Convection is a mechanism of energy transfer occurring by motion of fluid or gas over a surface, as shown in Figure 3.8. According to Newton's law of cooling, convection can be formulated as

$$q = hA(T_w - T_\infty) \tag{3.6}$$

In which h $(W/m^2°C)$ is the convection heat transfer coefficient. The expression $(T_w - T_\infty)$ stands for the temperature difference between the surface and ambient. The convection formula can be rearranged as

$$q = \frac{T_w - T_\infty}{\frac{1}{hA}} \tag{3.7}$$

where $R = \frac{1}{hA}$.

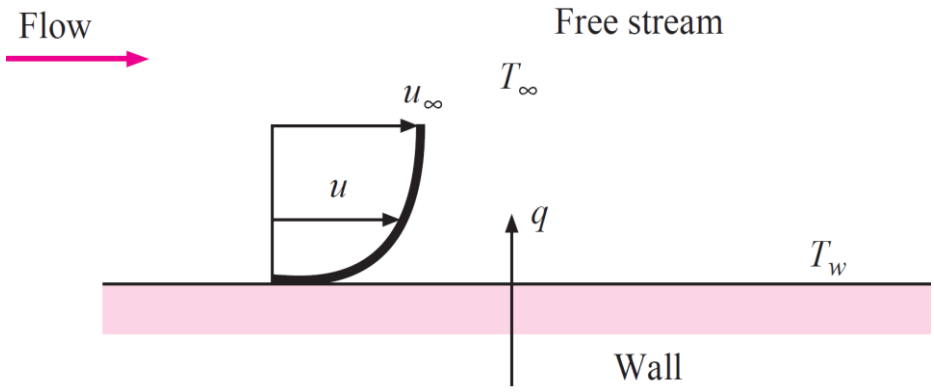

Figure 3.8: Convection heat transfer [28]

In a similar way to that shown for conduction, by using the Ohms law analogy, q represents the current, temperature refers to voltage and R is the convection resistance in $°C/W$. This analogy of Ohm's law will be used for modelling of convection between the cell and ambient temperature in the next chapter.

3.3 Transient heat transfer-formulation and methods

There are several methods for obtaining a mathematical model of transient heat transfer such as lumped method, analytical methods, Finite Difference Method (FDM) and Finite Element Method (FEM). Each method has its own advantages and disadvantages. The analytical solutions try to solve heat partial differential equation using separation of variables, which works in limited cases with simplified geometry and boundary conditions. In addition, the methods that works based on meshing, such as CFD and FEM methods, are difficult to implement in terms of meshing and computation time. Therefore, the lumped method and finite difference method has been implemented in this work for mathematical formulations. The fundamentals of both mentioned methods are described briefly in the following sections.

3.3.1 Lumped model

The lumped model can be defined as a material in which there is no temperature gradient inside, in other words the temperature is uniform during the whole heat transfer process, so the temperature is function of time variable only. It should be noted that lumped modelling is unrealistic because a temperature gradient must exist in a material if heat is to be conducted

into or out of the material. In general, the smaller the physical size of the body, the more realistic the assumption of a uniform temperature throughout the body [28].
Consider a body of arbitrary shape with uniform temperature T placed in a medium at temperature T_∞. Assuming that $T > T_\infty$, the energy balance for time interval dt can be written as

Heat release from body to environment=The decrease in internal energy of body

or

$$-q_{out} = du_{in}/dt$$

In which $-q_{out}$ is the convection heat transfer (or rate of heat release) and $\mathrm{d}u_{in}/\mathrm{d}t$ indicates the rate of internal energy change inside the body. Using Eq. 3.6 and the expression for internal energy, we obtain

$$-hA(T - T_\infty) = \rho V c dT/dt \qquad (3.8)$$

where ρ is the density, V is the volume of the body and c is the specific heat capacity. It can be interpreted as an electrical RC model in which $R = \frac{1}{hA}$ is convection resistance against the heat transfer to the environment and C_{th}=ρcV indicates the heat capacity of the body to maintain internal energy. Considering the circuit shown in Figure 3.9, current flow through capacitor can be expressed as $i_{cap} = C_{th} dV/dt$ and current flow through resistor can be expressed as $i_R = \frac{\Delta V}{R}$.

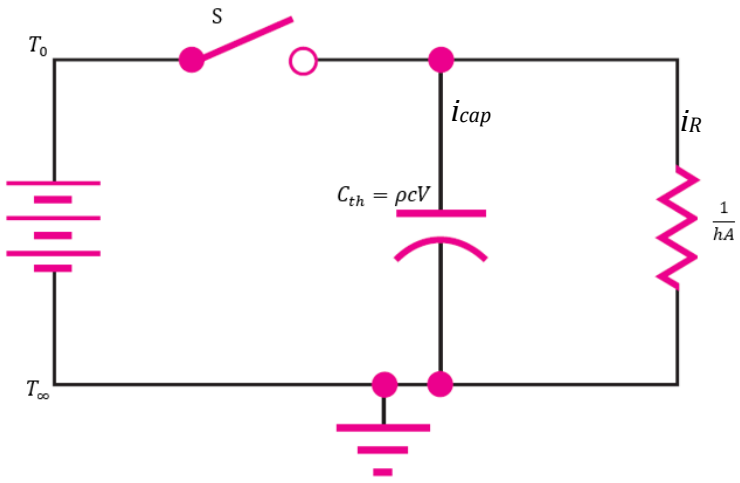

Figure 3.9: The equivalent circuit of lumped model [28]

It can be seen that by having $i_{cap} = i_R$, the Eq. 3.8 can be verified. In fact, the expression $i_{cap} = i_R$ implies the electrical form of energy balance in which the convection heat transfer is equal to the rate of internal energy. This methodology will be used for thermal modelling of cell. The lumped model is expected to yield reasonable results when the following condition is satisfied [26], [28]:

$$Bi = \frac{hs}{k} < 0.1, \qquad s = \frac{V}{A}$$

where Bi is the Biot number, which can also be expressed as

$$Bi = \frac{h\,\Delta T}{\frac{k}{s}\,T} = \frac{convection\ heat\ transfer\ at\ surface}{conduction\ inside\ the\ body} \tag{3.9}$$

or

$$Bi = \frac{s/k}{1/h} = \frac{conduction\ resistance\ inside\ the\ body}{convection\ \ resistance\ at\ surface} \tag{3.10}$$

In fact, the Biot number is the ratio of conduction resistance to the convection resistance. Therefore, a small value of Biot number shows that there is a small resistance inside the body to conduction and, consequently, the temperature inside the body will be approximately uniform.

3.3.2 Finite Difference Method (FDM)

Regarding the mentioned limitations of the lumped model, the numerical method can be used in cases in which the geometry is complicated, or the boundary conditions vary with time. One of the usual numerical methods to solve the heat equation is the finite difference method (FDM). It works based on discretization of differential equation domain and replacing the derivatives in the differential equation by linear algebraic equations. A brief explanation of FDM will be presented in this part. More details of this method can be found in [26], [28].
Under transient conditions with uniform constant properties, the two-dimensional heat equation can be written as

$$\frac{\partial^2 T}{\partial x^2} + \frac{\partial^2 T}{\partial y^2} + \frac{\dot{g}}{k} = \frac{1}{\alpha}\frac{\partial T}{\partial \tau} \tag{3.11}$$

In general, the heat diffusion area can be divided into the elements as shown in Figure 3.10. The subscript *m* and *n* denote the *x* and *y* position, respectively.

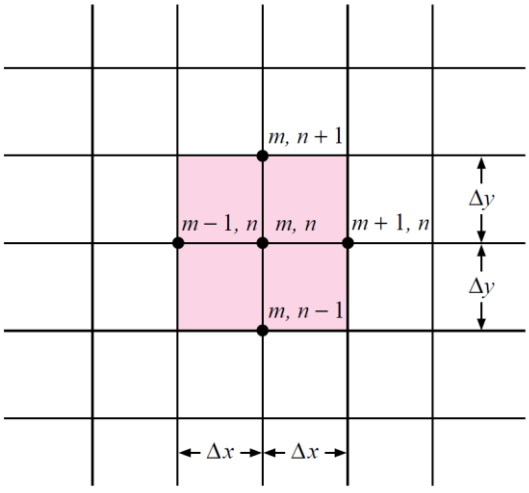

Figure 3.10: The internal nodes of configuration for FDM [28]

The second order partial derivatives can be approximated by

$$\frac{\partial^2 T}{\partial x^2} \approx \frac{1}{\Delta x^2}(T_{m+1,n} + T_{m-1,n} - 2T_{m,n}) \tag{3.12}$$

$$\frac{\partial^2 T}{\partial y^2} \approx \frac{1}{\Delta y^2}(T_{m,n+1} + T_{m,n-1} - 2T_{m,n}) \tag{3.13}$$

The time derivative can be approximated by

$$\frac{\partial T}{\partial \tau} = \frac{T_{m,n}^{p+1} - T_{m,n}^{p}}{\Delta \tau} \tag{3.14}$$

Using Eq. 3.12 to Eq. 3.14 and considering $\Delta x = \Delta y$, the following expression for $T_{m,n}^{p+1}$ can be derived:

$$T_{m,n}^{p+1} = \frac{\alpha \Delta \tau}{\Delta x^2}\left(T_{m+1,n}^{p} + T_{m-1,n}^{p} + T_{m,n+1}^{p} + T_{m,n-1}^{p}\right) + \left(1 - \frac{4\alpha \Delta \tau}{\Delta x^2}\right) T_{m,n}^{p} + \frac{\dot{g}}{\rho c}\Delta \tau \tag{3.15}$$

By definition of the Biot and the Fourier numbers, i.e., $Bi = \frac{h\,\Delta x}{k}$ and $Fo = \frac{\alpha\,\Delta \tau}{\Delta x^2}$, Eq. 3.15 can be written as:

$$T_{m,n}^{p+1} = Fo(T_{m+1,n}^{p} + T_{m-1,n}^{p} + T_{m,n+1}^{p} + T_{m,n-1}^{p}) + (1 - 4\mathrm{Fo})\, T_{m,n}^{p} + \frac{\dot{g}}{\rho c}\Delta \tau \tag{3.16}$$

To ensure stability, the coefficient of $T_{m,n}^{p}$ should always be positive, otherwise the numerical solution will be unstable. This gives

$$stability\ requirement: \qquad Fo \leq \frac{1}{4}$$

In a similar way, as shown in Figure 3.11, the formulation of boundary node and corner node with convection can be derived as Eq. 3.17 (for boundary node), Eq. 3.18 (for corner node), respectively.

$$T_{m,n}^{p+1} = Fo\left(2T_{m-1,n}^{p} + T_{m,n+1}^{p} + T_{m,n-1}^{p} + 2BiT_{\infty}\right) + (1 - 4Fo - 2Fo \times Bi)T_{m,n}^{p} + \frac{\dot{g}}{\rho c}\Delta \tau \tag{3.17}$$

$$stability\ requirement \qquad Fo(2 + Bi) \leq \frac{1}{2}$$

$$T_{m,n}^{p+1} = 2Fo\left(T_{m-1,n}^{p} + T_{m,n-1}^{p} + 2BiT_{\infty}\right) + (1 - 4Fo - 4Fo \times Bi)T_{m,n}^{p} + \frac{\dot{g}}{\rho c}\Delta \tau \tag{3.18}$$

$$stability\ requirement \qquad Fo(1 + Bi) \leq \frac{1}{4}$$

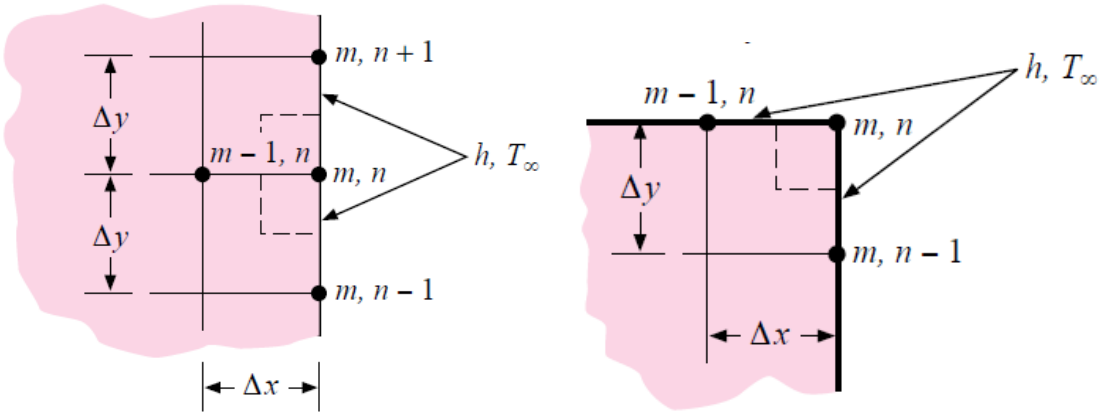

Figure 3.11: The boundary node (left) and corner node (right) [28]

3.4 Heat generation inside battery cells

Bernardi [29] presented a general energy balance formula using the first law of thermodynamics for the battery system taking into account temperature change due to chemical reaction, phase change, mixing effect, electrical work and heat dissipation to surrounding. The detailed form of Bernardi's formulation can be found in [29]. The symbolic form is as follows:

$$Q - VI = \dot{H}_{reaction} + \dot{H}_{mixing} + \dot{H}_{phase\ change} + \dot{H}_{heat\ capacity} \qquad (3.19)$$

In which Q (W) and VI are heat transfer rate to surrounding and electrical work, respectively. With regard to [17], [19] and [30], the contribution of mixing, phase change and heat capacity are negligible. Thus, the simplified formula of heat generation in lithium-ion batteries can be simplified to give:

$$Q = (V_{OCV} - V_t)I + IT\frac{dV_{OCV}}{dT} \qquad (3.20)$$

The first part of Eq. 3.20 is defined as overpotential heat or "irreversible heat source", which is always positive, and it is related to ion movement in the electrolyte and separator and electron flow in the current collectors. The second part is the entropic heat, which is called "reversible heat source" mainly caused by the entropy change and it can be positive or negative. Positive reversible heat means that the chemical reaction is exothermic and the negative reversible heat means that the chemical reaction is endothermic. Endothermic reaction means that the chemical bonds of the reactants have higher energy than the products' bonds [24]. In this thesis, only the overpotential heat source is considered because the contribution of entropy heat is relatively small compared to overpotential part under high C-rates [18], [19].

3.5 Utilized temperature estimation methods

Generally, in most of practical problems, few of the states of the dynamical system are measurable. Most of the states or measurements are affected by noise. In such cases, a feasible solution can be the estimation of all states or part of them by deigning an observer such as the

Kalman filter. In this section, the fundamentals of Kalman filter and sliding mode observer are briefly described.

3.5.1 Kalman filter

The Kalman filter is one the most significant and common sensor and data fusion algorithms at present [31]. Due to unique advantages of the Kalman filter, which are inexpensive computational cost, well-designed recursive properties, and suitability for real-time applications, they are used in various dynamical systems. One of the main applications of Kalman filter is to estimate the states of system having noisy measurements. The modelling of noise and stochastic dynamical systems are described in detail in [32]. In this section a brief introduction to Kalman filter for discrete systems is discussed, because the cell thermal modelling in this thesis will be done in discrete form.
Consider a discrete time linear system on the form

$$\begin{aligned} x(k+1) &= Ax(k) + Bu(k) + F\,v(k) \\ y(k) &= Cx(k) + w(k) \end{aligned} \tag{3.21}$$

In which $v(k)$ and $w(k)$ are independent white Gaussian noise with zero mean and covariances R_v and R_w, respectively. The initial conditions are defined by $E\{x_0\} = x_0$ and $P_0 = E\{x(0)x^T(0)\}$ as expected value and covariance, respectively. The estimation dynamics can be defined as

$$\hat{x}(k+1) = A\hat{x}(k) + B\hat{u}(k) + L(k)(y(k) - C\hat{x}(k)) \tag{3.22}$$

According to [33], the Kalman filter gain (L) which minimizes the mean square error is given by

$$\begin{aligned} L(k) &= AP(k)C^T(R_w + CP(k)C^T)^{-1} \\ P(k+1) &= (A - LC)P(k)(A - LC)^T + FR_vF^T + R_wL^T \end{aligned} \tag{3.23}$$

When the system is stationary, $P(k) = P(k+1)$, the Kalman filter gain is given by

$$\begin{aligned} L &= APC^T(R_w + CPC^T)^{-1} \\ P &= APA^T + FR_vF^T - APC^T(R_w + CPC^T)^{-1}CPA^T \end{aligned} \tag{3.24}$$

The Kalman filter that is described in Eq. 3.24 works in predictor case. It means that it predicts the states at time step *k* based on measurements at time step *k-1*. The Kalman filter can also works in filter case in which the state variables at time step k can be estimated by measurements at time step *k*. The Kalman filter gain in filter case can be written as

$$\hat{x}(k|k) = \hat{x}(k) + \tilde{L}(k)(y(k) - C\hat{x}(k) - Du(k)) \tag{3.25}$$

where the Kalman filter gain ($\tilde{L}$) and covariance of estimation error $P(k|k)$ are given by

$$\begin{aligned} \tilde{L}(k) &= P(k)C^T(CP(k)C^T + R_w)^{-1} \\ P(k|k) &= P(k) - P(k)C^T(CP(k)C^T + R_w)^{-1}CP(k) \end{aligned} \tag{3.26}$$

The details of the Kalman filter in filter case are presented in [32]. However, for non-linear systems, there are various types of Kalman filters, such as the Extended Kalman Filter (EKF), Unscented Kalman Filter (UKF) and Cubature Kalman Filter (CKF) which can be appropriate

to handle non-linear dynamic problems. These forms of Kalman filters are discussed in detail in [34].

3.5.2 Sliding Mode Observer (SMO)

Consider a typical linear continuous system

$$\dot{x} = Ax(t) + Bu(t) \qquad (3.27)$$
$$y = Cx(t)$$

In which $A \in R^{n\times n}$, $B \in R^{n\times m}$ and $C \in R^{p\times n}$. In addition, A and C matrices are full rank, and the system is fully observable. To design a sliding mode observer, the coordinate transformation $z = T_c x$ can be done in which

$$T_c = \begin{bmatrix} N_c^T \\ C \end{bmatrix} \qquad N_c \text{ is null space of } C$$

By this transformation, the state space matrix has the following form

$$T_c A {T_c}^{-1} = \begin{bmatrix} A_{11} & A_{12} \\ A_{21} & A_{22} \end{bmatrix} \qquad T_c B = \begin{bmatrix} B_1 \\ B_2 \end{bmatrix} \qquad C{T_c}^{-1} = [0\ I_p]$$

in which $A_{11} \in R^{(n-p)\times(n-p)}$ and $B_1 \in R^{(n-p)\times m}$. This form of C matrix is essential to design sliding mode observer. The formulation of state observation for $(\hat{x}, \hat{y})$ can be written as Eq. 3.28 in which the v is a discontinuous injection term.

$$\dot{\hat{x}}(t) = A\hat{x}(t) + Bu(t) + G_n v \qquad (3.28)$$
$$\hat{y} = C\hat{x}(t)$$

where $G_n = \begin{bmatrix} L \\ -I_p \end{bmatrix}$ $\qquad L: (n-p)\times p$

By definition of $e(t) = \hat{x}(t) - x(t)$ and $e_y(t) = \hat{y}(t) - y(t)$ and $v = \rho sign(e_{y,i})$ $i = 1, \dots p$ in which ρ is a positive scalar and $e_{y,i}$ shows the error of measurable state. In fact, the term v is a discontinuous function that force the trajectories of $e(t)$ on $S = \{e: Ce = 0\}$ in finite time. The error dynamics can be written as

$$\dot{e} = Ae(t) + G_n v \qquad (3.29)$$

By separation of measurable and unmeasurable states, the error dynamics equation can be re-written as follows:

$$\dot{e}_1 = A_{11}e_1 + A_{12}e_y + Lv \qquad e_1: (n-p)\times 1 \qquad (3.30)$$
$$\dot{e}_y = A_{21}e_1 + A_{22}e_y - v$$

Thus, the error of measurable states can be written as

$$\dot{e}_{y,i} = A_{21,i}e_1 + A_{22,i}e_y - \rho\ sign(e_{y,i}) \qquad (3.31)$$

By defining the Lyapunov function as $V = \frac{1}{2}{e_{y,i}}^2$, the reachability condition to the surface S is $\dot{V} < 0$.

Having $sign(e_{y,i})e_{y,i} = |e_{y,i}|$

$$e_{y,i} \times \dot{e}_{y,i} = e_{y,i}(A_{21,i}e_1 + A_{22,i}e_y) - \rho\,|e_{y,i}| < -|e_{y,i}|(\rho - |A_{21,i}e_1 + A_{22,i}e_y|)$$

The reachability condition is that ρ should be chosen large enough to make Eq. 3.32 holds, i.e.,

$$\rho > \left|A_{21,i}e_1 + A_{22,i}e_y\right| + \gamma \quad (3.32)$$

where γ should be positive. Once the reachability condition $e_{y,i} \times \dot{e}_{y,i} < -\gamma\left|e_{y,i}\right|$ satisfied, it guarantees the convergence of $e_{y,i}$ to zero in finite time and consequently, the sliding motion take place on surface S.

Using $e_y = \dot{e}_y = 0$ when sliding on the surface S, the following state space system can be derived:

$$\begin{aligned} \dot{e}_1 &= A_{11}e_1 + Lv_{eq} \\ 0 &= A_{21}e_1 - v_{eq} \end{aligned} \quad (3.33)$$

So, the sliding surface can be found as $\dot{e}_1 = (A_{11} + LA_{21})e_1$ in which L should be determined such that all eigenvalues of $A_{11} + LA_{21}$ should be on the left half plane. This implies that e_1 converges to zero and the estimated states are closed to real states.

In addition, there is another definition of sliding mode observer in which a linear output error feedback term will be added to the observer expression. Hence, the modified form of sliding mode observer can be written as:

$$\dot{\hat{x}}(t) = A\hat{x}(t) - G_l e_y + Bu(t) + G_n v \quad (3.34)$$
$$G_l: n \times p$$

In a similar way, the error dynamics can be found to be

$$\dot{e}(t) = (A - G_l C)e(t) + G_n v \quad (3.35)$$

Consider the Lyapunov function $V = e^T Pe$ in which P $(n \times n)$ is symmetric positive definite matrix. In order to assess the reachability criteria which is, $\dot{V} < 0$, differentiating the Lyapunov function gives

$$\dot{V} = \dot{e}^T Pe + e^T P\dot{e} = e^T(P(A - G_l C) + (\dot{A} - G_l C)^T P)\mathrm{e} + 2e^T P G_n v \quad (3.36)$$

In order to satisfy the reachability condition, based on the formulation in [20], $G_n = -\beta\, P^{-1}C^T$ and $P(A - G_l C) + (A - G_l C)^T P < 0$, then the estimation error will converge to zero, i.e., the obtained estimated states represent the real states.

Chapter 4: Modelling in MATLAB/Simulink

4.1 The Equivalent Electrical Model (EEM)

As mentioned earlier, there are various methods and models for cell electrical modelling, such as Rint model, first-order and second-order RC models and so on. Among the mentioned models, the second-order ECM (Electrical Circuit Model) is the most common electrical network for battery simulations due to its accuracy and simplicity. In fact, it handles the concentration polarization as well as electro-chemical polarization inside the cell with two RC pairs. Thus, in this thesis, the second-order ECM, which is shown in Figure 4.1, was implemented to provide the necessary input parameters, such as resistances, to determine the heat generation that is required for the thermal modeling and consequently temperature estimation. The "Cell Characteristics" block takes primary parameters, such as cell capacity, initial SOC, current and temperature as input, and computes the Ohmic resistance (R_0), electrochemical polarization resistance (R_1) and capacitance (C_1), concentration polarization resistance (R_2), and capacitance (C_2) and open circuit voltage.

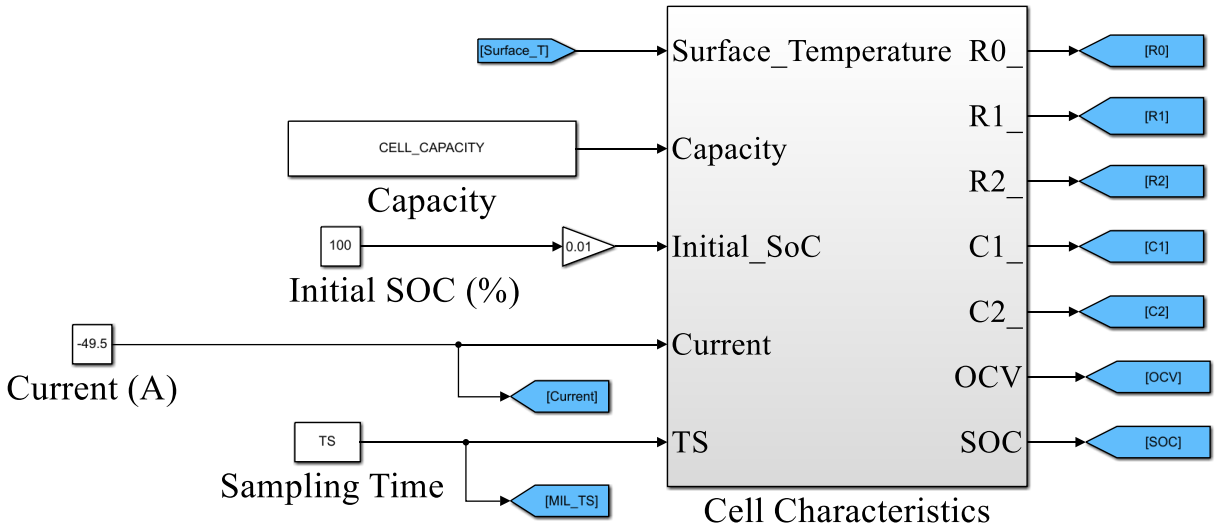

Figure 4.1: The electrical model of a battery cell in MATLAB/Simulink

The "Cell Characteristics" block calculates SOC by the Coulomb counting, i.e.,

$$SOC(t) = SOC(t_0) - \frac{1}{3600C}\int_{t_0}^{t} I(t)dt \qquad (4.1)$$

where, $SOC(t_0)$ is the initial SOC, C (Ah) is the initial capacity of the cell and is a function of temperature and current rate, and $I(t)$ is the current. Then, open circuit voltage, R_0, R_1, R_2, $C_1$and C_2 values corresponding to the initial SOC, current profile and temperature will be calculated.

4.2 Heat generation inside the cell

As mentioned earlier, internal heat generation rate in cell can be simplified to Eq. 4.3. Furthermore, having the electrochemical and concentration resistances, heat generation rate can be obtained as

$$Q = \mathrm{I}(V_{\mathrm{OCV}} - V_T) + \mathrm{IT}\frac{\mathrm{d}V_{\mathrm{OCV}}}{\mathrm{dT}} \qquad (4.3)$$

$$Q = (R_0 + R_1 + R_2)I^2 + \mathrm{IT}\frac{\mathrm{d}V_{\mathrm{OCV}}}{\mathrm{dT}} \qquad (4.4)$$

The first part of Eqs. 4.3 and 4.4 represent the overpotential heat (irreversible heat), which is heat generated by the polarization of the electrodes. The second part is the entropic heat (reversible heat), which is mainly caused by the entropy change. The reversible heat contribution is negligible in high C- rates [18], [19], so only the overpotential heat generation, as shown in Figure 4.2, is considered as internal heat source in this thesis.

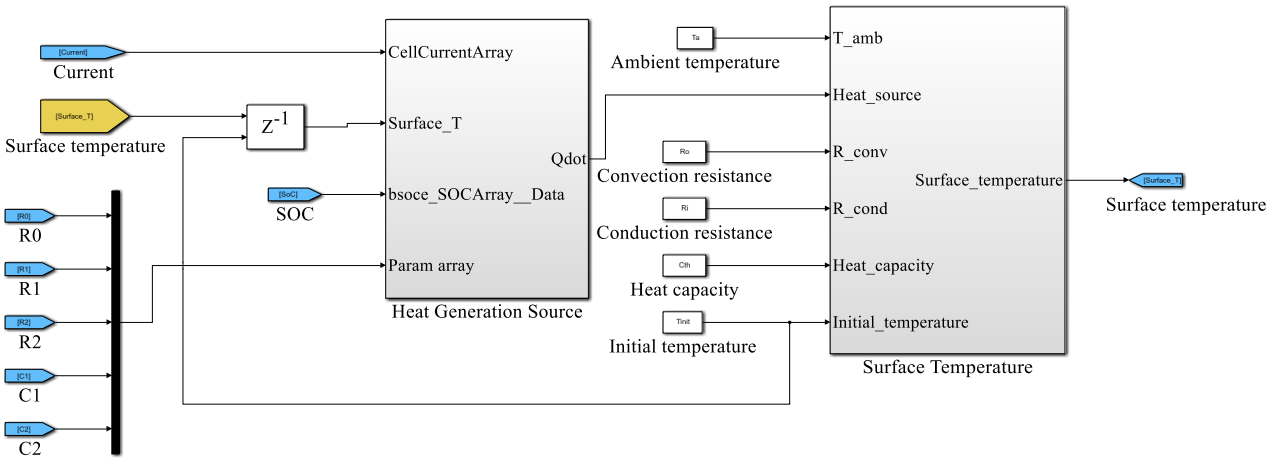

Figure 4.2: The heat generation model in MATLAB/Simulink

4.3 Thermal modelling

As described earlier, the lumped method relates the thermal energy rate inside the cell (or temperature variation) to the rate of heat generation inside the cell minus the heat release. On the other hand, the heat transfer of battery can be interpreted as an electrical network, including resistances and capacitors in which temperature represents the voltage, q (heat transfer rate) represents the current and heat capacity can be demonstrated as a capacitor to maintain the thermal energy inside it. In addition, it is obvious that the heat transfer take place as conduction, from core to the surface, and the convection from surface to ambient. There are two lumped model (second-order model and first-order model) which are commonly used in the literatures. Although the lumped model is not able to represent real interaction neither inside nor outside of the cell, it is still a popular method due to efficiency and suitability for real-time applications.

4.3.1 Lumped model- Second-order model

This approach models the cell heat transfer using a RC-network in which the resistances and capacitors characterize the heat transfer and the capability of the cell to maintain thermal energy. It can be seen in Figure 4.3 that the heat transfer from cell core to ambient is modelled by two types of resistances which are conduction resistance inside the cell and convection resistance outside the cell. Furthermore, the model contains two capacitors that represent the capacity of material inside and outside the cell to maintain thermal energy. The cell configuration can be in various shapes, such as cylindrical, prismatic and pouch. It should be noted that the prismatic cell with aluminum housing is considered in this thesis. To simplify the model, the following assumptions are made:

- The heat transfer of cell follows this route: cell core→ cell surface → ambient.
- There is no radiation heat transfer because the radiation is significant only at high temperatures.
- Thermal parameters do not change with temperature.
- There is no convection heat transfer inside the cell.
- The temperature distribution on cell housing surface is uniform because cell housing made up of aluminum, which has very high thermal conductivity.

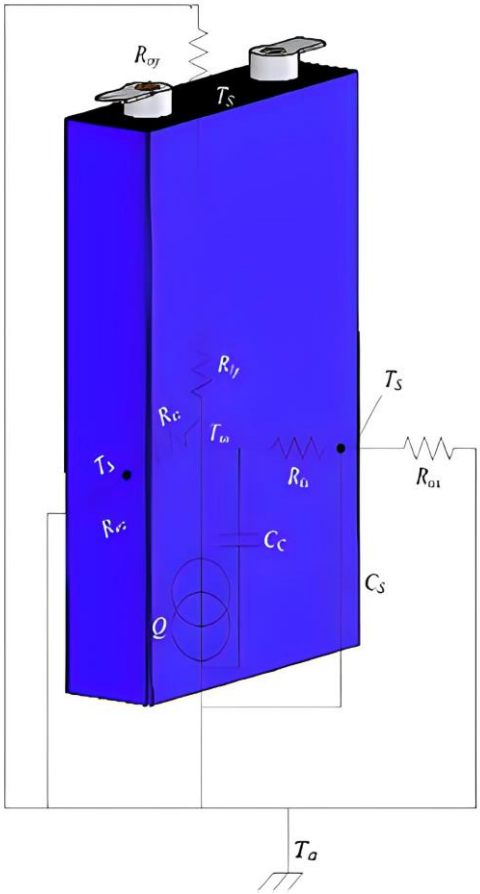

Figure 4.3: Equivalent electrical circuit analogy of thermal model of a cell [6]

The equivalent thermal circuit of cell can be obtained as shown in Figure 4.4, in which C_c $(j/°\mathrm{C})$ represents the heat capacity of internal material inside the cell and C_s $(j/°\mathrm{C})$ heat capacity of cell housing. Furthermore, T_i (core temperature), T_s (surface temperature), and T_a (ambient temperature), are shown by voltage in equivalent thermal model to display the potential heat transfer between the resistances. Q represents the internal heat generation rate that can be obtained from Eq. 4.4. The conduction and convection resistances are R_i and R_o in X, Y and Z-direction, respectively.

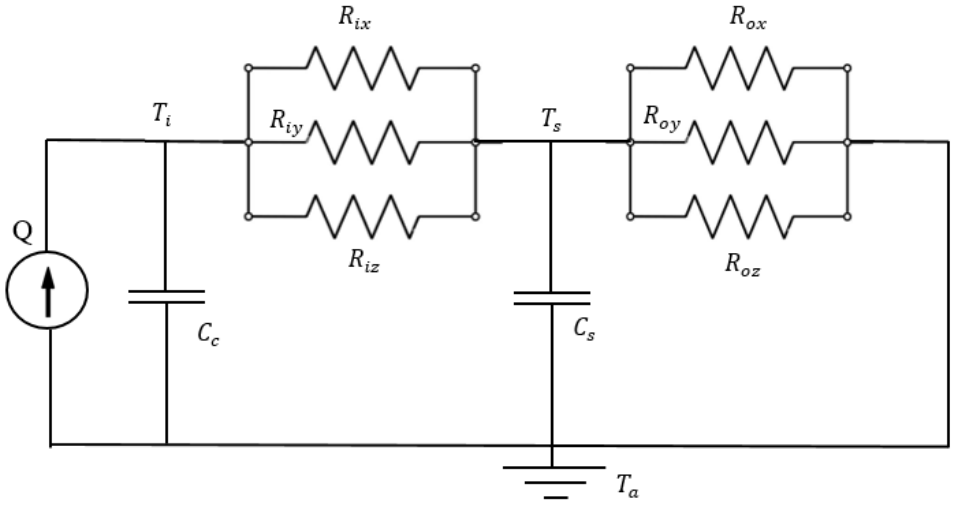

Figure 4.4: The second-order equivalent thermal circuit of cell

In addition, it can be seen that the R_i and R_o in X, Y and Z-direction are parallel, so the circuit in Figure 4.4 can be simplified as Figure 4.5 where the equivalent conduction resistance can be derived as from

$$\frac{1}{R_i} = \frac{1}{R_{ix}} + \frac{1}{R_{iy}} + \frac{1}{R_{iz}} \qquad (4.5)$$

Similarly, the convection resistance can be modelled by R_o in all directions as follows:

$$\frac{1}{R_o} = \frac{1}{R_{ox}} + \frac{1}{R_{oy}} + \frac{1}{R_{oz}} \qquad (4.6)$$

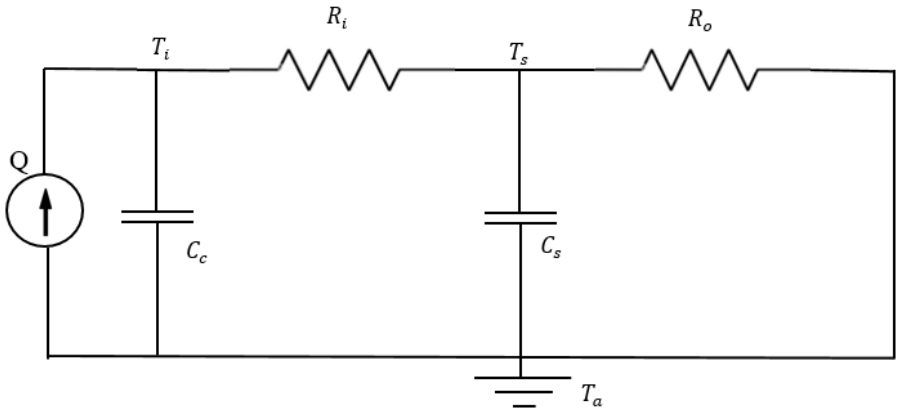

Figure 4.5: The second-order equivalent thermal circuit of cell (simplified form)

Based on the lumped model formulation, the thermal energy rate is equal to the net heat transfer $q_{in} - q_{out}$ plus heat generation rate Q (W) inside the cell which is given by Eq. 4.4. Therefore, the rate of change in thermal energy can be written as

$$\sum(q_{in} - q_{out}) + Q = mc\frac{dT}{dt} \tag{4.7}$$

in which c $(j/kg.℃)$ is specific heat capacity and m is mass (kg). The lumped model formulation for the whole cell including material inside cell (anode, cathode, separator, collectors and so on) and cell housing (aluminum shell that covers the cell) can be written in general form as

$$m_c c_c \frac{dT_i}{dt} = Q - q_{cond} \tag{4.8}$$
$$m_s c_s \frac{dT_s}{dt} = q_{cond} - q_{conv} \tag{4.9}$$

where m_c and m_s are the masses of material inside the cell and shell housing, respectively. Furthermore, c_c and c_s are the specific heat capacity of cell material and shell. The conduction and convection can be defined as

$$q_{cond} = \frac{T_i - T_s}{R_i} \tag{4.10}$$
$$q_{conv} = \frac{T_s - T_a}{R_o} \tag{4.11}$$

R_i and R_o represent the resistance against the conduction and convection heat transfer, respectively. Therefore, the formulation of a second-order lumped model can be written as:

$$C_c \frac{dT_i}{dt} = Q - \frac{T_i - T_s}{R_i} \tag{4.12}$$

$$C_s \frac{dT_s}{dt} = \frac{T_i - T_s}{R_i} - \frac{T_s - T_a}{R_o} \tag{4.13}$$

In which the heat capacities can be defined as $C_c = m_c c_c$ $(j/℃)$ and $C_s = m_s c_s$ $(j/℃)$. By introducing $x_1 = T_i$ and $x_2 = T_s$ as state variables, the state space model in continuous form is as follows:

$$\begin{bmatrix}\dot{x}_1(t)\\ \dot{x}_2(t)\end{bmatrix} = \begin{bmatrix}-\frac{1}{R_i C_c} & \frac{1}{R_i C_c}\\ \frac{1}{R_i C_s} & -\frac{1}{R_i C_s} - \frac{1}{R_o C_s}\end{bmatrix}\begin{bmatrix}x_1(t)\\ x_2(t)\end{bmatrix} + \begin{bmatrix}0 & \frac{1}{C_c}\\ \frac{1}{R_o C_s} & 0\end{bmatrix}\begin{bmatrix}T_a\\ Q\end{bmatrix} \tag{4.14}$$

$$y(t) = \begin{bmatrix}0 & 1\end{bmatrix}\begin{bmatrix}x_1(t)\\ x_2(t)\end{bmatrix} \quad C = \begin{bmatrix}0 & 1\end{bmatrix} \tag{4.15}$$

where the matrix C is defined such that T_s is measurable and T_i is unmeasurable. Regarding that it is intended to perform estimation in discrete form, by discretizing the state space using $\dot{x}_1 = \frac{x_1(k+1) - x_1(k)}{\Delta t}$ and $\dot{x}_2 = \frac{x_2(k+1) - x_2(k)}{\Delta t}$, in which Δt is the sampling time, a corresponding discretized state space model is

$$\begin{bmatrix} x_1(k+1) \\ x_2(k+1) \end{bmatrix} = \begin{bmatrix} 1 - \frac{\Delta t}{R_i C_c} & \frac{\Delta t}{R_i C_c} \\ \frac{\Delta t}{R_i C_s} & 1 - \frac{\Delta t}{R_i C_c} - \frac{\Delta t}{R_o C_s} \end{bmatrix} \begin{bmatrix} x_1 \\ x_2 \end{bmatrix} + \begin{bmatrix} 0 & \frac{\Delta t}{C_c} \\ \frac{\Delta t}{R_o C_s} & 0 \end{bmatrix} \begin{bmatrix} T_a \\ Q \end{bmatrix} \quad (4.16)$$

$$y(k) = [0 \quad 1] \begin{bmatrix} x_1(k) \\ x_2(k) \end{bmatrix} \quad (4.17)$$

This state-space model is used for the Kalman filter estimations and its continuous form is used for the sliding mode observer, which will be discussed in the following sections.

4.3.2 Lumped model- first-order model

The first-order model is the simplified form of second-order model in which the capacity of the cell is modelled by one capacitor. Figure 4.6 shows the first-order model in which C_{th} stands for thermal capacity of cell (J/℃), Q represents the heat generation rate in the cell (W), R_i represents the internal conduction resistance, R_o is the external convection resistance, T_i is the internal temperature (core temperature), T_s is the surface temperature and T_a is the ambient temperature.

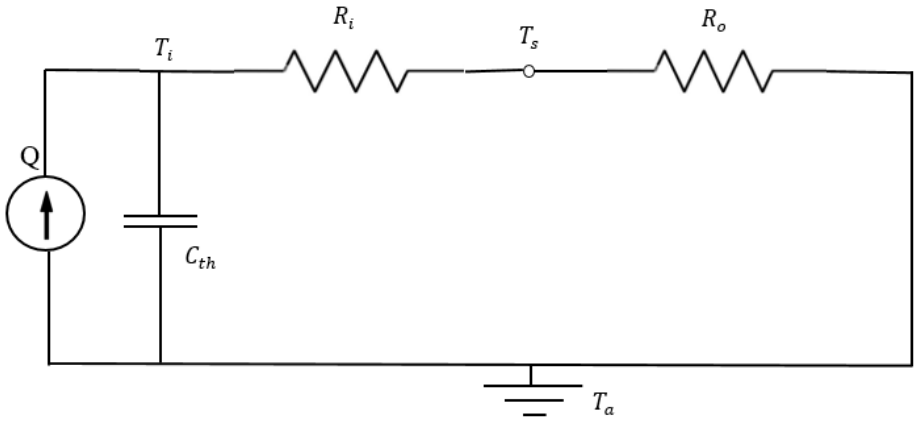

Figure 4.6: First-order equivalent thermal model

With regard to the capacitor formulation, the differential equation of first-order model can be written as:

$$C_{th} \frac{dT_i}{dt} = Q - q \quad (4.18)$$

As the sum of currents flowing into that node is equal to the sum of currents flowing out of that node, we have

$$q = \frac{T_i - T_s}{R_i} = \frac{T_s - T_a}{R_o} \quad (4.19)$$

Then, temperature inside the cell can be derived as a function of T_s as:

$$T_i = \frac{R_i + R_o}{R_o} T_s - \frac{R_i}{R_o} T_a \quad (4.20)$$

Consequently, by insertion of T_i in Eq. 4.18, the differential equation for T_s can be obtained as follows:

$$\frac{dT_s}{dt} = \frac{R_o Q}{C_{th}(R_i+R_o)} - \frac{T_s - T_a}{C_{th}(R_i+R_o)} \tag{4.21}$$

The discrete form of Eq. (4.21) can be found be as follows:

$$T_s(k+1) = T_s(k)e^{\frac{\Delta t}{C_{th}(R_i+R_o)}} + (T_a(k) + R_o \times Q) \times (1 - e^{\frac{\Delta t}{C_{th}(R_i+R_o)}}) \tag{4.22}$$

This expression is used to estimate T_i using Kalman filter estimation with a first-order model that will be described following sections. The Simulink model of first-order model is shown in Figure 4.7.

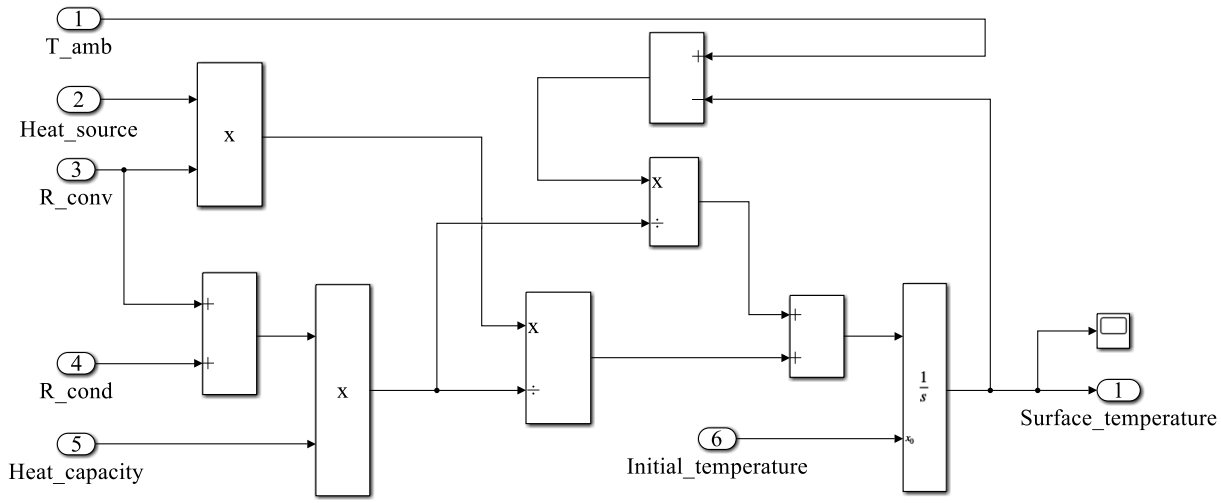

Figure 4.7: The first-order lumped model for surface temperature

4.3.3 Finite Difference Model (FDM)

The finite difference method derives a couple of discrete equations that relates the temperature of each node at a specified time step to the temperature of that node itself at previous time step together with surrounding nodes. These set of equations can be transformed into the discrete state-space model in which each node corresponds to one specific state. Hence, the state-space matrix includes all the nodes in model. For example, by meshing the model with *m* nodes in X-direction and *n* nodes in Y-direction, we have $m \times n$ state-space variables. In other words, FDM converts the heat differential equation for central nodes, corner nodes and edge nodes to discretized equations which are given by Eqs. 3.16 and 3.17.

4.4 Temperature estimation using Electro-Thermal Model (ETM)

Regarding the state space model, the model inputs are ambient temperature (T_a) and internal heat generation rate (Q), which is given by "heat generation block". Thus, to estimate the temperature inside the cell, it is necessary to connect battery electrical model with thermal

model that can be called Electro-Thermal Model (ETM). As can be seen in Figure 4.8, the current and ambient temperature are inputs to the electrical model which determine the SOC, V_{OCV} and V_T that are needed for the heat generation block. Then, the heat generation block calculates the heat generation rate inside the cell according to Bernardi's formulation and feedforward it to the thermal model block can be either lumped model or finite difference model. Consequently, the thermal model converts the heat transfer relations inside and outside the cell to a state-space model and estimate the temperature inside the cell using a Kalman filter or a sliding mode observer.

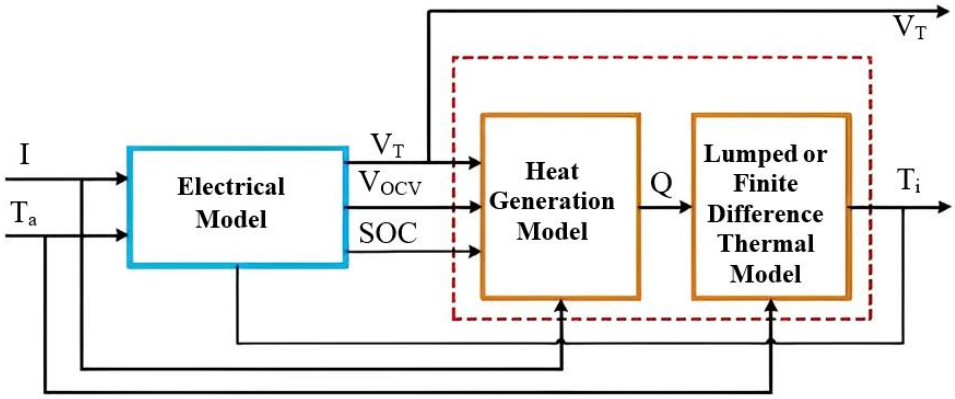

Figure 4.8: The schematic diagram of Electro-Thermal Model (ETM)

The modeling methods and estimation approaches that are used in this thesis are presented in Table. 4.1.

Table 4.1: The thermal modeling and estimation methods for temperature estimation

Model No.	Thermal model	State space	Estimation method
1	Lumped	Continuous	Conventional Sliding mode observer
2		Continuous	Modified sliding mode observer
3		Discrete	Kalman filter
4	FDM	Discrete	Kalman filter

4.4.1 Temperature estimation based on lumped model

The lumped model simplifies the conduction and convection heat transfer into an electrical circuit. Although this method cannot model the complexity of heat transfer around cell, it has been used extensively for temperature estimation due to ease of use and suitability for onboard applications. In this thesis, the lumped model integrated with Kalman filter and sliding mode observer to estimate the temperature inside the cell. Figure 4.9 shows Kalman filter, that is implemented in two versions, which are first and second-order model, using the discrete state-space model and the inputs to system, which are ambient temperature and heat generation rate. The first case, as shown in Figure 4.9, the measurements for Kalman filter block generated by T_s from the first-order model that is mixed by white Gaussian noise. In the second case study, the Kalman filter block takes the measurements directly from the output of second-order state-space model. It should be mentioned that the noise term is added to the measured signal inside the Kalman filter block.

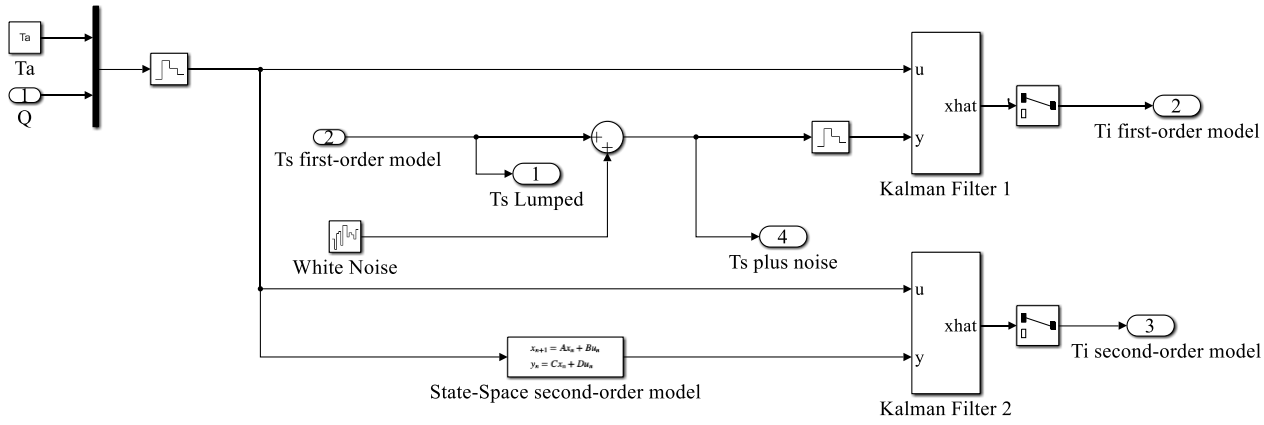

Figure 4.9: Kalman filter estimation block in Simulink

In addition, two types of sliding mode observer are implemented for temperature estimation, based on the continuous state space model. The first one is the classical Utkin observer and the second one is the modified version that has better estimation properties by taking into account the output error feedback term. The sliding mode observers and their connections to other blocks are shown in Figure 4.10.

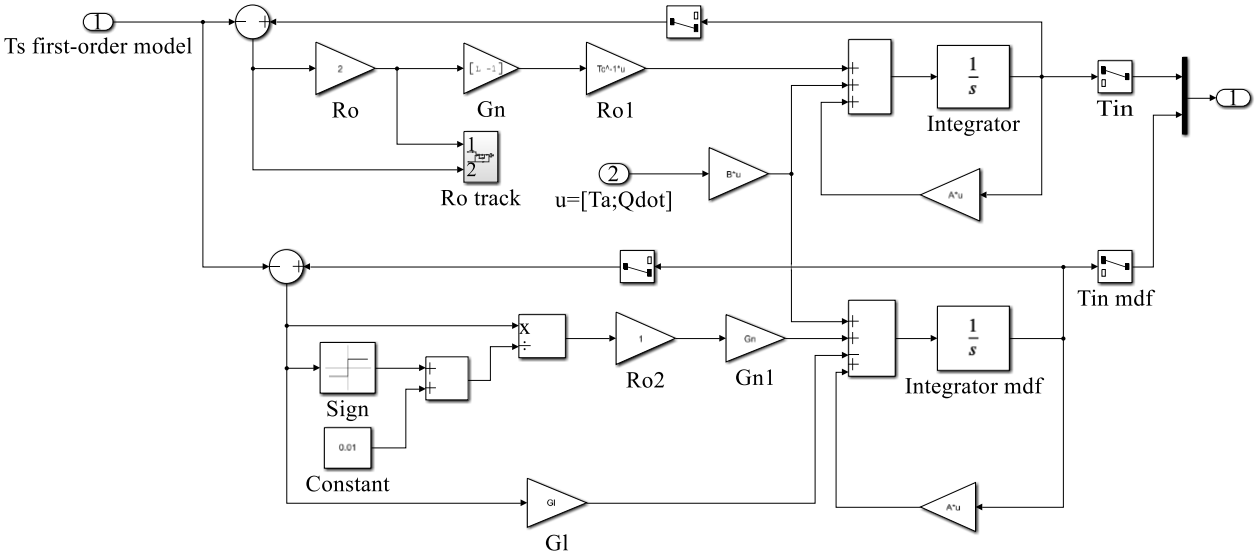

Figure 4.10: The sliding mode observers in Simulink

4.4.2 The temperature estimation using FDM

As mentioned in Section 4.3.3, FDM derives the state-space model in discreet form by discretizing the heat differential equation in X- and Y-direction and in time as well. As can be seen in Figure 4.11, the derivation of state space model for all nodes (corner nodes, edge node and internal nodes) are done in the “State Space” block. In addition, this block provides state space model to Kalman filter block that estimate the temperature inside the cell by taking into account the T_s generated by the finite difference model added with white noise.

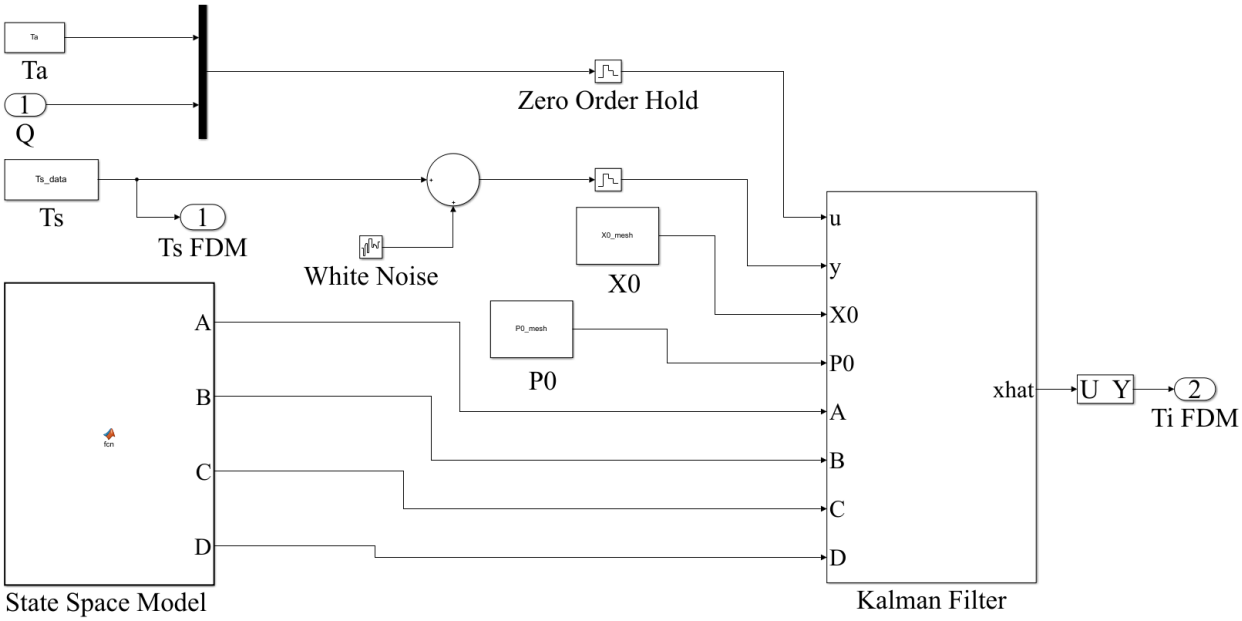

Figure 4.11: The temperature estimation block based on FDM

It is important to mention that the necessary condition to design a sliding mode observer for a specified system is that the system must be observable. Regarding this limitation, the state space model derived from the finite difference method is unobservable. Thus, the sliding mode observer has not been implemented for the FDM thermal model.

4.5 Finite Difference (FD) modelling

One of the alternative ways to evaluate the temperature distribution inside the cell without using an observer is to solve the heat differential equation using FD method by considering the boundary condition and the internal heat source. To do so, at first, the electrical model gives the heat generation rate inside the cell, which is then sent to a MATLAB code that discretize the heat differential equation for all nodes on the X-Y plane of cell, as depicted on Figure 4. 12. Then, it solves the discretized equations from the initial condition and convection boundary conditions.

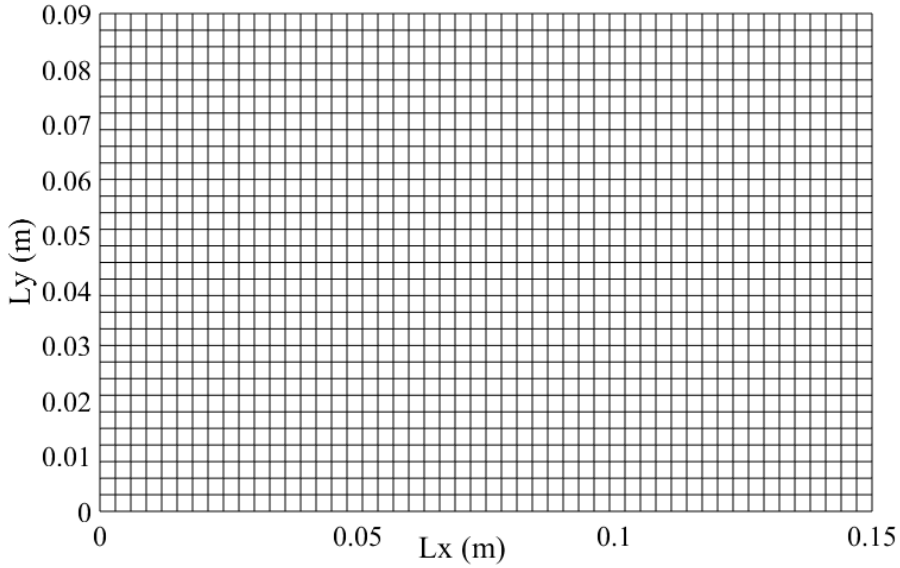

Figure 4.12: Finite difference model (mesh size=3 mm)

4.6 Finite Element Modelling (FEM)

The PDE toolbox in MATLAB is able to solve structural mechanics, heat transfer, and general Partial Differential Equations (PDEs) by pre-defined functions using finite element analysis for 2D and 3D geometries. It must also be noted that FE-method divides a large geometry into smaller and simpler components called elements, such as triangular (for 2D geometry) and tetrahedral (for 3D geometry). Then, it formulates the whole system or geometry by determining the equations for each element and assemble them to make a set of equations that can be solved by applying the initial conditions, boundary conditions and loads. The details of FEM can be found in Ref. [35] ,[36].
In order to solve the heat transfer equation using PDE toolbox, the primary information (as shown in Table. 4.2) such as analysis type, geometry, thermal properties, initial and boundary condition, geometry, element size and so on should be defined for the mesh model in Figure 4.13. The detailed description of the PDE toolbox functions in Table 4.2 is presented in [37].

Table 4.2: PDE toolbox functions for transient thermal analysis

Inputs	PDE function
analysis type	createpde(thermal,transient)
geometry	g = decsg (3,4, X-coordinates, Y-coordinates)
thermal property	thermalProperties (model, conductivity,k_{cond},mass density, ρ,specific heat, c)
heat source	internalHeatSource(model, Q)
initial condition	thermalIC(model,T_a)
boundary condition	thermalBC (model, region type, region ID, convection coefficient, k_{conv},ambient temperature, T_a)
element size	generateMesh(model,hmax,2)

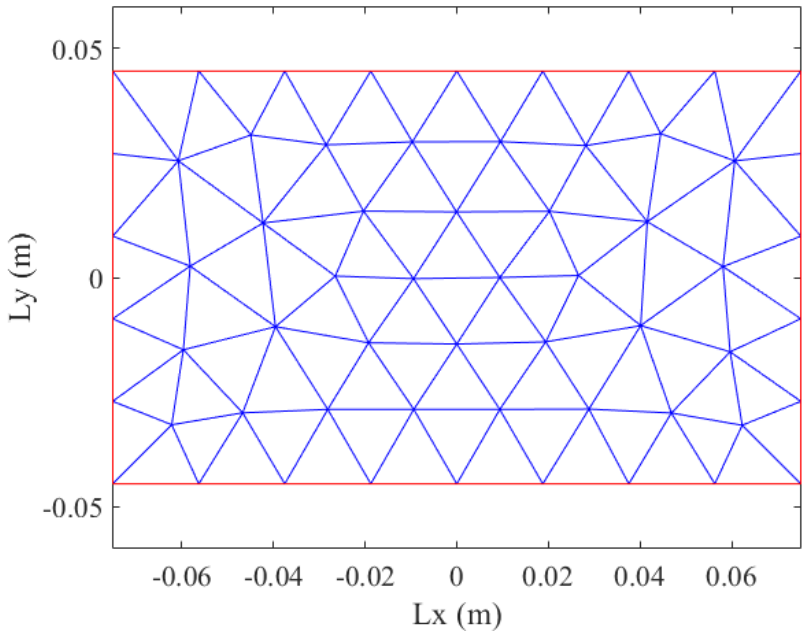

Figure 4.13: The FE model of cell with triangular elements (mesh size=2 cm)

4.7 CFD modelling

It can be seen in Figure 4.14 that the full cell consists of housing, jelly roll (stack), current collector, electrolyte, and other subsidiary components. In addition, as depicted on Figure 4.15, the jelly roll is made up of several layers of anode, cathode, and separators. It should be mentioned that there is an air gap between housing and jelly roll such that convection heat transfer can occur there and consequently, it makes the heat transfer problem more challenging. This imply that the lumped model and finite difference models that are implemented in this work may be too simplified to represent the real and practical conditions. Hence, it is helpful to evaluate the accuracy of estimations obtained from lumped model and finite difference model with CFD results.

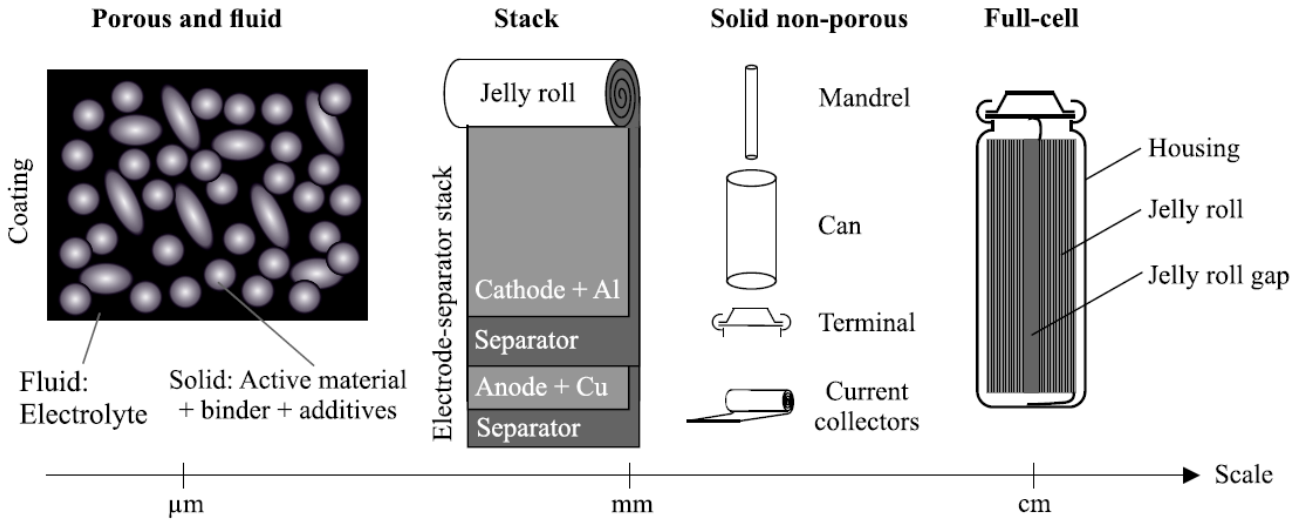

Figure 4.14: The material inside a cylindrical cell at different scales [38]

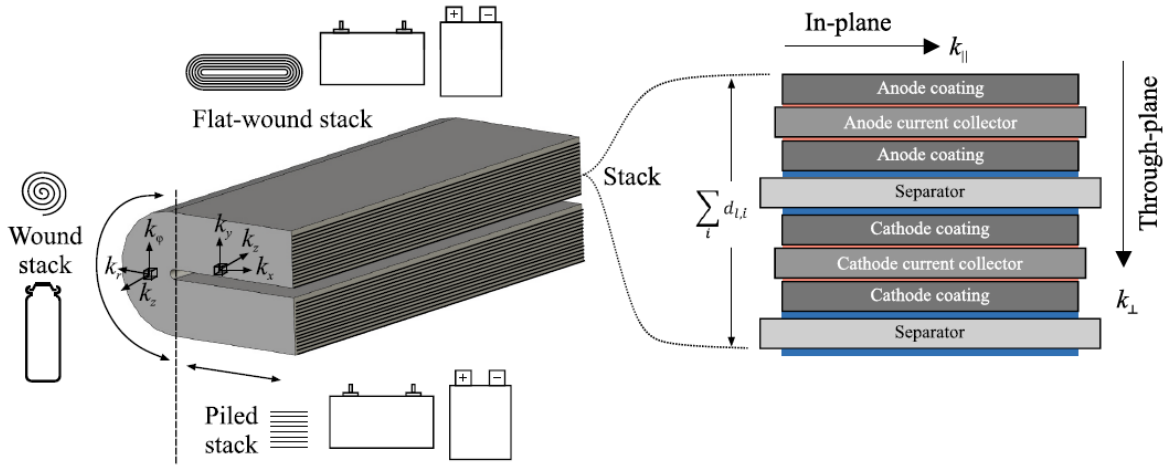

Figure 4.15: The piled stack of electrode-separator for a prismatic cell [6]

Figure 4.16 shows the CFD model of cell in which the jelly roll, current collector, housing, and surrounding air around the cell are modelled in a typical CFD software. The top surface of the cell is isolated by a plastic layer, and the other surfaces have convection with surrounding air. Some CFD results are used as a validation reference for core temperature and surface temperature predictions of the proposed solutions, as they are performed using validated parameters on a candidate cell.

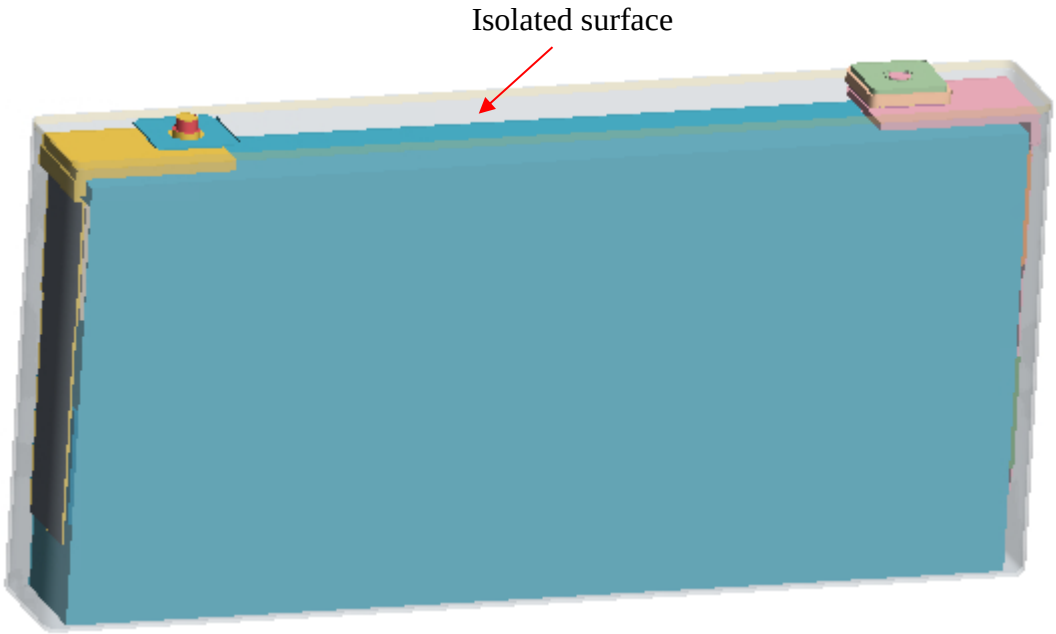

Figure 4.16: The CFD model of a specified cell

Chapter 5: Simulations and results

This chapter discusses the results of the mentioned modelling approaches (lumped model and FDM) and estimation methods (Kalman filter and sliding mode observer) in various load-cases. Moreover, the derivation of model parameters such as thermal conductivity, convection coefficient for lumped model and FDM will be described as well.

5.1 Equivalent 2D model for FDM

In order to perform simulations with the lumped model, it is necessary to have heat capacities of the cell (C_c) and shell housing (C_s), conduction resistance (R_i) and convection resistance (R_o). The exact values for these parameters were not available. Therefore, the values in Table. 5.1 are used, which is from cell specification in papers that are relatively closed to the simulated cell in terms of mass, C-rate, anode/cathode material and dimensions. C_{th} is the heat capacity of whole lumped model including cell and shell for first-order lumped model.

Table 5.1: The cell specification for lumped model

parameter	R_i (℃/W)	R_o (℃/W)	C_c (j/℃)	C_s (j/℃)	C_{th} (j/℃)
value	0.42	0.86	775	15	790

The schematic image of the cell for this thesis is shown in Figure 5.1. The surface temperature that is used for estimation is between positive and negative poles. The mentioned T_i that is intended to be estimated by Kalman filter or sliding mode in either lumped model or finite difference model located on the X-Y plane of the cell, as shown in Figure 5.1.
As mentioned earlier, the two-dimensional FD method is used in this thesis, therefore the 3D lumped model that is shown in Figure 5.2, should be converted to a corresponding 2D model. Hence, the thermal conductivity and convection heat transfer for 2D model should be determined such that it represents the given values of R_i and R_o in Table 5.1. According to literatures [38],[39],[40],[41], the thermal conductivity of the cell in Z-direction is a small, compared to other directions. Thus, the conduction resistance in the Z-direction, which can be defined as $R = (L_z/2)/(K_z \times A_{xy})$ will be a large number. Since there is a large resistance in Z-direction for conduction, it is assumed that that there is no heat transfer in the Z-direction or the temperature variation in the Z-direction is zero. As a result, the equivalent thermal conductivity and convection heat transfer correspond to the given values of R_i and R_o for a X-Y plane inside the cell (Z=0) can be derived as follows:

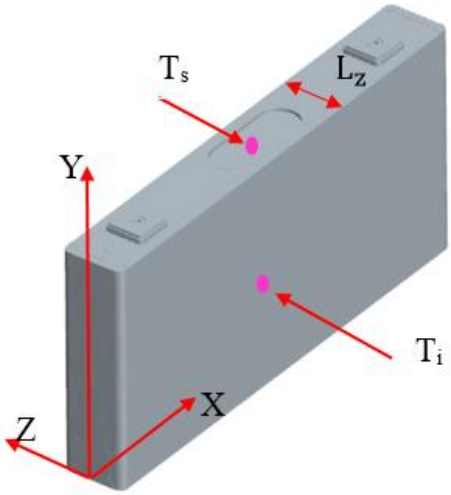

Figure 5.1: The specification of a candidate cell

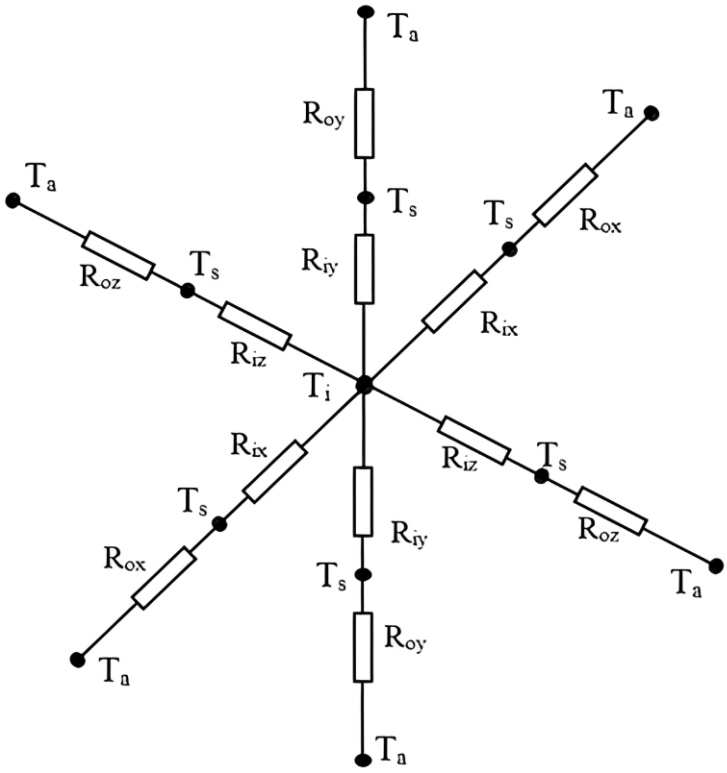

Figure 5.2: The schematic 3D lumped thermal model

$$\frac{1}{R_i} = \frac{2}{R_{ix}} + \frac{2}{R_{iy}} \qquad (5.1)$$

$$R_{ix} = \frac{L_x}{2 \times K_{eq} \times A_{yz}} \qquad (5.2)$$

$$R_{iy} = \frac{L_y}{2 \times K_{eq} \times A_{xz}} \qquad (5.3)$$

By applying the values of R_x and R_y in Eq. 5.1, the equivalent thermal conductivity for the X-Y plane inside the cell for FD simulations will be given by

$$K_{eq} = \frac{1}{R_i \times A_{eq}}, \qquad A_{eq} = \frac{4 \times A_{yz}}{L_x} + \frac{4 \times A_{xz}}{L_x} \qquad (5.4)$$

In addition, Eq. 5.5 gives the equivalent convection coefficient for two dimensional FD simulations by assuming zero convection in X-Y plane from both side of cell ($Z = \pm L_z/2$).

$$h_{eq} = \frac{1}{R_o \times A_s}, \qquad A_s = 2 \times (A_{yz} + A_{xz}) \qquad (5.5)$$

It is notable that the material inside the cell is a combination of jelly stack (anode, cathode, separator), current collector and electrolyte that have different thermal conductivity in X, Y and Z direction. In addition, there is air gap between the stack and the housing that makes the determination of the thermal conductivity more difficult. Thus, the assumption about thermal conductivity in Z direction and equivalent thermal conductivity might be simple too much.

Regarding that the 3D model is converted to 2D model for FD simulations, it is essential to find out where the maximum temperature will take place. To do so, as shown in Figure 5.3, one-fourth of a cell was analyzed with MATLAB PDE toolbox. The F1, F5 and F6 are isolated due to symmetry of the cell and other faces have convection boundary conditions.

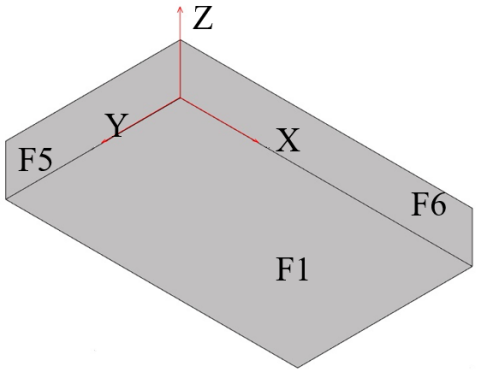

Figure 5.3: The isolated faces for PDE solution

Figure 5.4 shows the temperature distribution in 3D model. It can be seen that the maximum temperature point occurs in the origin of the XYZ-coordinates. So, the X-Y plane is chosen for 2D FDM and FEM simulations in this thesis.

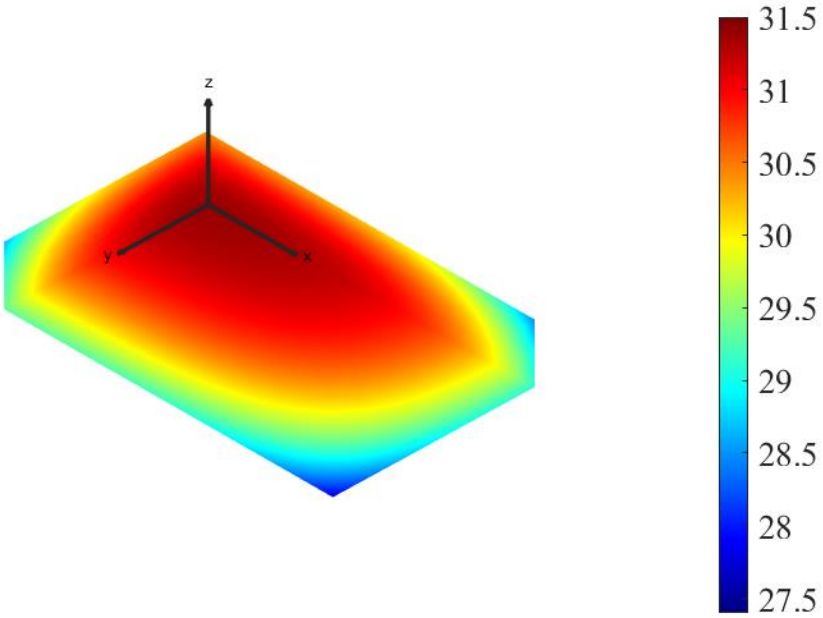

Figure 5.4: The temperature distribution in the 3D model

5.2 Temperature estimation

In this section the results of the different methods for estimation and thermal modeling approaches will be presented. The performance of estimation is evaluated at 1C charge/discharge and 2C charge/discharge rates. At first, as shown in Figure 5.5 and Figure 5.6, the heat generation for 1C charge/discharge is given by the Equivalent Electrical Model (EEM). It can be seen that there is a high variation in heat generation in the beginning and at the end of the charge and discharge processes due to SOC. On the other hand, the heat generation does not change too much in the middle of the process especially in the time interval 600-3000 (s).

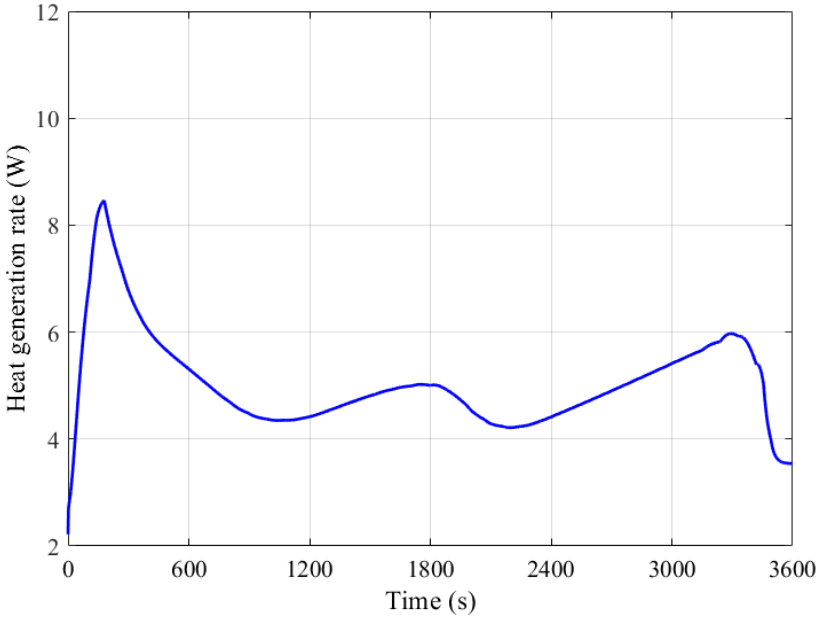

Figure 5.5: Heat generation rate inside the cell during 1C charge

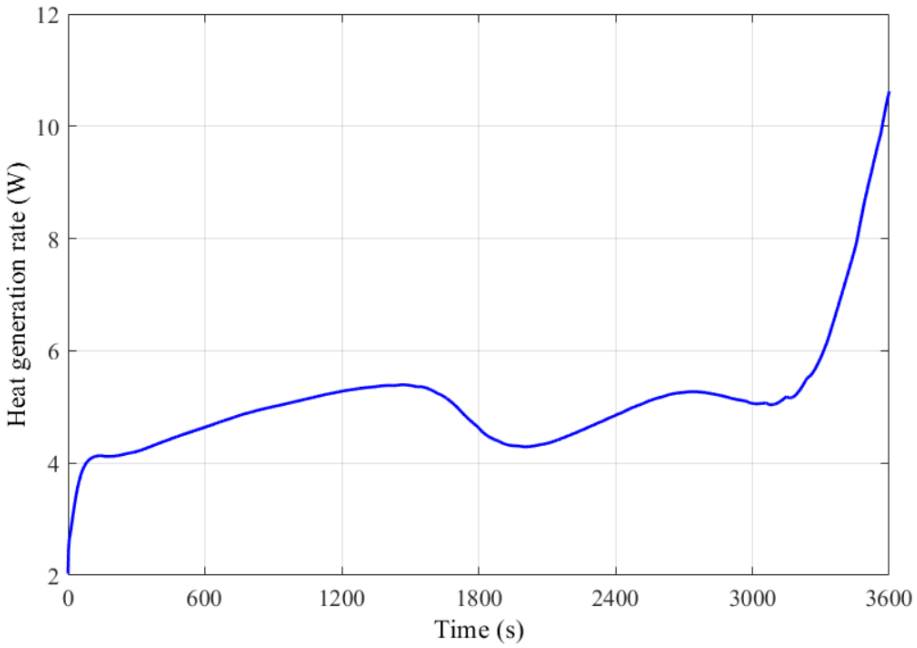

Figure 5.6: Heat generation during 1C discharge

It is assumed that the point in which it is possible to install a sensor to measure the surface temperature is located on the X-Y plane in the middle of the poles, as shown in Figure 5.1. The surface temperature (T_s) that is considered for Kalman filter estimation in 1C charge/discharge is demonstrated in Figure 5.7 and Figure 5.8. It contains zero-mean white Gaussian noise (covariance=0.001).

.

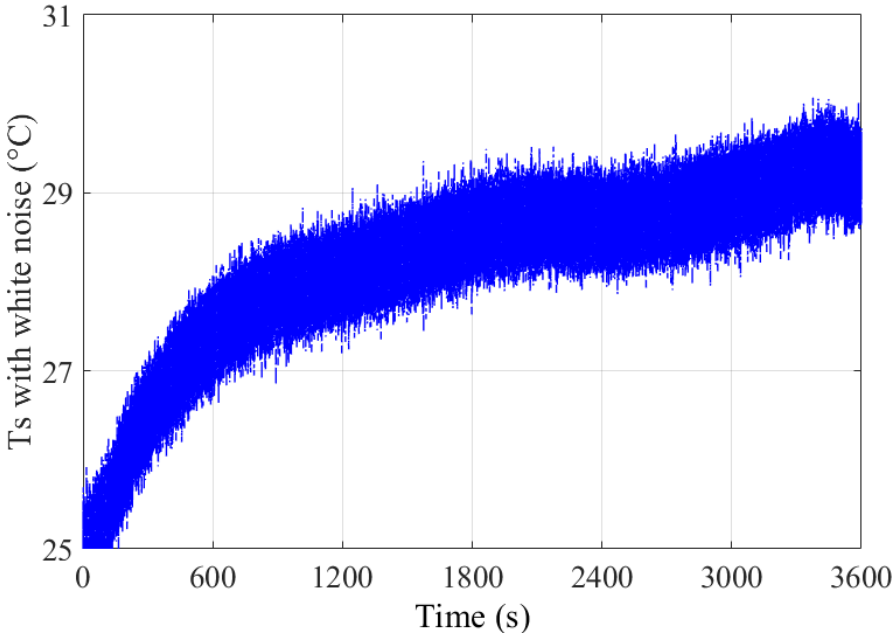

Figure 5.7: The surface temperature during 1C charge

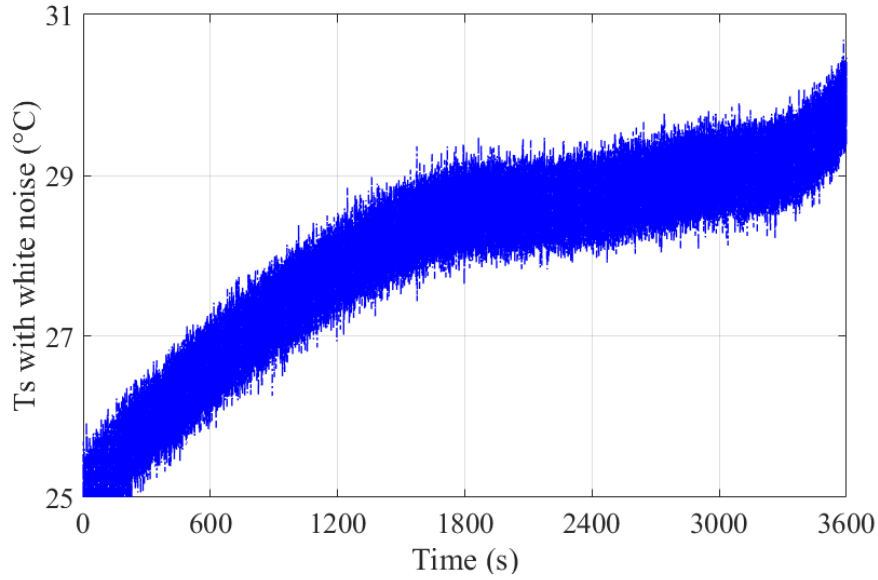

Figure 5.8: The surface temperature during 1C discharge

Having the measurements, state-space inputs (ambient temperature, heat generation rate) and process noise (applied to the system through the Kalman filter block in Simulink with covariance=0.001), the estimation results for 1C charge/discharge rate are given in Figure 5.9 and Figure 5.10. It can be seen that the results of the lumped model for core temperature (T_i) estimation are the same for either Kalman filter or sliding mode observer. Moreover, there is no large difference between surface temperatures obtained by FDM and lumped model. On the other hand, the core temperature estimated by Kalman filter and FDM gives lower values compared to lumped model estimations.

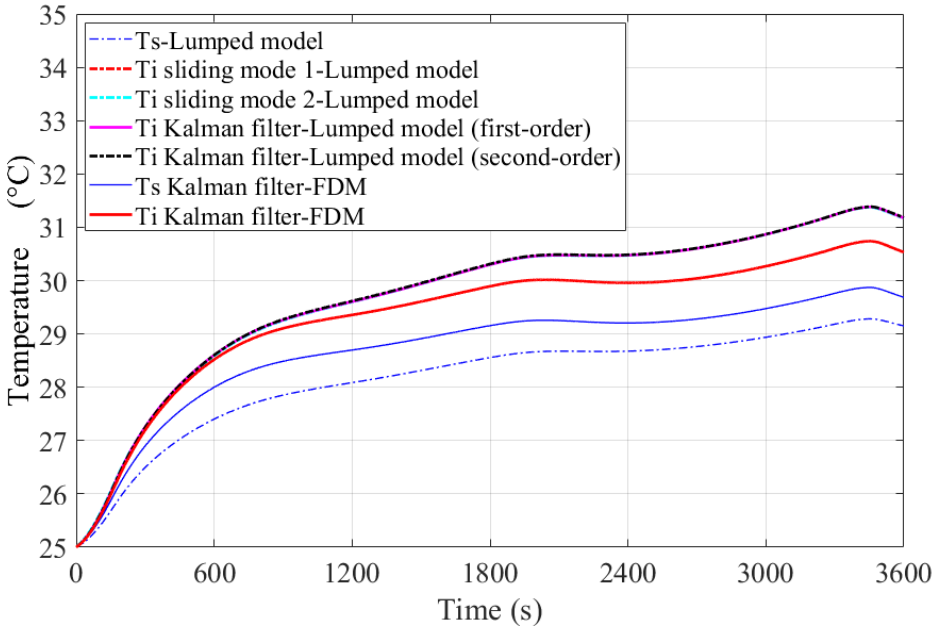

Figure 5.9: The temperature estimation in 1C charge condition

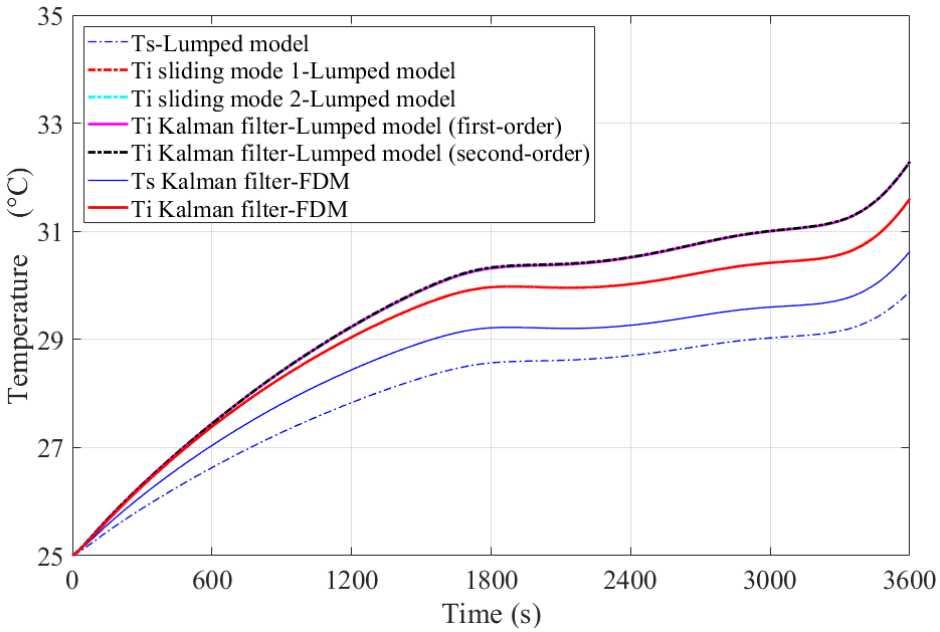

Figure 5.10: The temperature estimation in 1C discharge condition

Since the cell temperature will be different depending on the conditions, the performance was also investigated for 2C charge/discharge rate. In a similar way, the heat generation can be derived as shown in Figure 5.11 and Figure 5.12. It is clear that the heat generation rate is higher than 1C rate. Moreover, with 2C charging the cell will be completely full (SOC=100%) at t=1800 (s) and it will be completely discharged (SOC=0) at t=1800 (s).

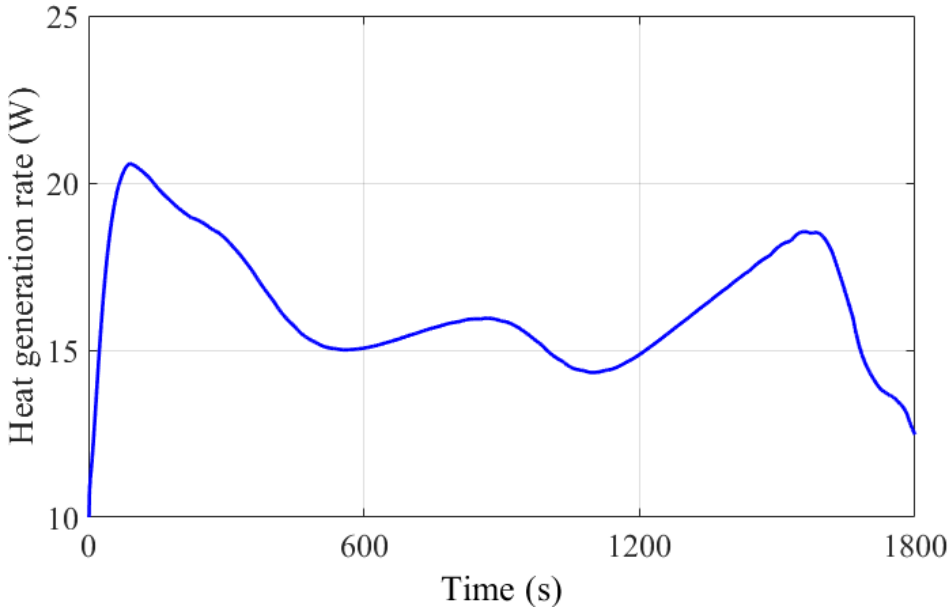

Figure 5.11: Heat generation rate during 2C charge

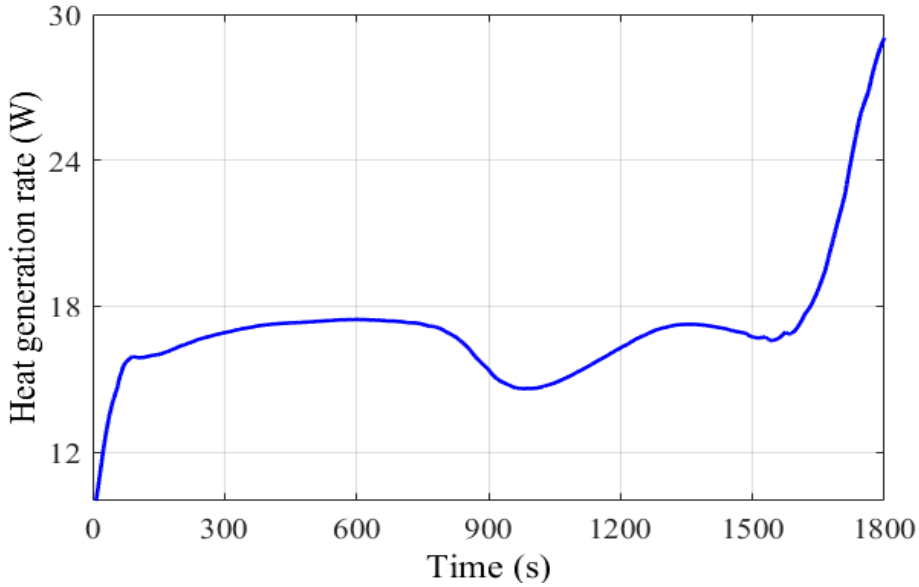

Figure 5.12: Heat generation rate during 2C discharge

In a similar way to before, the surface temperature with white Gaussian measurement noise (covariance=0.001) is given in Figure 5.13 and Figure 5.14.

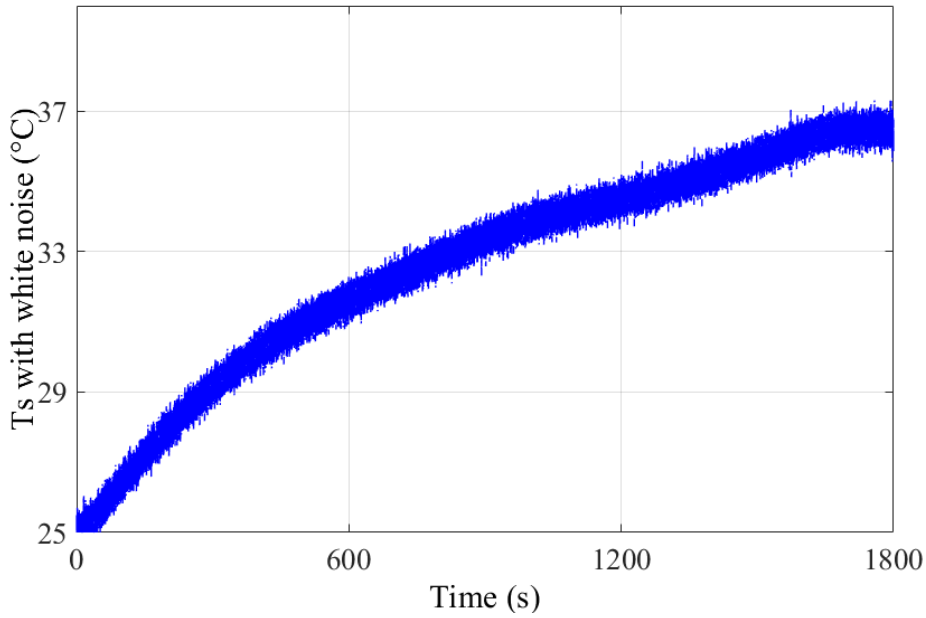

Figure 5.13: The cell surface temperature during 2C charge

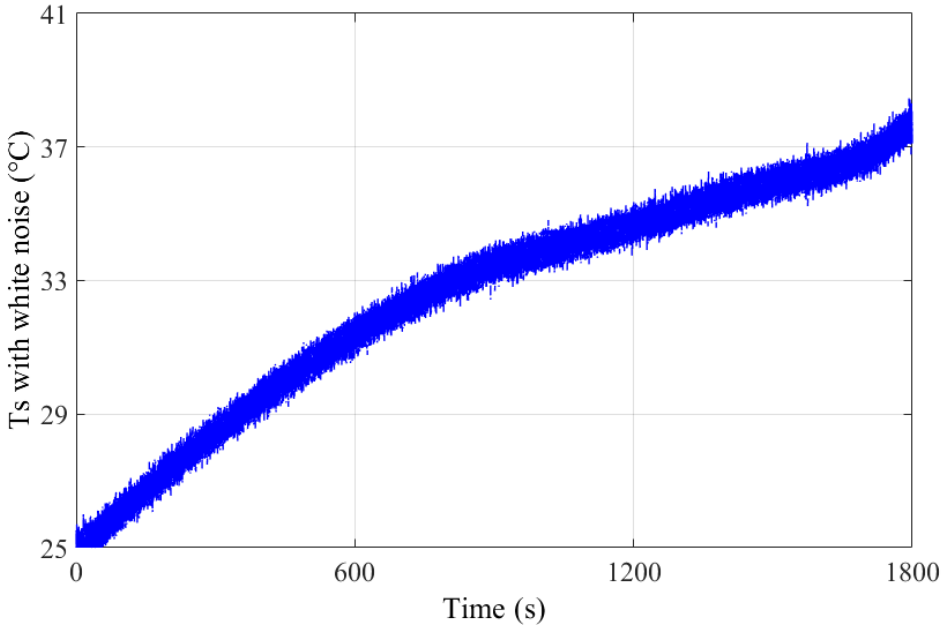

Figure 5.14: The cell surface temperature during 2C discharge

Figure 5.15 and Figure 5.16 illustrate the temperature estimation at 2C charge/discharge. It is notable that likewise 1C rate, the core temperature (T_i) estimation using lumped model are the same for the Kalman filter and the sliding mode observer. Similar to 1C rate, the Kalman filter estimation with FDM thermal model gives T_i values lower than lumped model estimations due to different modeling approach.

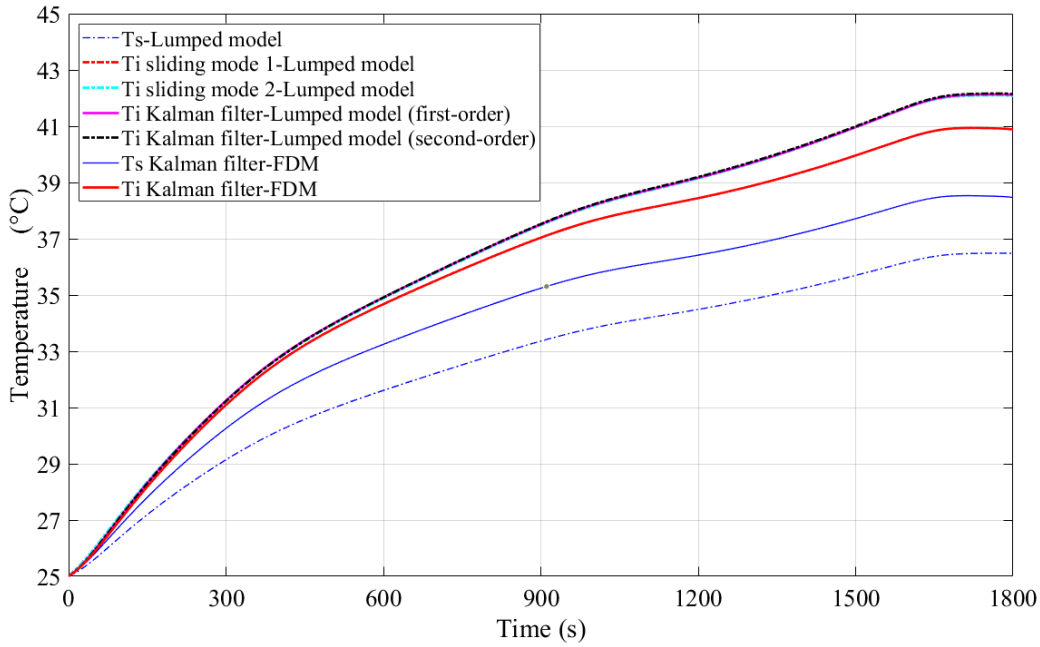

Figure 5.15: The temperature estimation during 2C charge

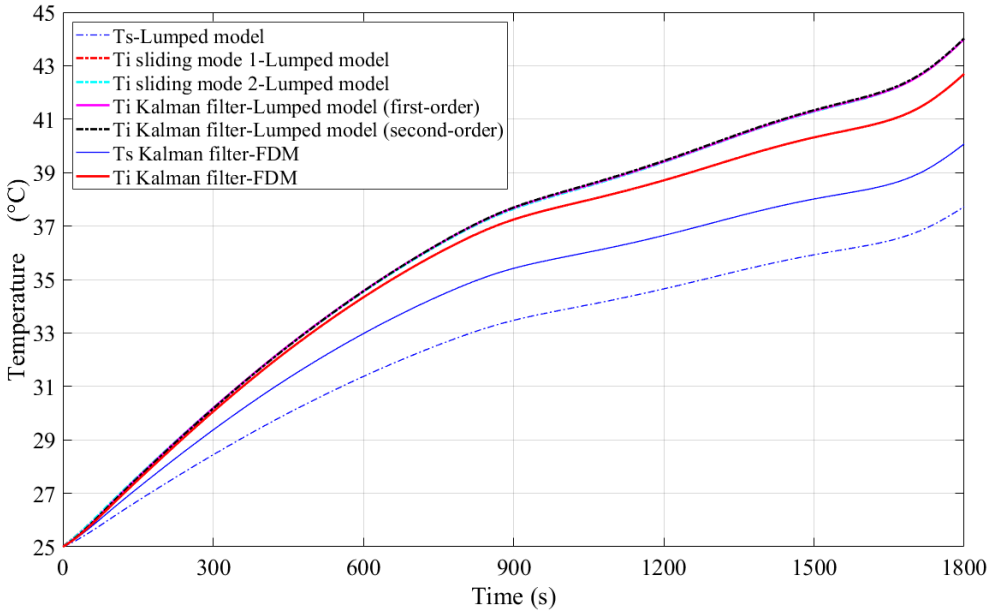

Figure 5.16: The temperature estimation during 2C discharge

The efficiency of thermal models and estimation methods are evaluated by current pulse simulations. Figure 5.17 illustrates the current at 1C rate charge/discharge pulses until t=3600 (s), then the current will be zero until t=5000 (s). The heat generation rate is shown in Figure 5.18.

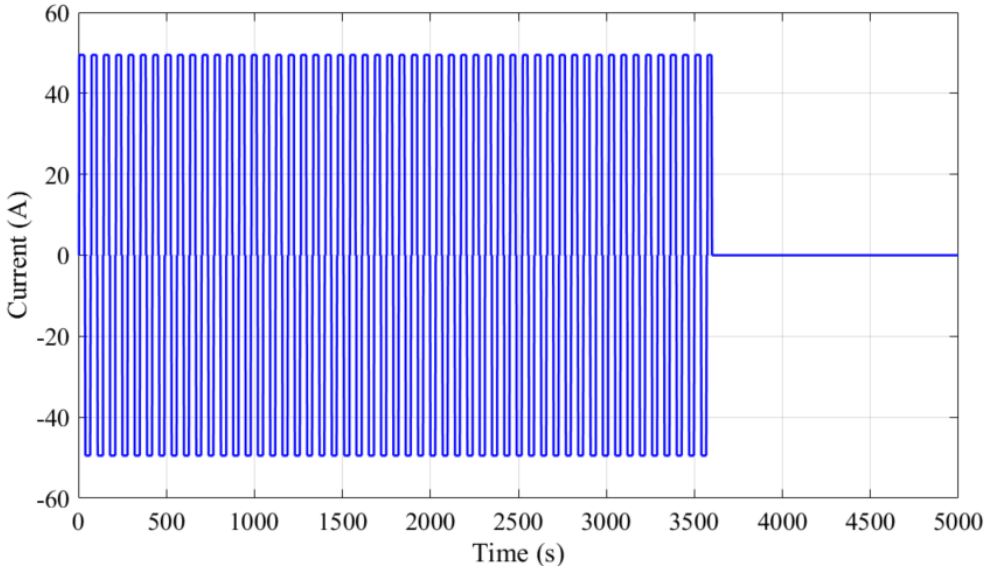

Figure 5.17: Current profile of 1C pulse in charge/discharge

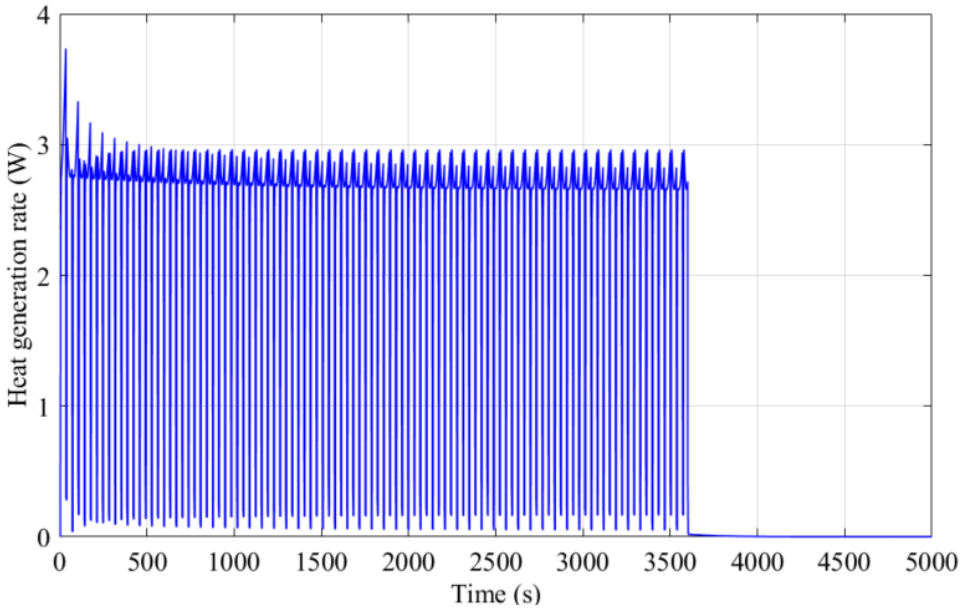

Figure 5.18: Heat generation rate of cell during 1C charge/discharge

The surface temperature that is used as measurement for Kalman filter estimation, contains white Gaussian noise (covariance=0.001), and is shown in Figure 5.19.

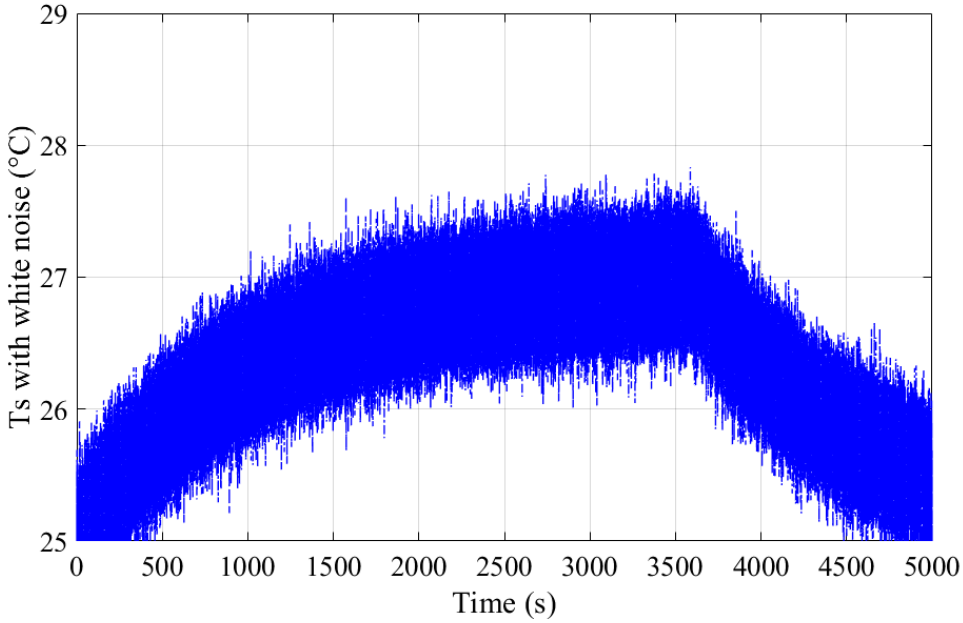

Figure 5.19: The surface temperature with white noise

The estimation results for 1C charge/discharge pulse are shown in Figure 5.20. Similar to the previous case studies, the Kalman filter estimations using FDM thermal model are lower than lumped model estimations. In addition, the core temperature estimation using lumped model are the same for Kalman filter and sliding mode observer as well.

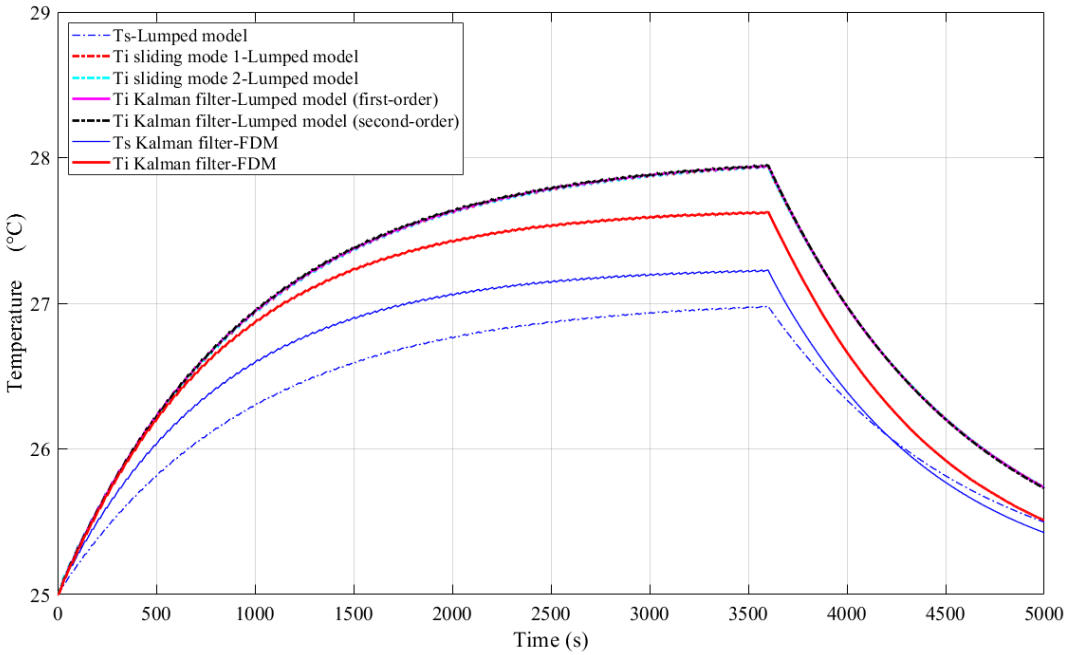

Figure 5.20: The temperature estimation during 1C pulse charge/discharge

5.3 Temperature simulation-FDM results

In addition to estimation, the cell temperature can be derived by solution of heat PDE using finite difference method in a two-dimensional region (X-Y plane of cell) with convection at all boundary conditions. The surface temperature, inside temperature and temperature distribution are as shown in Figure 5.21 to Figure 5.24.

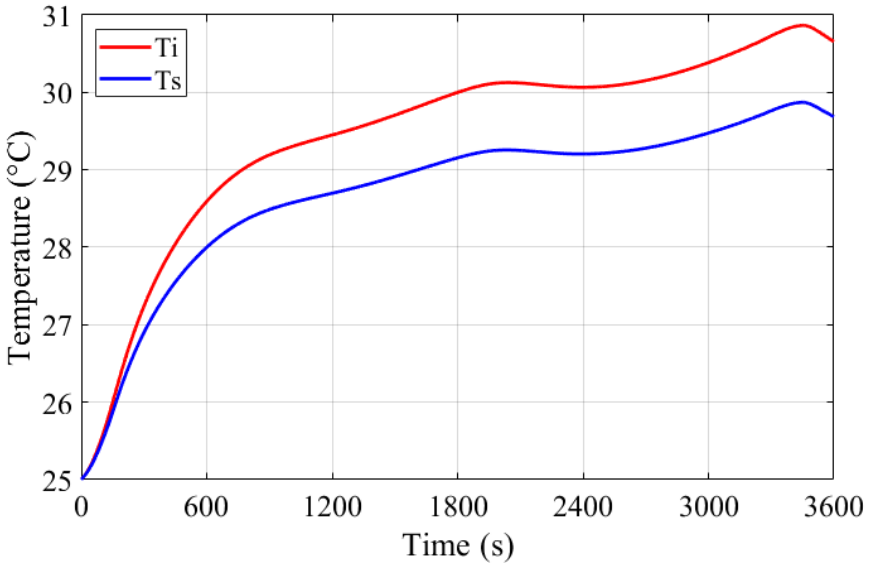

Figure 5.21: The temperature results using FDM during 1C charge

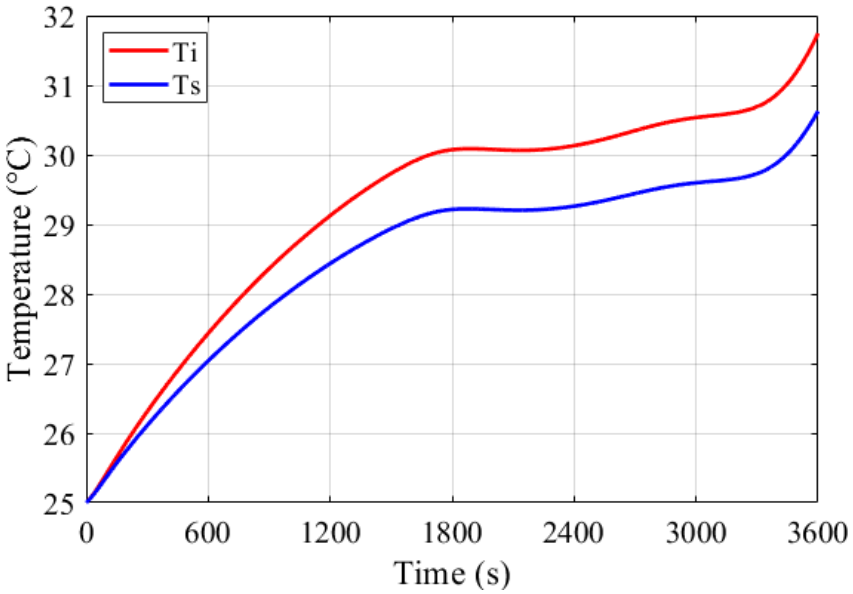

Figure 5.22: The temperature results using FDM during 1C discharge

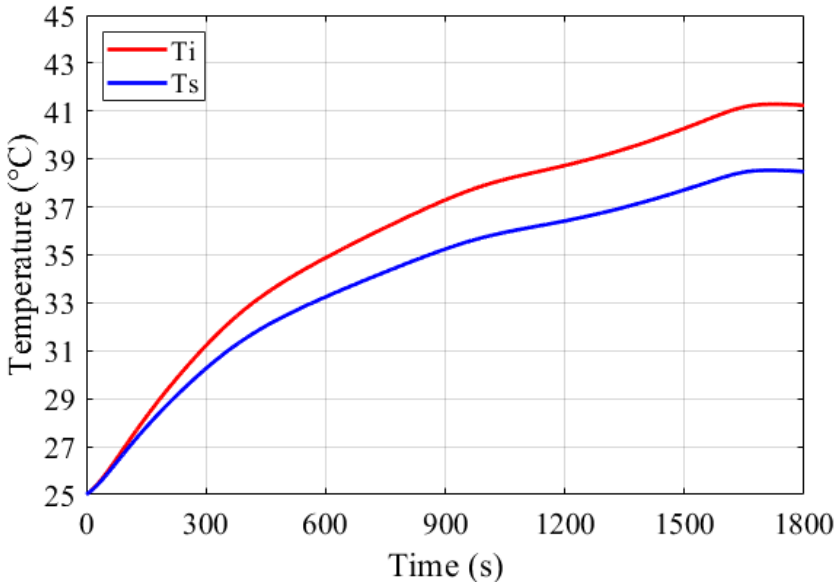

Figure 5.23: The temperature results using FDM during 2C charge

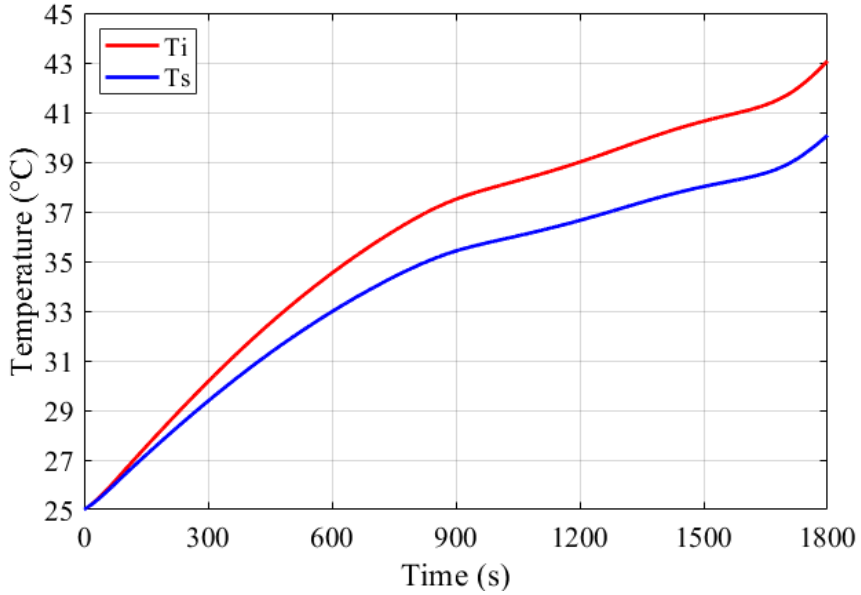

Figure 5.24: The temperature results using FDM during 2C discharge

The temperature distribution obtained by finite difference method are given in Figure 5.25 to Figure 5.28. The comparison of these results and discussions will be done at the end of this chapter.

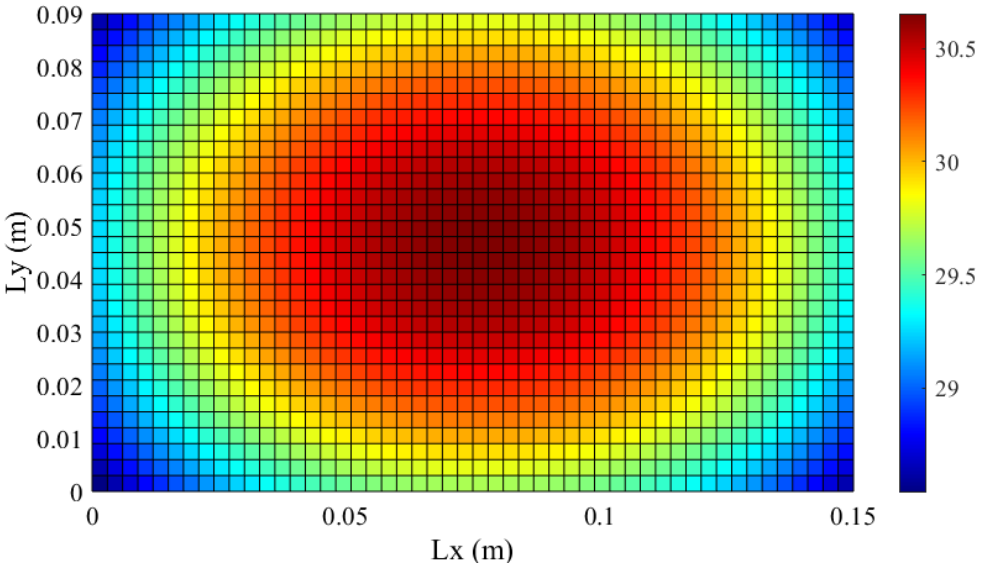

Figure 5.25: The PDE solution using FDM during 1C charge

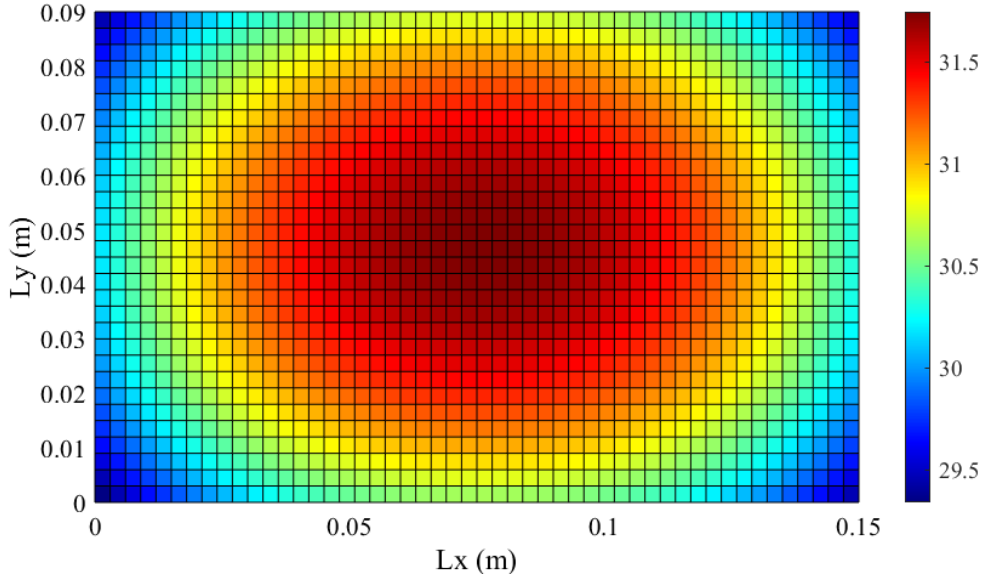

Figure 5.26: The PDE solution using FDM during 1C discharge

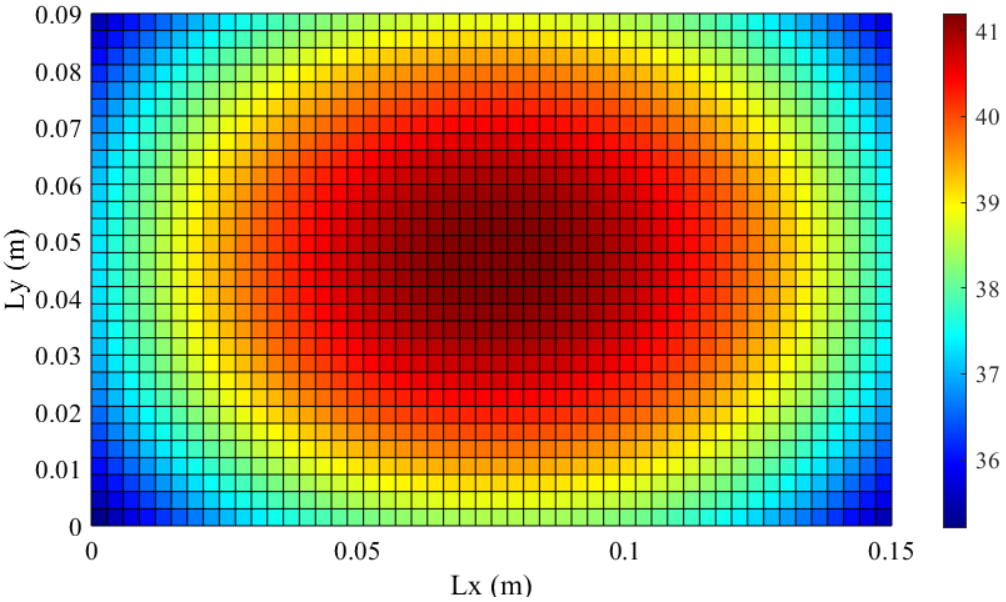

Figure 5.27: The PDE solution using FDM during 2C charge

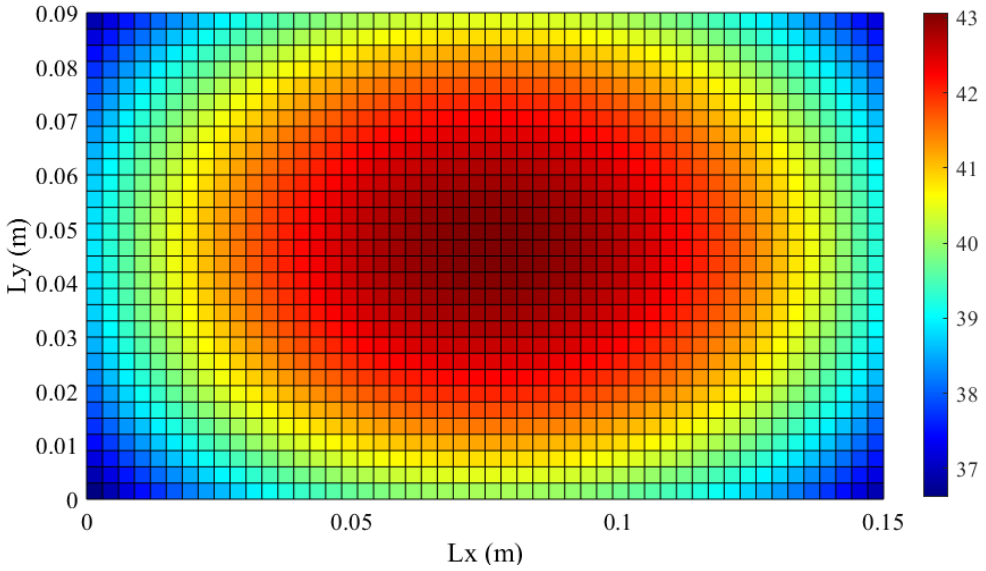

Figure 5.28: The PDE solution using FDM during 2C discharge

5.4 Temperature simulation-FEM

MATLAB PDE toolbox solves the partial differential equations using finite element method. The results of MATLAB PDE toolbox for 1C charge/discharge and 2C charge/ discharge are presented in Figure 5.29 to Figure 5.32. It should be mentioned that due to some limitations in the MATLAB function and time shortage, the heat generation considered is the mean value of the heat generation rate over time. it is thus constant in each case study. Hence, there are no fluctuations in the temperature curves.

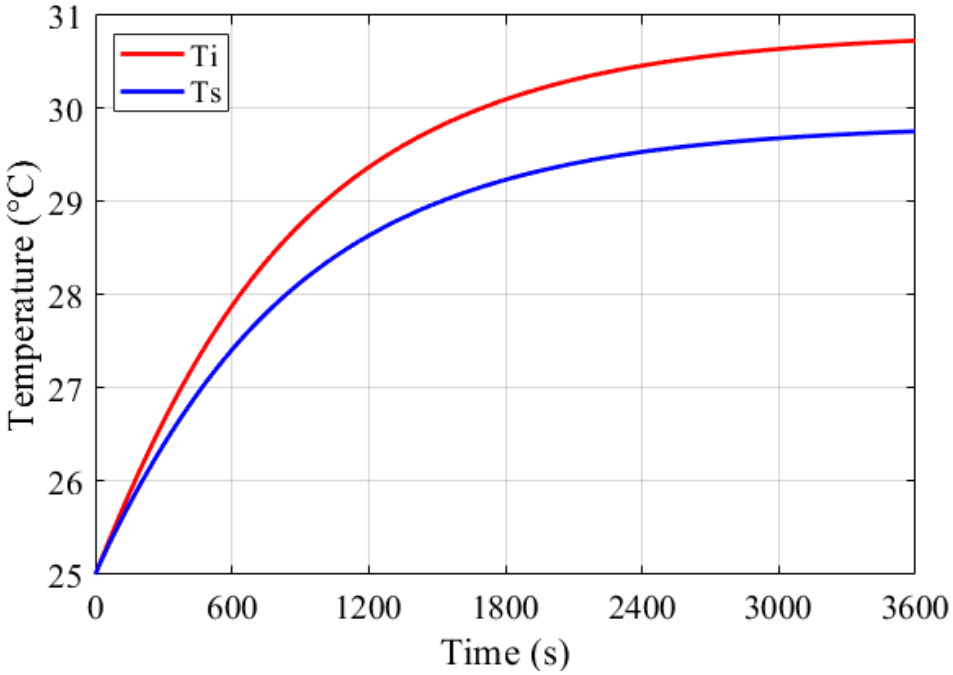

Figure 5.29: The temperature results in 1C charge using FEM

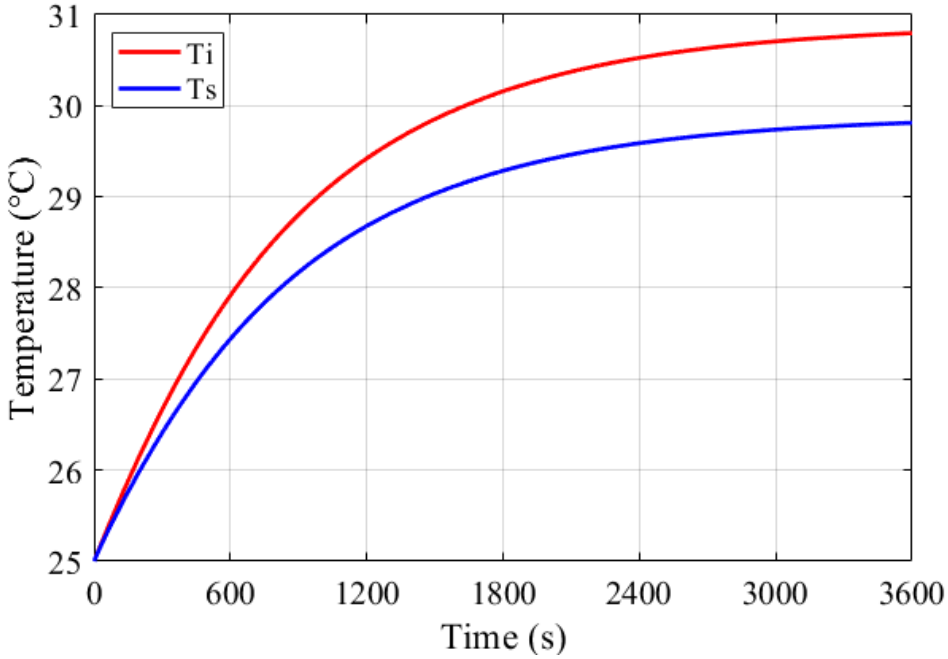

Figure 5.30: The temperature results in 1C discharge using FEM

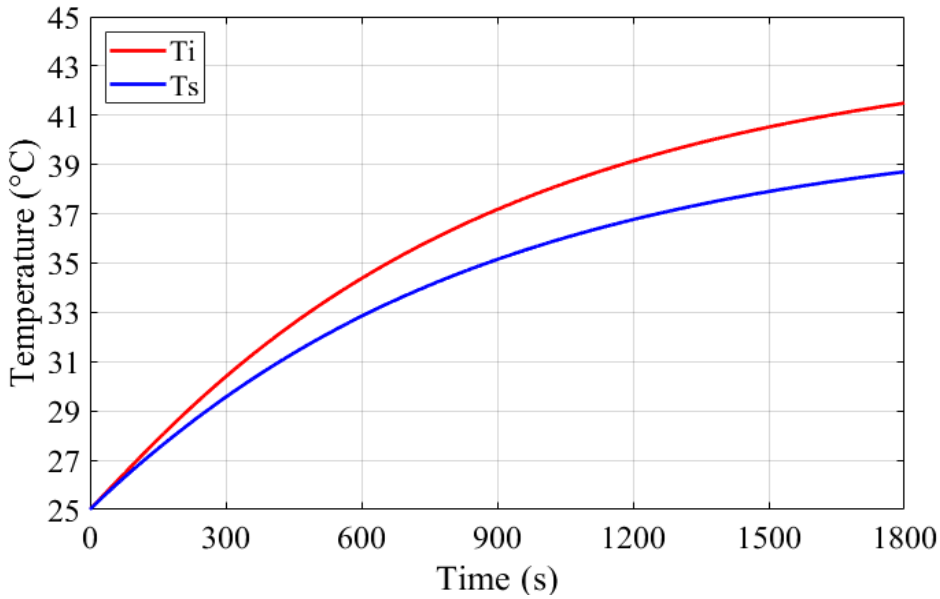

Figure 5.31: The temperature results in 2C charge using FEM

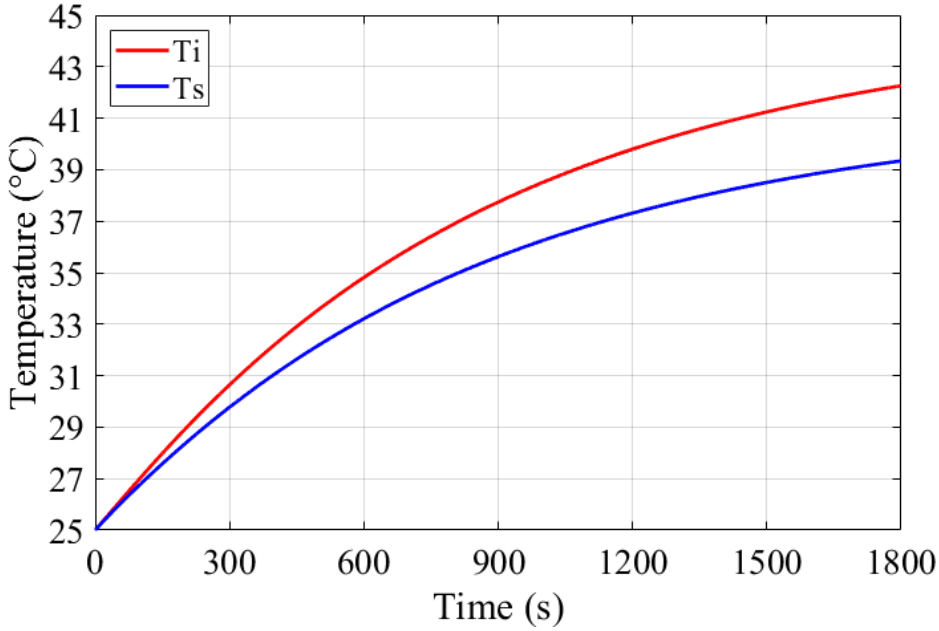

Figure 5.32: The temperature results in 2C discharge using FEM

In adition, the temperature distribution at t=3600 (s) for 1C charge/discharge and t=1800 (s) for 2C charge/discharge illustrated in Figure 5.33 to Figure 5.36.

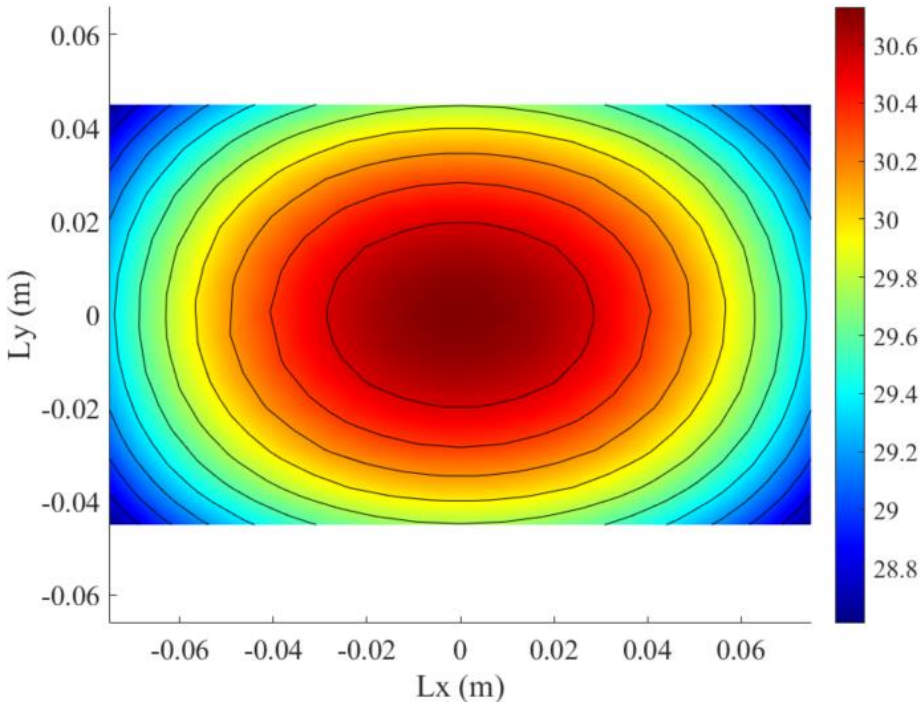

Figure 5.33: The temperature distribution at t=3600 s in 1C charge

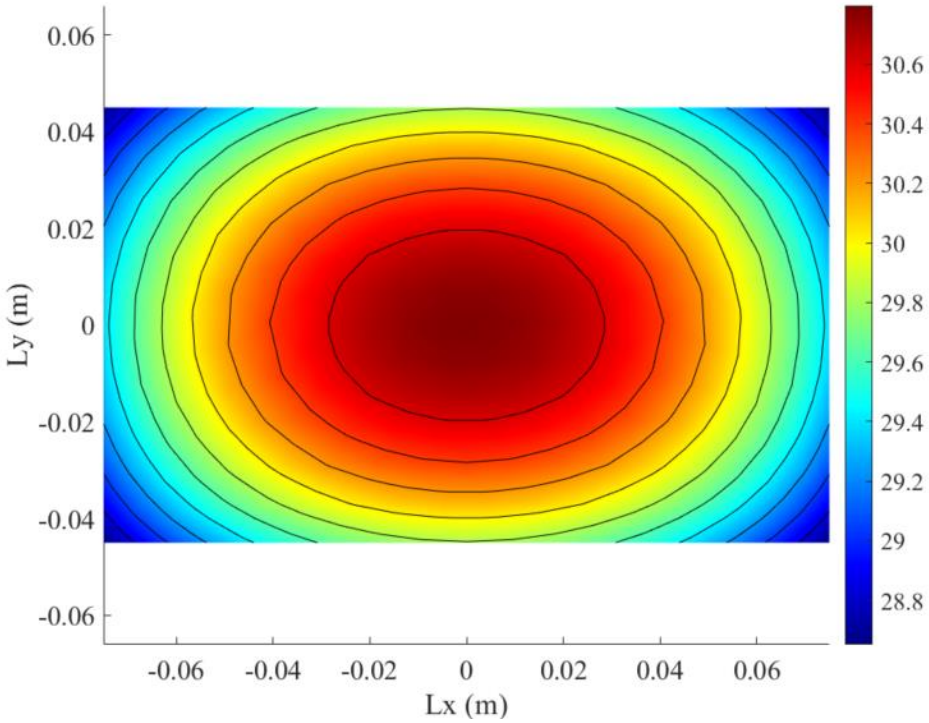

Figure 5.34: The temperature distribution at t=3600 s in 1C discharge

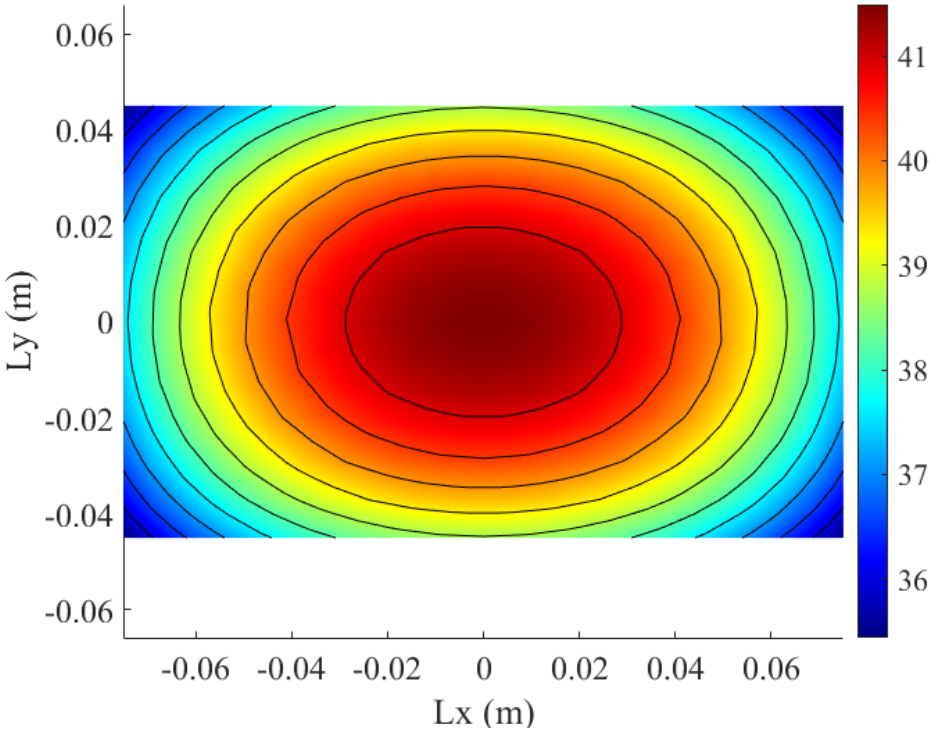

Figure 5.35: The temperature distribution at t=1800 s in 2C charge

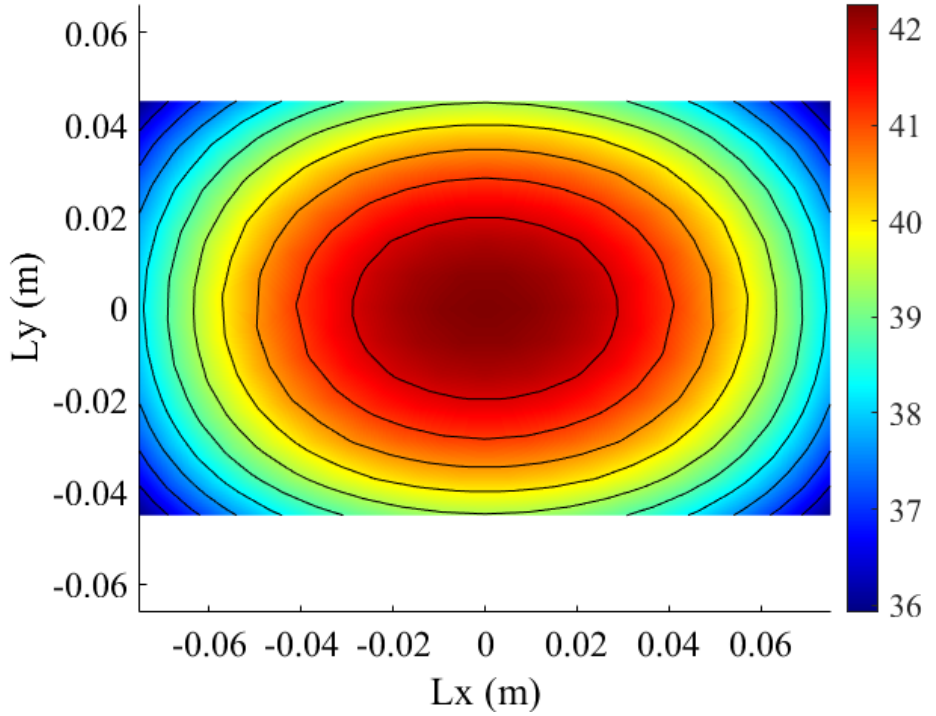

Figure 5.36: The temperature distribution at t=1800 s in 2C discharge

5.5 Discussion about the results

Table. 5.2 compares the estimation results with FDM and FEM solutions for t=3600 s (for 1C charge/discharge) and t=1800 s (for 2C charge/discharge). Regarding Table. 5.2 results for 1C charge/discharge, the surface temperatures are almost the same for 1C charge. This implies that all methods give approximately the same results despite different estimation and modelling approaches. However, for 2C charge/discharge, the surface temperatures of the lumped method are significantly lower than the mesh-based methods' results.
It can be seen that core temperatures (T_i) for 1C charge/discharge using the lumped model are higher than FDM and FEM results. The reason can be the modelling approach of lumped method in which the temperature distribution is approximated with one single resistance in all directions. Therefore, it makes the lumped method to overestimate the core temperature.
Regarding 2C charge/discharge results, the mesh-based methods give approximately the same results for core temperature (T_i). On the other hand, T_i values correspond to lumped method are still higher than mesh-based models, especially for 2C discharge condition. Due to the same reason mentioned for the 1C charge/discharge case, the lumped method in 2C charge/discharge overestimates T_i as well.

Table 5.2: The temperature comparison for all case studies and methods

	Method		T_i	T_s	ΔT
1C charge	Estimation	Lumped	31.4	29.3	2.1
		FDM	30.7	29.8	0.9
	PDE solution	FDM	30.6	29.6	1.0
	PDE toolbox	FEM	30.7	29.7	1.0
1C discharge	Estimation	Lumped	32.2	29.8	2.4
		FDM	31.5	30.6	0.9
	PDE solution	FDM	31.7	30.6	1.1
	PDE toolbox	FEM	30.8	29.8	1.0
2C charge	Estimation	Lumped	42.1	36.5	5.6
		FDM	41.0	38.5	2.5
	PDE solution	FDM	41.3	38.5	2.8
	PDE toolbox	FEM	41.5	38.7	2.8
2C discharge	Estimation	Lumped	43.9	37.7	6.2
		FDM	42.7	40.0	2.7
	PDE solution	FDM	43.1	40.1	3.0
	PDE toolbox	FEM	42.3	39.3	3.0

5.6 Validation

In order to do validation of the results, the CFD results are compared with the estimation and PDE solution results (FDM and FEM method). As mentioned earlier, the CFD model includes the jelly stack, current collectors, cell housing and surrounding environment. All the mentioned components are meshed in a CFD software. In addition, all surfaces on cell housing have convection heat transfer except the top surface which is adiabatic (no convection) so that it is covered by a layer of plastic material. The transient CFD simulation is done in time duration 0-1980 (s) at 1C charge condition. The temperature of points No.1,2,3,4,5 and 6 are plotted versus time. The positions of the mentioned points are shown in Figure 5.37. The temperature of point No. 6, which corresponds to the core temperature, is the reference for validation.

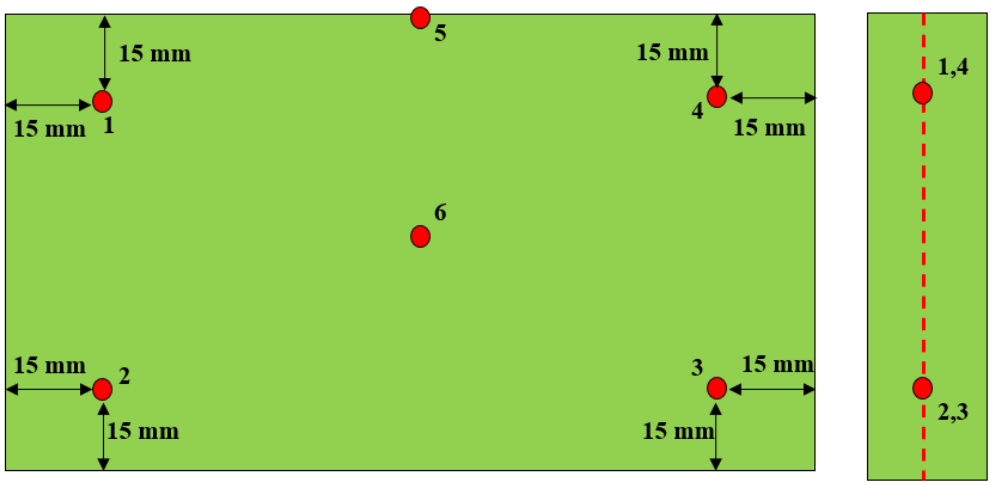

Figure 5.37: The location of points used for validation

The heat generation rate obtained from CFD simulations at 1C charge condition is illustrated in Figure 5.38. Since the C-rate for this cell is higher than the previous cell, the heat generation is higher as well. For validation purpose, this heat generation is applied to the MATALAB/Simulink model that was described in the modelling chapter.

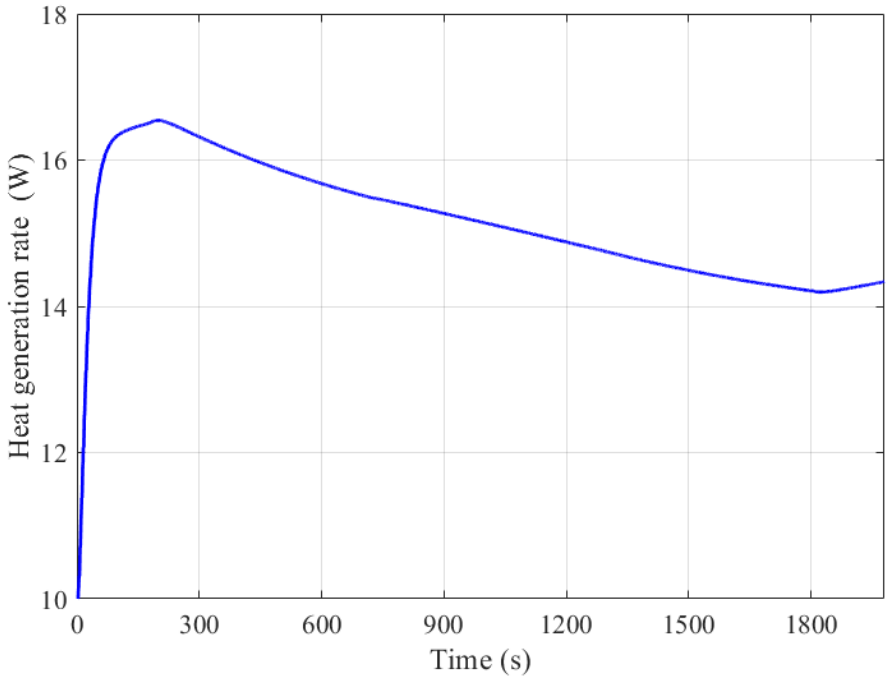

Figure 5.38: Heat generation rate for CFD simulations in 1C charge

The comparison of simulations is depicted in Figure 5.39, where it can be seen that the T_i obtained by Kalman filter estimation using the FDM thermal model can follow the CFD curve with 1.4 ℃ error. This implies that although the FDM model is very simplified (It models only the jelly stack), it can give better results than the lumped model due to mesh generation that leads to modelling the temperature gradient inside the cell from surface to the center point in X- and Y-directions.
The estimation using the lumped-based model with either the Kalman filter or the sliding mode observer is almost 3.5 ℃, which is relatively large. This reveals that the lumped model is not able to model the cell temperature well because it simulates the whole cell as a single point without considering temperature distributions in the X- and Y-directions.

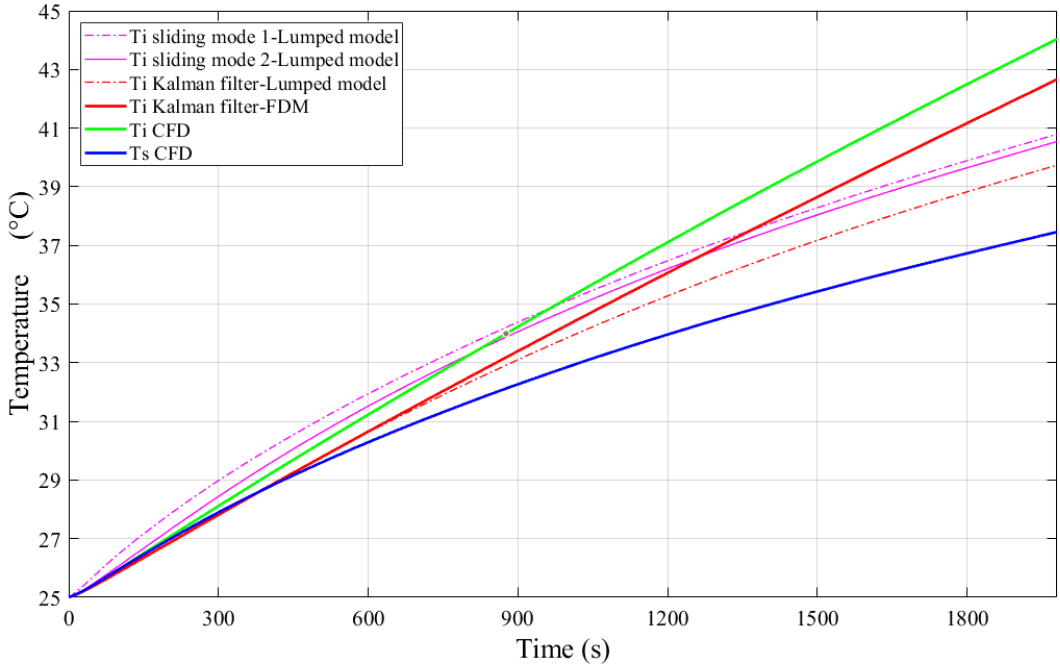

Figure 5.39: The comparison of temperature estimation with CFD simulations in 1C charge

By applying the heat generation from the CFD simulation (shown in Figure 5.38) to the FD and FE model, the temperature distribution can be obtained, as illustrated in Figure 5.40 and Figure 5.41, respectively. It can be seen that both methods give the same values despite of using different methods. The maximum temperature in both contour plots is 42.5 ℃ , which is quite closed to the estimated temperature using Kalman filter combined with FDM.

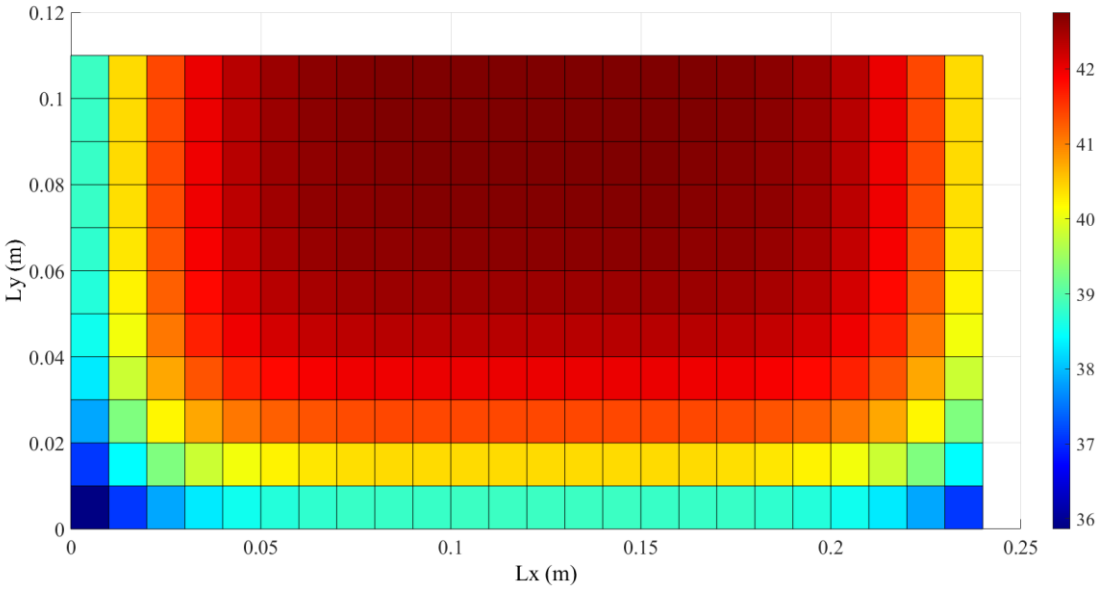

Figure 5.40: Temperature distribution using FDM at t=1980 (s)

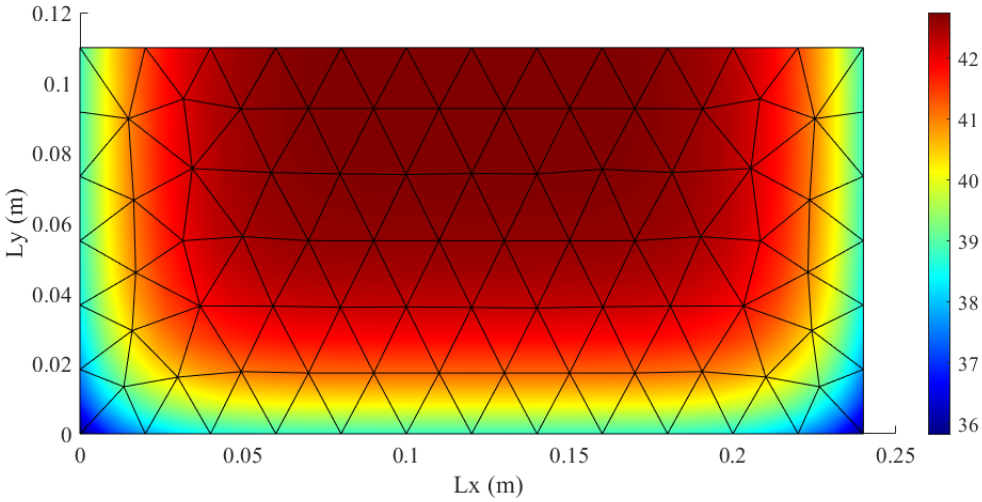

Figure 5.41: The temperature distribution using FEM at t=1980 (s)

The temperature results of T_i and T_s for the Kalman filter estimation are compared with FDM and FEM results in Figure 5.42. It can be seen that T_s obtained by CFD, FDM and FEM are relatively close despite different modeling approaches. In addition, T_i estimation obtanied by the Kalman filter using FDM thermal modelling, FDM and FEM solutions are able to give core temperautre close to CFD curve.

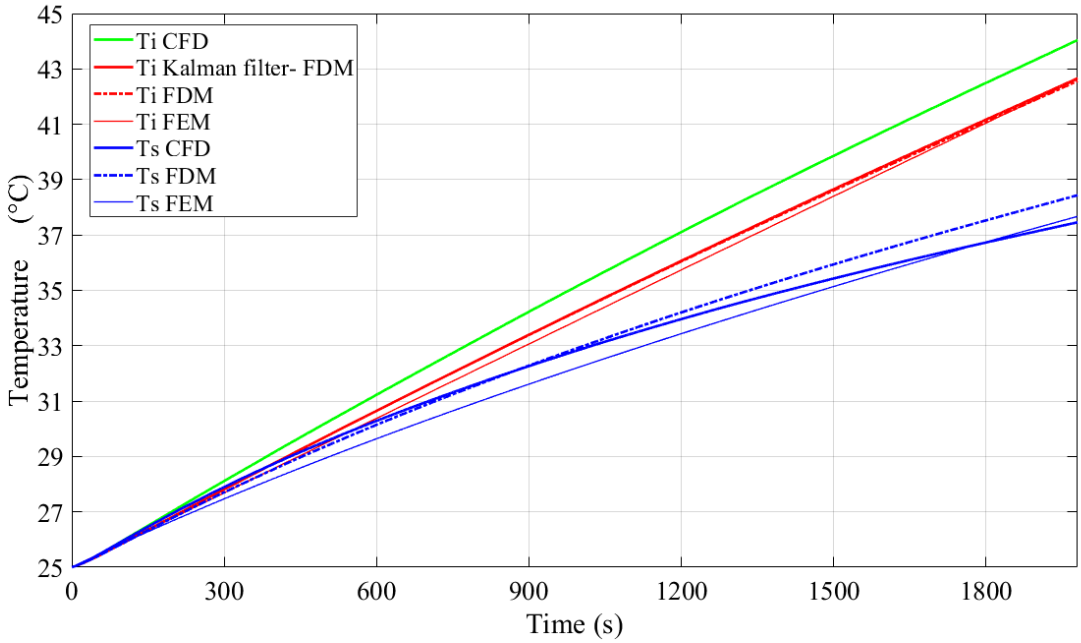

Figure 5.42: The comparison of FDM and FEM solutions with CFD results in 1C charge

The validation results can be summarized in Table.5.3. It can be seen that the mesh-based models such as Kalman filter estimation using FDM, FDM and FEM solution are able to give the temperature with 1.4 ℃ difference. On the other hand, the lumped models that use sliding mode observer and Kalman filter give values with approximately 4.3 ℃ difference. Hence, it can be concluded that the lumped method that simplifies whole cell as one point, without considering the temperature distribution in X and Y direction, is not able to follow the CFD

result compared to mesh-based methods. In addition, the methods that works based on meshing and considering the temperature variation inside the cell have better correlation with CFD results.

Table 5.3: The validation results based on estimation, FDM and FEM solutions at t=1980 (s)

Method		T_i	error
Estimation	Sliding mode 1-Lumped model	40.8	3.2
	Sliding mode 2-Lumped model	40.5	3.5
	Kalman filter-Lumped model	39.7	4.3
	Kalman filter-FDM	42.6	1.4
simulation	**CFD**	**44**	**---**
	FDM	42.6	1.4
	FEM	42.6	1.4

Chapter 6: Conclusions

6.1 Conclusion

Several methods to estimate the core and surface temperature of prismatic lithium-ion cell are derived and analyzed in this thesis. More specially, the temperature estimation carried out using Kalman filter for lumped model and FDM as well as sliding mode observer for only lumped model in this thesis. Although, the lumped model is easy to use and suitable for real-time applications, this method simulates the cell as an equivalent circuit, so its accuracy and performance depends on its parameters, i.e., R_i, R_o, C_c and C_s. Hence, these parameters must be identified correctly using identification and experiment data. It can be seen from the results that the lumped model performance is different as compared to FDM and CFD. One of the reasons can be the values of the RC parameters which were obtained from a similar cell in a research article. Another reason can be the lumped method modelling in which the whole cell is simulated as a zero-dimensional material without considering the temperature distribution. In addition, the internal structure of a cell is fairly complex since it consists of several materials with different heat transfer specifications in X, Y and Z-directions. This implies that the temperature distribution inside the cell cannot be identical. Thus the assumptions behind lumped model can generate some discrepancy compared to FDM and CFD that are based on meshing and describe spatial temperature variation inside the cell.

The FDM thermal model simulates the whole cell through meshing of a two-dimensional plate with equivalent thermal conductivity and convection coefficients in which each node temperature represents one state variable. Therefore, a large number of state variables result from the meshing. For example, by having 10 nodes each in X and in Y- direction, the dimensions of state space will be 100 which makes the problem troublesome in terms of simulation time. However, the advantage of this method is that it considers the temperature variation inside the cell, and it gives reliable results that have better correlation with CFD results. Regarding the complicated internal structure of a cell, a drawback of the FDM used in this thesis is that it considers the whole cell as one single material (without cell housing) with uniform equivalent thermal properties in all directions.

The estimations were done by Kalman filters and sliding mode observers for the lumped model. Two different sliding mode observers (original and modified sliding mode observer) were designed for the lumped model. Both methods give the same results, and consequently the same performance. In comparison with the sliding mode observers, the Kalman filter is more practical because it also considers the noise in the measurements and the process.

The temperature contour inside the cell obtained by solving the heat equation in two dimensions with conduction boundary condition using FDM and FEM (MATALB PDE toolbox) shows that these methods can be useful to verify the estimation results despite the fact that it is not possible to use them in real-time application today.

6.2 Future work

As mentioned earlier, the internal structure of the cell is complicated, including air gap, jelly stack, current collectors and so on. Hence, having accurate values for thermal conductivity, convection coefficient, thermal resistances and other parameters is challenging. Thus, it is recommended to identify the mentioned parameters through identification algorithms using experimental lab tests on the specific cell.

The Kalman filter estimates surface temperature that is described by white Gaussian noise. It is suggested to measure the cell surface temperature in lab to evaluate the performance of the Kalman filter. It is recommended to validate the estimation results with more complex experimental conditions. Moreover, the thermal modelling approaches and estimation methods can be implemented to multi-cell systems together with a cooling system that makes the modelling process more complicated. Therefore, the model of multi-cell system should be compromised in terms of computational time, feasibility for real-time applications and so on. In addition, it can be proposed to apply all the modelling and simulations of this thesis that is done on a prismatic cell, to a cylindrical cell as well.

Reference

[1] H. S. Hamut, N. Javani, and I. Dinçer, *Thermal Management of Electric Vehicle Battery Systems*, ISBN 9781118900246, 2017.

[2] European Commission. "Stepping up Europe's 2030 climate ambition Investing in a climate-neutral future for the benefit of our people". https://eur-lex.europa.eu/legal-content/EN/TXT/?uri=CELEX%3A52020DC0562, 2020

[3] C. Julien, A. Mauger, A. Vijh and K. Zaghib, "*Lithium Batteries Science and Technology"*, ISBN 978-3-319-19107-2, ISBN 978-3-319-19108-9 (eBook), doi 10.1007/978-3-319-19108-9.

[4] European Environment Agency. (2022). New registrations of electric cars, EU-27. [Online]. Available from: https://www.eea.europa.eu/data-and-maps/daviz/new-electric-vehicles-in-eu-2/#tab-chart_2

[5] J. Jiang and C. Zhang, *Fundamentals and Applications of Lithium-Ion Batteries in Electric Drive Vehicles*, ISBN 978-1-118-41478-1, 2015.

[6] Ralph J. Brodd, *Batteries for Sustainability*, ISBN 978-1-4614-5791-6, https://doi.org/10.1007/978-1-4614-5791-6, 2013.

[7] Y. Ma, Y. Cui, H. Mou, J. Gao, H. Chen, "Core temperature estimation of lithium-ion battery for EVs using Kalman*"*, *Applied Thermal Engineering* 168114816, 2020.

[8] R. R. Richardson, P. T. Ireland., D. A. Howey, "Battery internal temperature estimation by combined impedance and surface temperature measurement", *J. Power Sources* 265 254–261, https://doi.org/10.1016/j.jpowsour.2014.04.129, 2014.

[9] M. O'Leary, Battery packs for heavy-duty electric vehicles, Available from: https://www.volvogroup.com/en/news-and-media/news/2022/may/battery-packs-for-electric-vehicles.html, 2020.

[10] D. Worford, DFDS Makes Volvo's Largest Electric Truck Order, Available from: https://www.environmentalleader.com/2021/10/dfds-makes-volvos-largest-electric-truck-order/ ,2021.

[11] G. Pistoia, *Lithium-Ion Batteries : Advances and Applications*, ISBN 9780444595164, Oxford , Elsevier, 2014.

[12] C. Zhang, K. Li, J. Deng, "real time estimation of battery internal temperature based on a simplified thermoelectric model", *Journal of Power Sources* 302 146-154, 2016.

[13] D. Andrea, *Lithium-Ion Batteries and Applications: A Practical and Comprehensive Guide to Lithium-Ion Batteries*, Volume 1, Batteries. Norwood: Artech House, ISBN 9781630817688, 2020.

[14] X. Lin, H. E. Perez, S. Mohan, J. B. Siegel, A. G. Stefanopoulou, Y. Ding, M. P. Castanier, "A lumped-parameter electro-thermal model for cylindrical batteries", *Journal of Power Sources*, 257 1-11, 2014.

[15] J. Sun, G. Wei, L. Pei, R. Lu, K. Song, C. Wu and C. Zhu, "Online Internal Temperature Estimation for Lithium-Ion Batteries Based on Kalman Filter", *Energies,* 8 4400-4415, 2015.

[16] H. Dai, L. Zhu, J. Zhu, X. Wei and Z. Sun, "Adaptive Kalman filtering based internal temperature estimation with an equivalent electrical network thermal model for hard-cased batteries", *Journal of Power Sources*, 293 351-365, 2015.

[17] L Chen, M. Hu, K. Cao, S. Li, Z. Su, G. Jin and C. Fu, "Core temperature estimation based on electro-thermal model of lithium-ion batteries", *Int J Energy Res.*, 445320–5333, 2020.

[18] C. Zhang, K. Li, J. Deng, "Real-time estimation of battery internal temperature based on a simplified thermoelectric model", *Journal of Power Sources* 302 146-154, 2016.

[19] H. Pang, L. Guo, L. Wu , J. Jin , F. Zhang , K. Liu, "A novel extended Kalman filter-based battery internal and surface temperature estimation based on an improved electro-thermal model", *Journal of Energy Storage*, 41 102854, 2021.

[20] S. Sattarzadeh, T. Roy, S. Dey, "Real-Time Estimation of 2-D Temperature Distribution in Lithium-Ion Pouch Cells", *IEEE transactions on transportation electrification*, vol. 7, no. 4, 2021.

[21] W. Zhou, Y. Zheng, Z. Pan and Q. Lu, "Review on the Battery Model and SOC Estimation Method", 9, 1685, 2021, https://doi.org/10.3390/pr9091685.

[22] Y. Wang, Y. Tian, J. Sun, Z. Wang, L. Xu, R. Li, M. Chen, Z. "A comprehensive review of battery modeling and state estimation approaches for advanced battery management systems". *Renewable and Sustainable Energy Reviews*., 131, 110015, https://doi.org/10.1016/j.rser.2020.110015, 2020.

[23] B. Xia, Z. Sun, R. Zhang, R. Zhang, and Z. Lao, "A cubature particle filter algorithm to estimate the state of the charge of lithium-ion batteries based on a second-order equivalent circuit model", *Energies* 10(4)-457, 2017.

[24] M. Soltani, S. H. Beheshti, "A comprehensive review of lithium-ion capacitor: development, modelling, thermal management and applications", *Journal of Energy Storage* 34 102019, 2021.

[25] S. Nejad, D.T. Gladwin, D.A. Stone, "A systematic review of lumped-parameter equivalent circuit models for real-time estimation of lithium-ion battery states", *Journal of Power Sources* 316 183-196, 2016.

[26] F. P. Incropera, D. P. DEWITT, T. L. Bergman, A. S. Lavine, "*Fundamentals of Heat and Mass Transfer*", ISBN-13: 978-0-471-45728-2, 2007.

[27] Anon. 2015. What's the Difference Between Conduction, Convection, and Radiation? [Online]. Available from: https://www.machinedesign.com/learning-resources/whats-the-difference-between/document/21834474/whats-the-difference-between-conduction-convection-and-radiation, 2023.

[28] J. P. Holman, *Heat Transfer*, Tenth Edition, McGraw-Hill, ISBN 978–0–07–352936–3, 2010.

[29] D. Bernardi, E. Pawlikowski and J. Newman, "A General Balance for Battery Systems, Journal of Electrochemical Science and Technology", *J. Electrochem. Soc.* 132 5, 1985.

[30] L. Zhang, H. Peng, Z. Ning, Z. Mu and C. Sun, "Comparative Research on RC Equivalent Circuit Models for Lithium-Ion Batteries of Electric Vehicles", *Applied. Science*, 7, 1002; https://doi.org/10.3390/app7101002., 2017.

[31] B. Alsadik, Adjustment Models in 3D Geomatics and Computational Geophysics, eBook ISBN: 9780128175897, Paperback ISBN: 9780128175880.

[32] T. Glad, L. Ljung, *Control Theory- Mulitvariable and Nonlinear Methods*, 2010.

[33] K. J. Åsröm, R. M. Murray, *Feedback Syetm- An Introduction for Scientists and Engineers*, Version v2.10b, 2008.

[34] S. Särkkä, Bayesian Filtering and Smoothing, Cambridge University Press, IBSN 9781139344203,2014 https://doi-org.proxy.lib.chalmers.se/10.1017/CBO9781139344203

[35] G. R. Liu, S. S. Quek, *The finite element method: a practical course*,2nd edition. Butterworth-Heinemann, ISBN 0080983561, 2014.

[36] N. S. Ottosen, H. Pettersson, *Introduction to the finite element method*, ISBN 0134738772, 1992.

[37] Partial Differential Equation Toolbox, User's Guide, 1995–2023.

[38] M. Steinhardt, J. V. Barreras, H. Ruan, B. Wu, G. J. Offer, A. Jossen, "Meta-analysis of experimental results for heat capacity and thermal conductivity in lithium-ion batteries: A critical review", *Journal of Power Sources* 522 230829,2022.

[39] T. S. Bryden, B. Dimitrov, G. Hilton, C. P. D. León, P. Bugryniec, S. Brown, D. Cumming, A. Cruden, "Methodology to determine the heat capacity of lithium-ion cells", *Journal of Power Sources* 395 369–378, 2018.

[40] J. He, R. Youssef, Md S. Hosen, M. Akbarzadeh, J. V. Mierlo, M. Berecibar, "A novel methodology to determine the specific heat capacity of lithium-ion batteries", *Journal of Power Sources* 520 230869, 2022.

[41] D. Werner, A. Loges, D. J. Becker, T. Wetzel, "Thermal conductivity of Li-ion batteries and their electrode configurations A novel combination of modelling and experimental approach", *Journal of Power Sources* 364, 2017.